GROUND MOTIONS AND TSUNAMIS FROM Mw 9.0 CASCADIA SUBDUCTION EARTHQUAKES BASED ON VALIDATIONS USING THE Mw 8.8 MAULE, CHILE EARTHQUAKE OF 2010

FINAL REPORT

March 29, 2013

Paul Somerville, Andreas Skarlatoudis and Wenwen Li*

URS Group, Inc.

915 Wilshire Boulevard
Los Angeles, CA 90017

Tel: (213) 996-2200
Fax: (213) 996-2290

*Email: paul.somerville@urs.com

Contents

GROUND MOTIONS AND TSUNAMIS FROM Mw 9.0 CASCADIA SUBDUCTION EARTHQUAKES BASED ON VALIDATIONS USING THE Mw 8.8 MAULE, CHILE EARTHQUAKE OF 2010

SUMMARY

In the USGS Hazard and NEHRP Design Ground Motion Maps, the subduction source is modeled by earthquakes having magnitudes as large as **M** 9.2. Since these magnitudes are larger than any of the earthquakes on which current empirical ground motion models (Atkinson and Boore, 2003; Zhao et al., 2006; Abrahamson et al., 2012) are based, it is important to use ground motion and tsunami data from the recent **M** 8.8 subduction earthquake in Maule, Chile on February 27, 2010 to provide insight into the nature of ground motions and tsunamis from such large events. The strong motion recordings and tsunami data of this earthquake provide valuable information on what the ground motions and tsunamis from such large earthquakes may be like. With this project we specifically address the task of improving the models of strong ground motions in western Oregon and Washington, particularly including the effects of long duration codas and long periods expected from plate-boundary earthquakes in Cascadia.

Broadband ground motion simulations enhance the usefulness of the recordings of such earthquakes by providing a means of interpolating and extrapolating the recorded data. In this report, we first test our capability to simulate the 21 broadband strong motion recordings of the **M** 8.8 Maule earthquake by demonstrating that our simulations reproduce the amplitudes of the recorded ground motions without systematic bias. We use simulations to study the distribution of the ground motion amplitudes caused by the Maule earthquake, and validate our ground motion simulation method by comparing the simulated and recorded ground motions. We also test our ability to simulate the recorded tsunami wave heights of the Maule earthquake.

Based on this test using the **M** 8.8 Maule earthquake, we then applied our ground motion and tsunami simulation procedures to estimate the ground motion and tsunami characteristics of earthquakes that rupture the entire Cascadia subduction zone. We use four different slip models in order to study the variability and the sensitivity of the simulated ground motions and tsunami inundation to the individual characteristics of each slip model used. We compare the simulated ground motions with those predicted by other models, and make maps of the simulated ground motions for two site conditions, soft rock and deep soil. We provide equations for predicting the response spectra of the ground motions for these two site conditions.

PREVIOUS WORK

This report builds on previous work (Somerville et al., 2008), which used the source characteristics and recorded ground motions of the Mw 8.4 Arequipa, Peru earthquake of 2001 to guide the simulation of ground motions for Cascadia subduction earthquakes in the magnitude range of Mw 8.4 to 9.0. At the time of that study, the Arequipa earthquake was the largest subduction earthquake for which strong motion recordings were available. Previously, Cohee et al. (1991) Somerville et al. (1991) performed similar ground motion simulation studies for Mw 8.0 Cascadia earthquakes based on the recorded ground motions of the 1985 Mw 8.0 Michoacan, Mexico and Valparaiso, Chile earthquakes.

EARTHQUAKE SOURCE SCALING RELATIONS OF SUBDUCTION EARTHQUAKES

Somerville et al. (2002) developed scaling relations for the source parameters of subduction earthquakes, based on the rupture models of seven large subduction earthquakes. These models are analogous to those we developed for crustal earthquakes (Somerville et al., 1999). The subduction earthquakes used in these scaling relations include three earthquakes whose rupture models we developed: 1923 Tokyo, Japan (Wald and Somerville, 1995); 1944 Tonankai, Japan (Ichinose et al., 2003); and 2001 Peru (Somerville et al., 2003). The rupture models portray the spatial and temporal distribution of slip on the fault plane, as inferred from strong motion recordings, teleseismic data, and in some cases geodetic and tsunami observations. The scaling relations describe the scaling with seismic moment of rupture area, rise time, asperity dimensions, and the corner periods of spatial wavenumber models of fault slip heterogeneity, which control the spatial distribution of slip and slip velocity.

Somerville et al. (2002) measured the rise time of subduction earthquakes based on the maximum slip velocity (Ishii et al., 2002). They found that the rise time for subduction earthquakes is given by:

$$T_r = 1.8 \times 10^{-9} \, M_o^{1/3} \qquad (1)$$

PROCEDURE FOR BROADBAND STRONG GROUND MOTION SIMULATION

We use a hybrid broadband ground motion simulation approach, based on frequency-wavenumber Green's functions for long periods (> 3s) and on a partly stochastic ray theory method (Somerville et al., 1991) for shorter periods, to simulate broadband ground motions for large subduction earthquakes. We showed in earlier work that the short period simulation procedure successfully reproduces the recorded ground motions of the **M** 8.0 Valparaiso, Chile and Michoacan, Mexico earthquakes of 1985 (Somerville et al., 1991) as well as of the **M** 8.4 Arequipa, Peru of 2001 earthquake (Somerville et al., 2008), and on that basis we applied it to simulate the ground motions of **M** 8.0 Cascadia earthquakes (Cohee et al., 1991). Specifically, we used the Caleta de Campos rock site recording of an aftershock of the 1985 Michoacan, Mexico earthquake as an empirical source function in the simulations, described in detail by Cohee et al. (1991).

In the hybrid broadband simulation procedure, the low frequency and high frequency components of the ground motions are computed separately and then combined using matched filters. The low frequency simulation methodology, used for periods longer than 0.3s or 1.0s, uses a deterministic representation of source and wave propagation effects (Graves and Pitarka, 2004) that is based on the approach described by Hartzell and Heaton (1983). The basic calculation is carried out using a 1D frequency-wavenumber integration algorithm.

The earthquake source is specified by a kinematic description of fault rupture, incorporating spatial heterogeneity in slip, rupture velocity and rise time. Following Hartzell and Heaton (1983), the fault is divided into a number of subfaults. The slip and rise time are constant across each individual subfault, although these parameters are allowed to vary from subfault to subfault. We use a slip velocity function that is constructed using two triangles as shown in Figure 1.
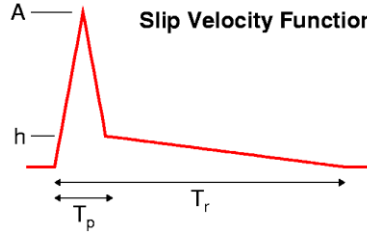
Figure 1. Slip velocity function used in the deterministic simulations [see equation (1)].

This functional form is based on results of dynamic rupture simulations (e.g., Guatteri et al., 2003). We constrain the parameters of this function as follows:

$$T_r = 1.83x10^{-9} \cdot M_0^{-1/3}$$
$$T_p = 0.2 \cdot T_r \qquad\qquad (2)$$
$$h = 0.2 \cdot A$$

where M_0 is the seismic moment, T_r is the rise time and A is normalized to give the desired final slip. The expression for T_r comes from the empirical analysis of Somerville et al. (1999). The rupture initiation time (T_i) is determined using the expression:

$$T_i = \frac{R}{V_r} - \delta t$$
$$\qquad\qquad (3)$$
$$V_r = 0.8 \cdot V_s$$

where R is the rupture path length from the hypocenter to a given point on the fault surface, V_r is the rupture velocity and is set at 80% of the local shear wave velocity (V_s), and δt is a timing perturbation that scales linearly with slip amplitude such that δt = δt$_0$ where the slip is at its maximum and δt=0 where the slip is at the average slip value. For these calculations, we set δt=0.1s. This scaling results in faster rupture across portions of the fault having large slip as suggested by source inversions of past earthquakes (Hisada, 2001).

For scenario earthquakes, the slip distribution can be specified using randomized spatial fields, constrained to fit certain wave number properties (e.g., Somerville et al., 1999; Mai and Beroza, 2002). In the simulation of past earthquakes, we use smooth representations of the static slip distribution determined from finite-fault source inversions. Typically, these inversions will also include detailed information on the spatial variation of rupture initiation time and slip velocity function, either by solving for these parameters directly or by using multiple time windows. However, we do not include these in our simulations of scenario earthquakes, but rather rely on equations (2) and (3) to provide them. This is because the level of detailed resolution of these parameters provided by the source inversions will generally not be available a priori for future earthquakes. Furthermore, since the inversions determine these parameters by optimally fitting the selected observations, it is not clear that they will produce an optimal waveform fit at sites not used in the inversion.

The high frequency simulation methodology, used for periods shorter than 0.3s or 1.0s, is a stochastic approach that sums the response for each subfault using empirical source functions. The simulation procedure was originally developed by Somerville et al. (1991) following the concepts of Irikura (1978) and Hartzell (1978).

The crustal structure model used in the simulations has a median Vs_{30} (average shear wave velocity for the upper 30m) of 434 m/s, consistent with the average Vs_{30} value of the strong motion sites that recorded the Maule earthquake. The generated ground motion maps and all comparisons with the available GMPEs are presented for sites with Vs_{30} of 434 m/s and 181 m/s (lower boundary of NEHRP site category D). To adjust the simulations for Vs of 434 m/s to the lower surface shear wave velocity of 181m/s, we used the NEHRP amplitude and period dependent amplification factors to scale the response spectra.

GROUND MOTION MODELS

We compare the ground motion estimates obtained in this report with three ground motion models for subduction earthquakes. These three models are Atkinson and Boore (2003), Zhao et al. (2006) and Abrahamson et al. (2012). The Atkinson and Boore (2003) and Abrahamson et al. (2012) models were derived from worldwide sets of strong motion recordings of subduction earthquakes and the Zhao et al. (2006) model was derived from strong motion recordings from earthquakes in Japan. We compare our results for sites with Vs_{30} = 434 m/s with the relations of Atkinson and Boore (2003) and Abrahamson et al. (2012) derived for the specific Vs_{30} and with the SC II relations of Zhao et al. (2006). For the D site condition, we use the D relations of Atkinson and Boore (2003) and Abrahamson et al., 2012 and the SC III relations of Zhao et al. (2006).

In this report, we also fit a simple ground motion model to the simulations. The ground motion model has the form:

$\ln(\text{Sa}) = C_1 + C_2 \times R_{cld}$ (4)

where C_1 and C_2 are the regression coefficients and R_{cld} is the closest distance from the rupture.

THE M 8.8 MAULE, CHILE EARTHQUAKE OF FEBRUARY 27, 2010

The **M** 8.8 Maule, Chile earthquake of February 27, 2010 is one of the largest earthquakes for which strong ground motion recordings have ever been obtained. The purpose of this section of the report is to find out whether the simulation procedures for ground motions and tsunami wavefields reproduce the recorded features of the **M** 8.8 2010 Chile earthquake. The earthquake and fault parameters from the 2010 Chile earthquake, as published by the USGS, are listed in Table 1.

**Table 1. Earthquake information and fault model adopted for the Maule earthquake.**

Earthquake Parameters / Fault Model	
Origin Time	06:34:14 UTC
Location	36.12° S, 72.90° W
Depth	35 km
M	8.8
Strike, dip	9, 12

We used the earthquake rupture model of Lorito et al. (2011) to simulate the ground motions and tsunamis of the Maule earthquake. This rupture model was derived from both tsunami and geodetic data, shown in Figures 2 and 3. The rupture zone of the earthquake was about 625 km along strike and 200 km down dip, and most of the slip occurred in two asperities, adjacent to the earthquake hypocenter at a depth about 35km.
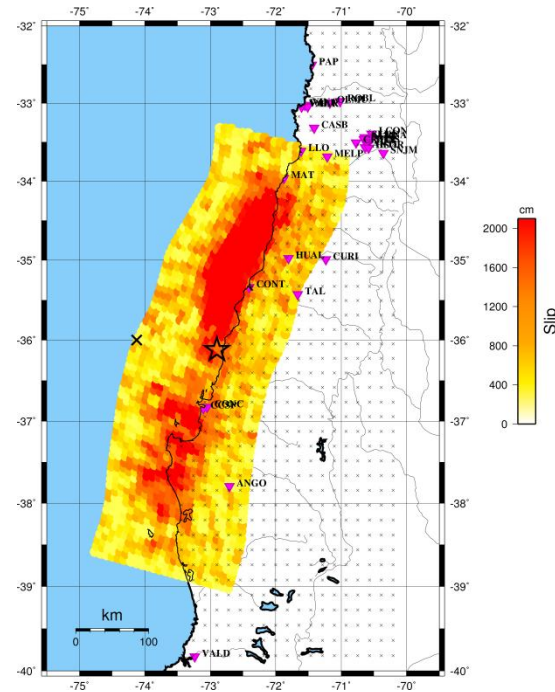
Figure 2. Rupture model of the Mw 8.8 Maule, Chile earthquake of 2010, showing the slip distribution of Lorito et al. (2011), the locations of strong ground motion recording stations, and the grid of stations used for simulations.

Figure 3 shows the final rupture model used for broadband simulations. The original rupture model from Lorito et al. (2011) was modified to take account of the rupture times in which the dependence of rupture velocity on slip described in the preceding section and has been interpolated at one third the sampling interval of the original slip model. The average slip in the interpolated model was about 413 cm, while the maximum slip was 2143 cm.
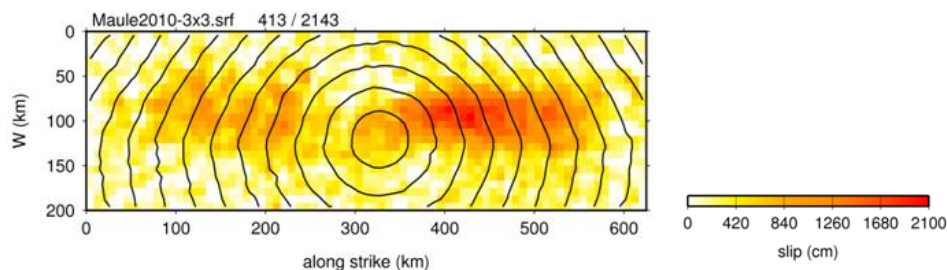
Figure 3. Rupture model of the Mw 8.8 Maule, Chile earthquake of 2010.

Strong motion recordings of the Chile earthquake were obtained at 21 several stations whose locations are shown in Figure 2 and listed together with the Vs_{30} in Table 2 (information from Boroschek and Contreras, 2012).

Table 2. Strong motion recordings of the 2010 Maule earthquake

Station	Abbrev	Latitude	Longitude	Orientation (degrees)	Vs_{30} (m/s)
COPIAPÓ-Hospital	COPI	-27.374	-70.322	0	-
VALLENAR-Liceo Santa Marta	VALLE	-28.576	-70.755	0	-
PAPUDO	PAP	-32.507	-71.448	60	517
VIÑA DEL MAR-Centro	VINA	-33.025	-71.553	0	273
VALPARAÍSO-UTFSM	VALU	-33.035	-71.596	180	1421
VIÑA DEL MAR-Puente Marga Marga	MAR	-33.048	-71.510	0	280
VALPARAÍSO-Almendral	VAL	-33.048	-71.604	310	360
SANTIAGO-Conjunto Villa Andalucía	SANT	-33.467	-70.652	270	-
PEÑALOLÉN-Hospital Luis Tisné	HTIS	-33.501	-70.579	0	452
MAIPÚ-Centro de Referencia de Salud	CRMA	-33.509	-70.772	0	450
LA FLORIDA-Metro Línea 5 Estación Mirador	MET	-33.514	-70.606	0	685
PUENTE ALTO-Hospital Sótero del Río	HSOR	-33.577	-70.581	0	-
LLOLLEO	LLO	-33.616	-71.611	340	305
MATANZAS-Escuela Carlos Ibáñez del Campo	MAT	-33.960	-71.873	0	400
HUALAÑÉ-Hospital	HUAL	-34.977	-71.805	0	527
CURICÓ-Hospital	CURI	-34.990	-71.236	150	540
CONSTITUCIÓN-Hospital	CONT	-35.340	-72.406	0	340
TALCA-Colegio Integrado San Pío X	TAL	-35.430	-71.665	0	640
CONCEPCIÓN-Colegio Inmaculada Concepción	CONC	-36.828	-73.048	60	230
ANGOL-Hospital	ANGO	-37.795	-72.706	0	325
VALDIVIA-Hospital	VALD	-39.831	-73.239	0	-

We used the Lorito et al. (2011) rupture model of the 2010 Chile earthquake to simulate broadband ground motions at the twenty one strong motion recording sites, and at the grid of stations shown in Figure 2. The matching of the low and high frequency components of the simulated ground motions was performed at 0.3Hz (3s) following the testing of several trial values. This selection was based on comparisons with the available recordings, which were strongly influenced at the longer periods by the high-pass filter applied to the recordings (f_{cut} = 0.25Hz – 4s). We compared the recorded and simulated ground motions at the recording stations, and analyzed the ground motions simulated over the grid.

CRUSTAL STRUCTURE MODEL

The crustal velocity model that we used, which is listed in Table 3, was derived from the results of Ocola et al. (1995). This model was modified to include a shallow layer of low seismic velocity representing weathered rock. We found that the amplitudes of the ground motions simulated using this velocity model are in agreement with the observed ground motion amplitudes at the recording stations, which have an average Vs_{30} of 434 m/s.

Table 3. Crustal structure model for Chile (modified from Ocola et al., 1995

Thickness (km)	V_p (m/s)	V_s (m/s)	Density (Kgr/m^3)	Q_p	Q_s
0.2	2600	1500	2.00	40	20
6.7	5300	3030	2.10	200	100
4.6	6000	3370	2.50	500	200
18.1	6500	3650	2.78	500	200
15.8	7300	4100	3.18	1600	500

COMPARISON OF RECORDED AND SIMULATED GROUND MOTIONS - 2010 MAULE EVENT

In Figure 4, we compare the recorded response spectra of the 2010 Maule earthquake with the predictions of Zhao et al. (2006) (Zhao06) ground motion model. The comparisons of the recorded values with the Zhao06 model are in close agreement for the majority of the stations studied and for the selected period range (0.01-4s). For closer distances (<80km) the simulated values tend to be lower than the Zhao06 model for that period range.
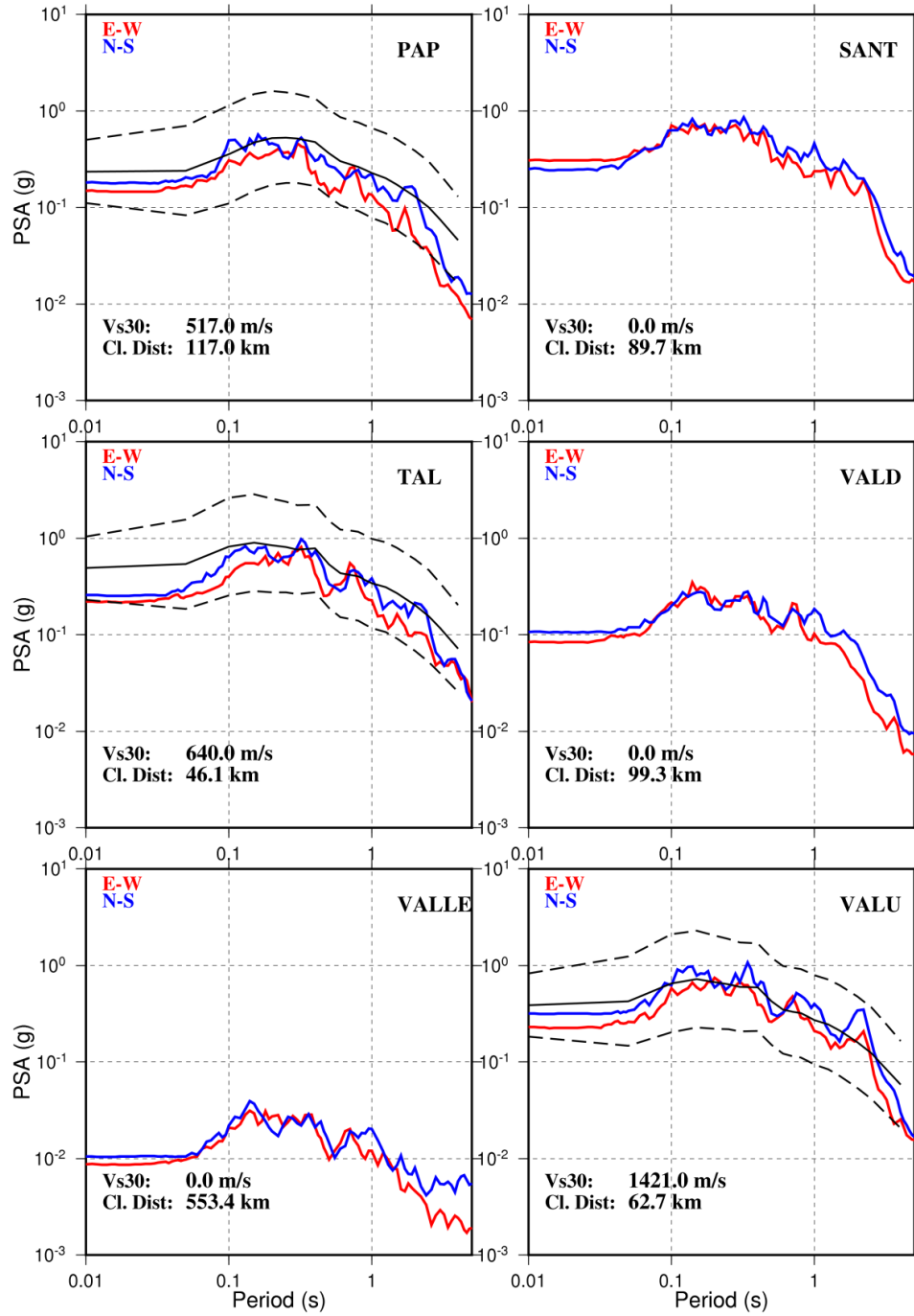
Figure 4. Comparison of the recorded response spectra of the 2010 Maule earthquake with the median and +/- one sigma levels of the Zhao et al., 2006 ground motion prediction model.
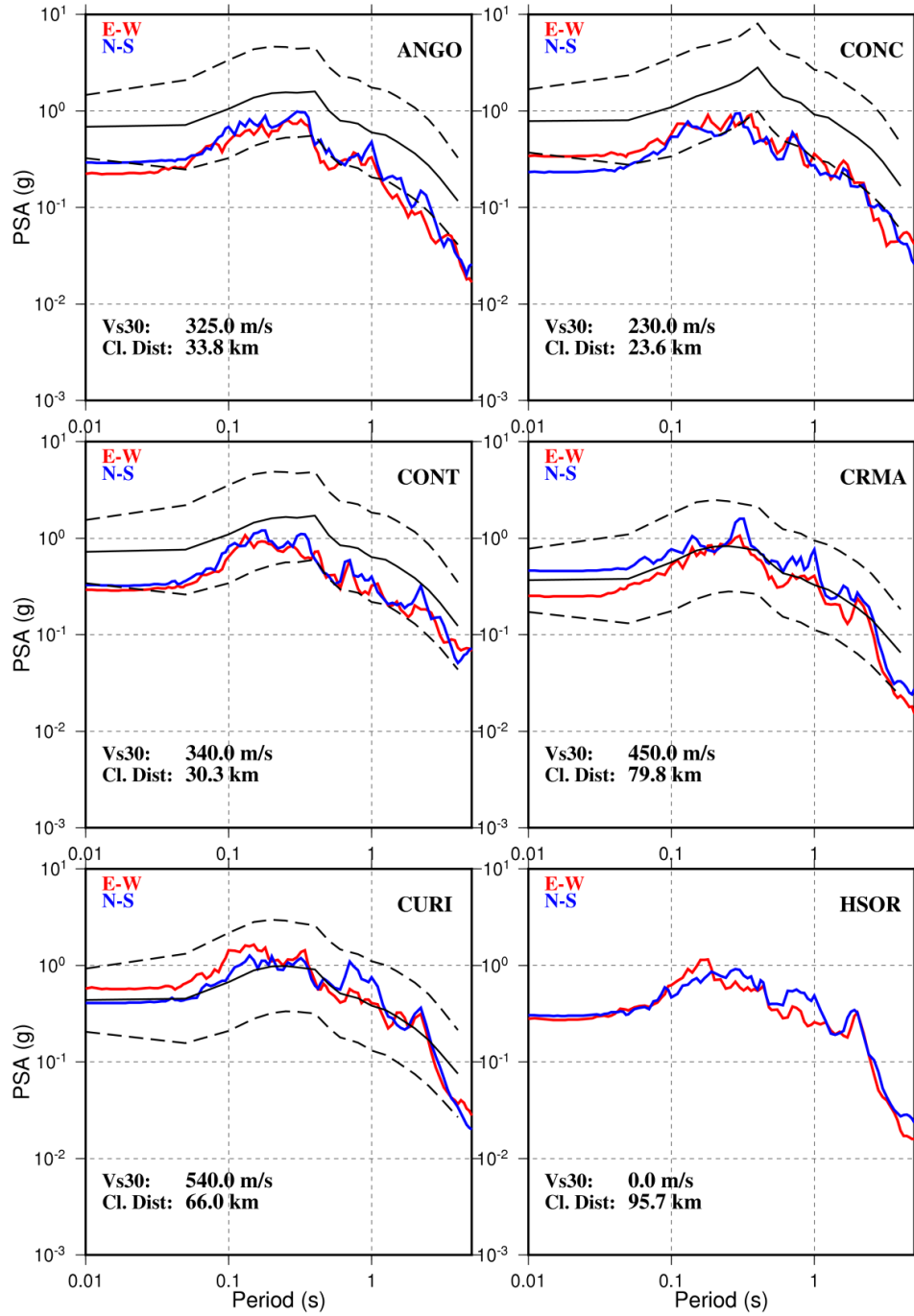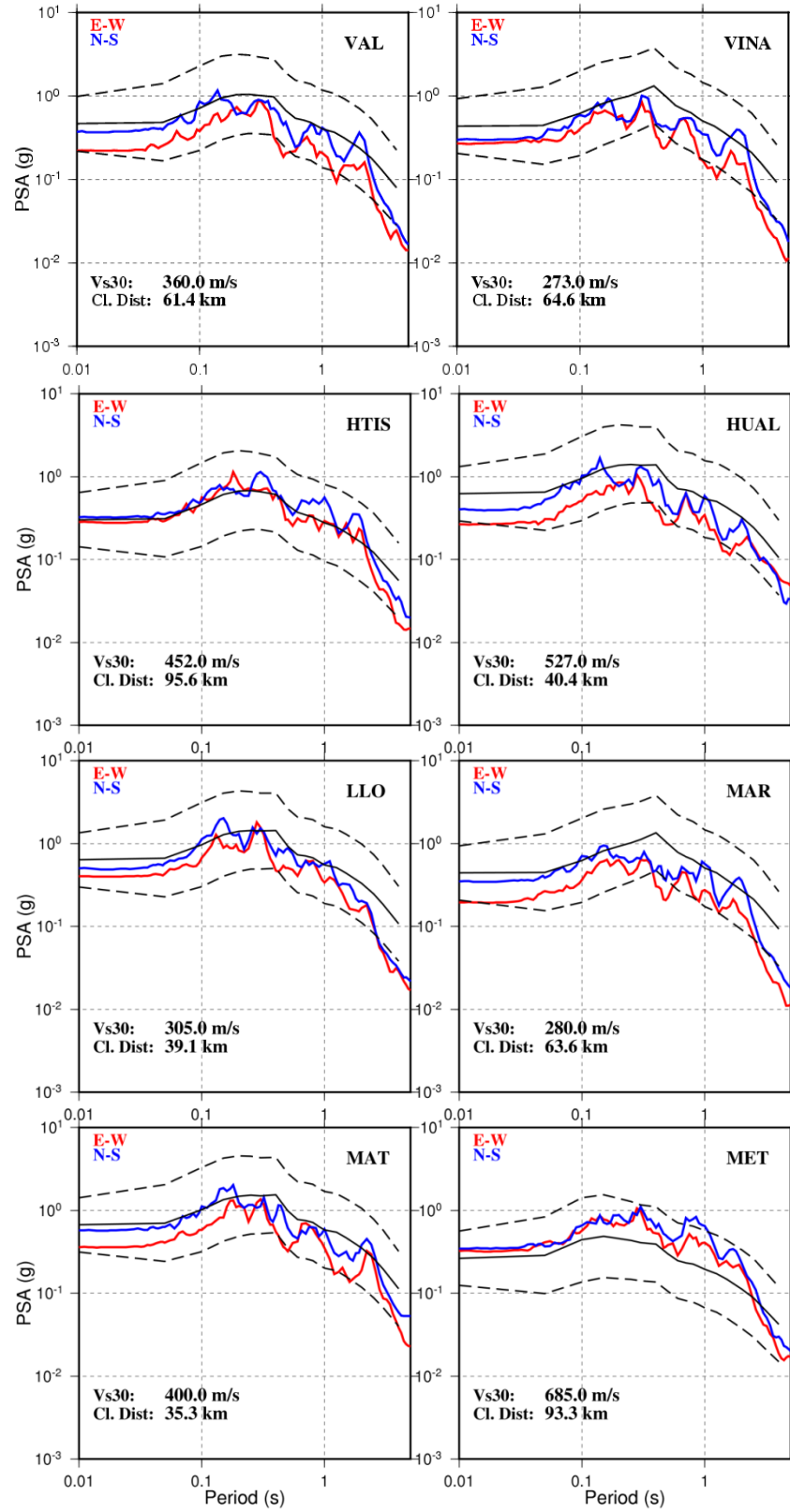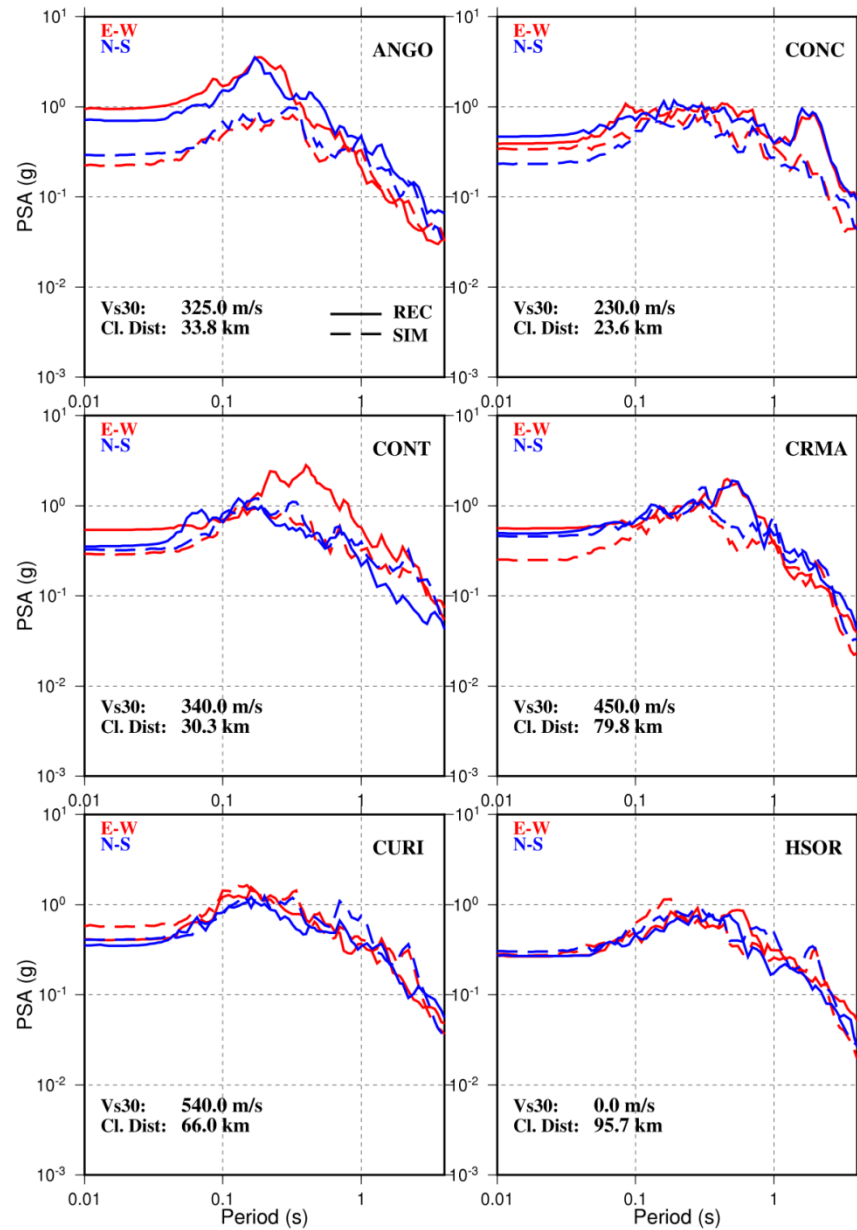
Figure 4. Cont.

Figure 4. Cont.

The recorded and simulated response spectra at each station are compared in Figure 5. The agreement is quite good for most of the stations except at stations VALU and MET, where the simulations overpredict the data, and for stations ANGO and VALLE where the simulations underpredict the data.

Figure 5. Comparison of the simulated (dashed lines) and recorded (solid lines) response spectra of the 2010 Maule earthquake.
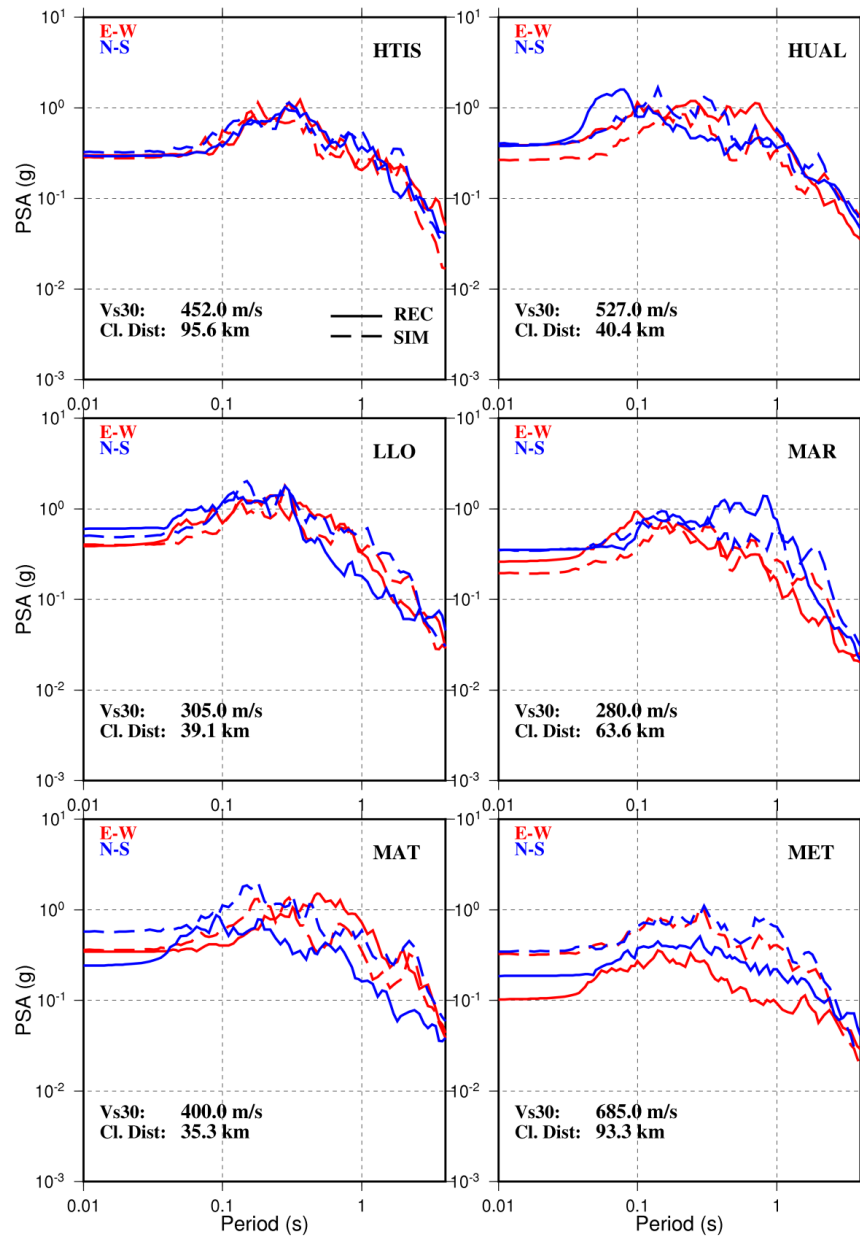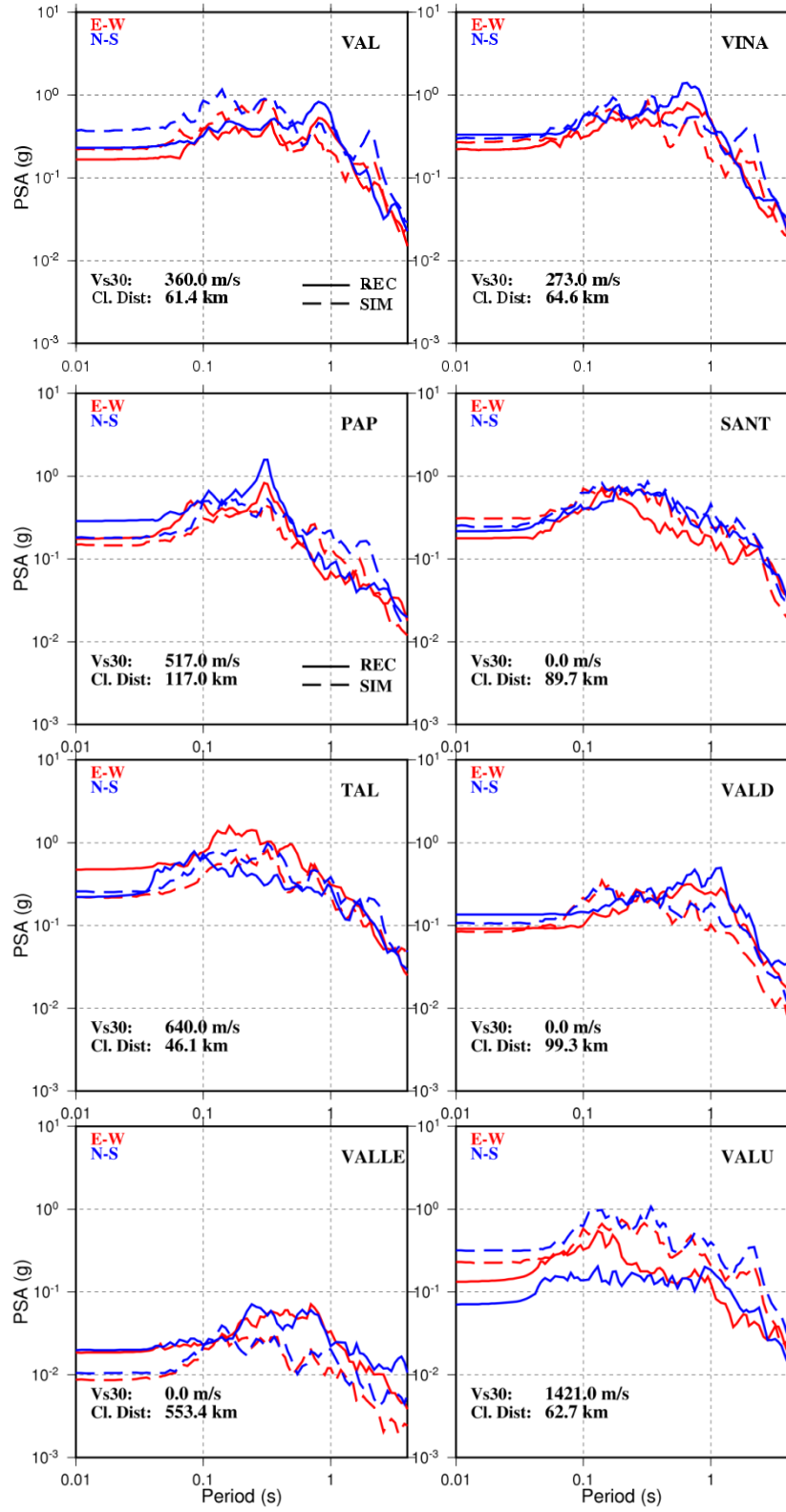
Figure 5. cont.

Figure 5. Cont.

Figure 6 shows the goodness of fit between the recordings and simulations at all of the stations, following the procedure of Abrahamson et al. (1990). The grey shading shows the 90th percentile confidence interval in the median prediction. Results are presented for periods up to 4s due to the high-pass filtering applied in the recordings (f_{cut} = 0.25Hz - 4s). There is little systematic bias in the prediction of the ground motions, although there is some underprediction at a period of 0.5 seconds and some overprediction between 1 and 2 seconds, especially on the North component. The standard deviation of the difference between recorded and simulated values, shown by the green shading, is about a factor of 1.5 (0.4 natural log units).
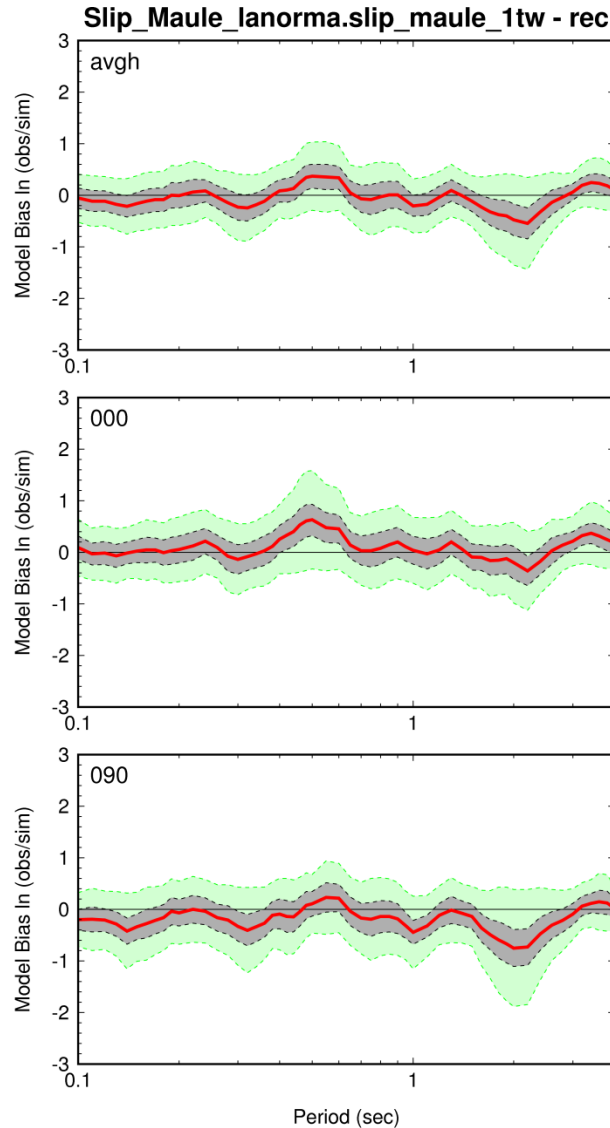

Figure 6. Goodness of fit of recorded and simulated response spectra of the 2010 Maule earthquake for average, North and East components. The red line shows the bias, the green zone shows the standard deviation, and the grey zone shows the standard deviation of the mean.

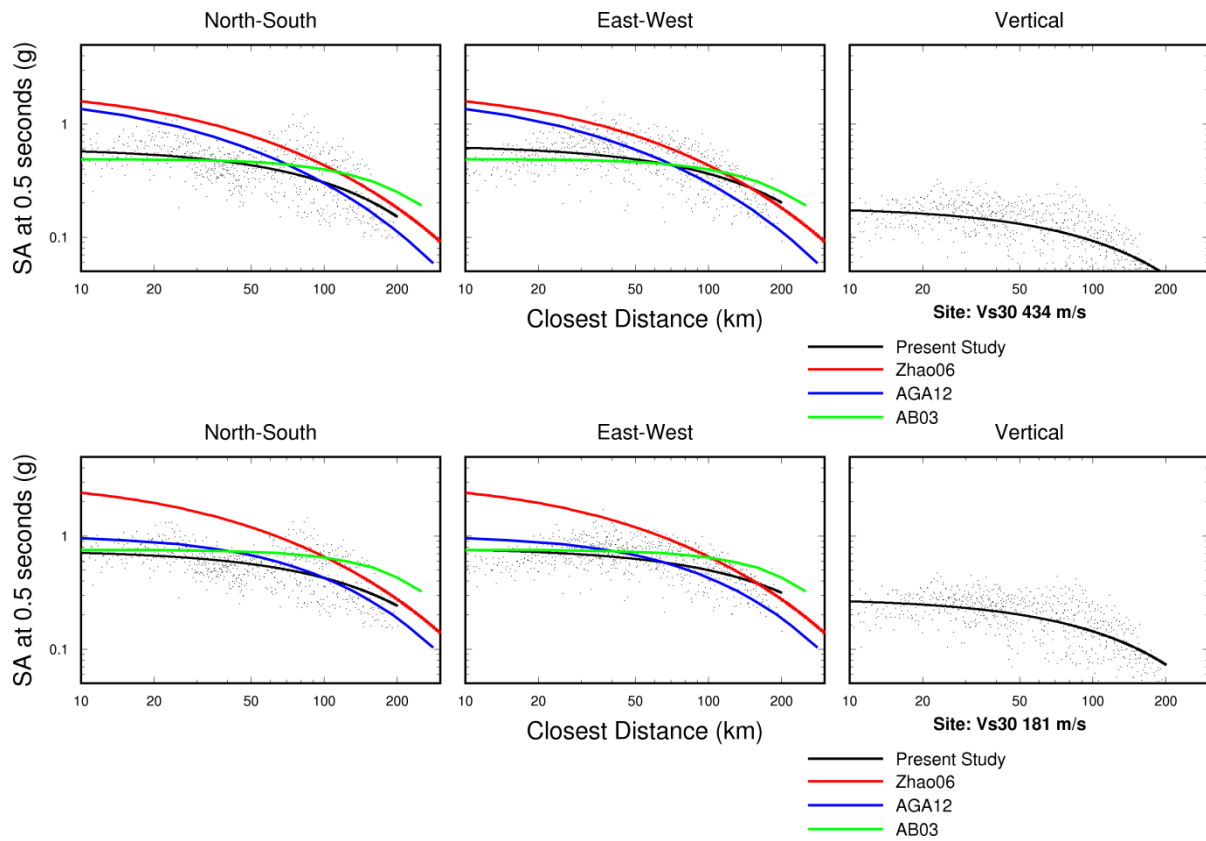## SIMULATED GROUND MOTIONS OF THE 2010 MAULE EARTHQUAKE

The comparisons described above have demonstrated the performance of our strong motion simulation procedure in matching the recorded ground motions of the **M** 8.8 Maule earthquake. This forms the basis for using the simulated ground motion values from the grid of stations (shown in Figure 2) in order to study the strong ground motion characteristics in the study area. The attenuation of ground motion in the study area is shown in Figures 7 through 11 for peak acceleration and for 0.2s, 0.5s, 1s and 2s response spectral acceleration periods. The top panel of each figure shows the attenuation for sites with Vs_{30} of 434 m/s and the bottom panel shows the attenuation for deep soil (Vs_{30} 181 m/s) site conditions. The agreement between the simulations and ground motion models is quite close for peak acceleration, but at 0.5 seconds the simulations underpredict the models. At 1 and 2 seconds the simulations are in very good and fairly good agreement with the models, respectively. The closest agreement of the simulations with the different ground motion models is with the Zhao et al. (2006) and Abrahamson et al. (2012) models, while there is poorer agreement with the Atkinson and Boore (2003) model, except for 0.5s. Similar period-dependent trends were found with respect to the strong motion recordings, as shown in Figure 6. The rate of attenuation of the simulations is more gradual than that of Zhao06 and AGA12, and more comparable to that of AB03.
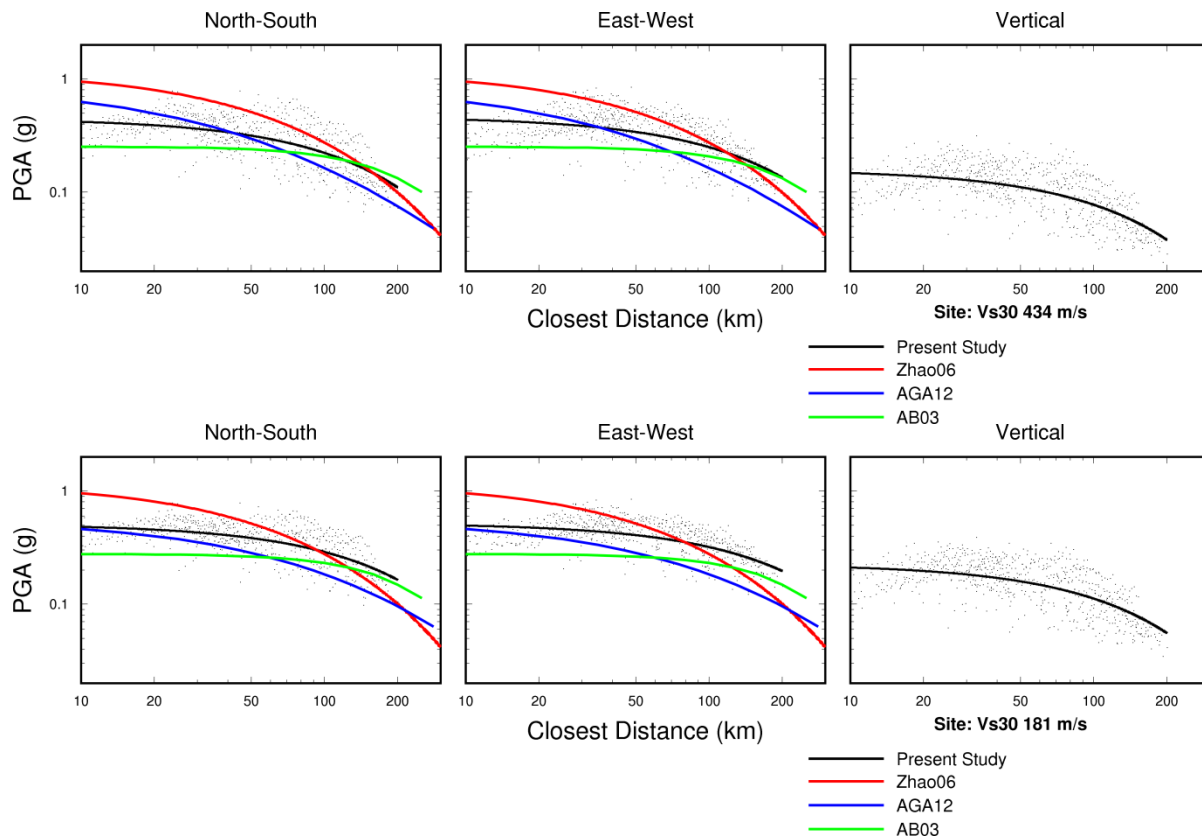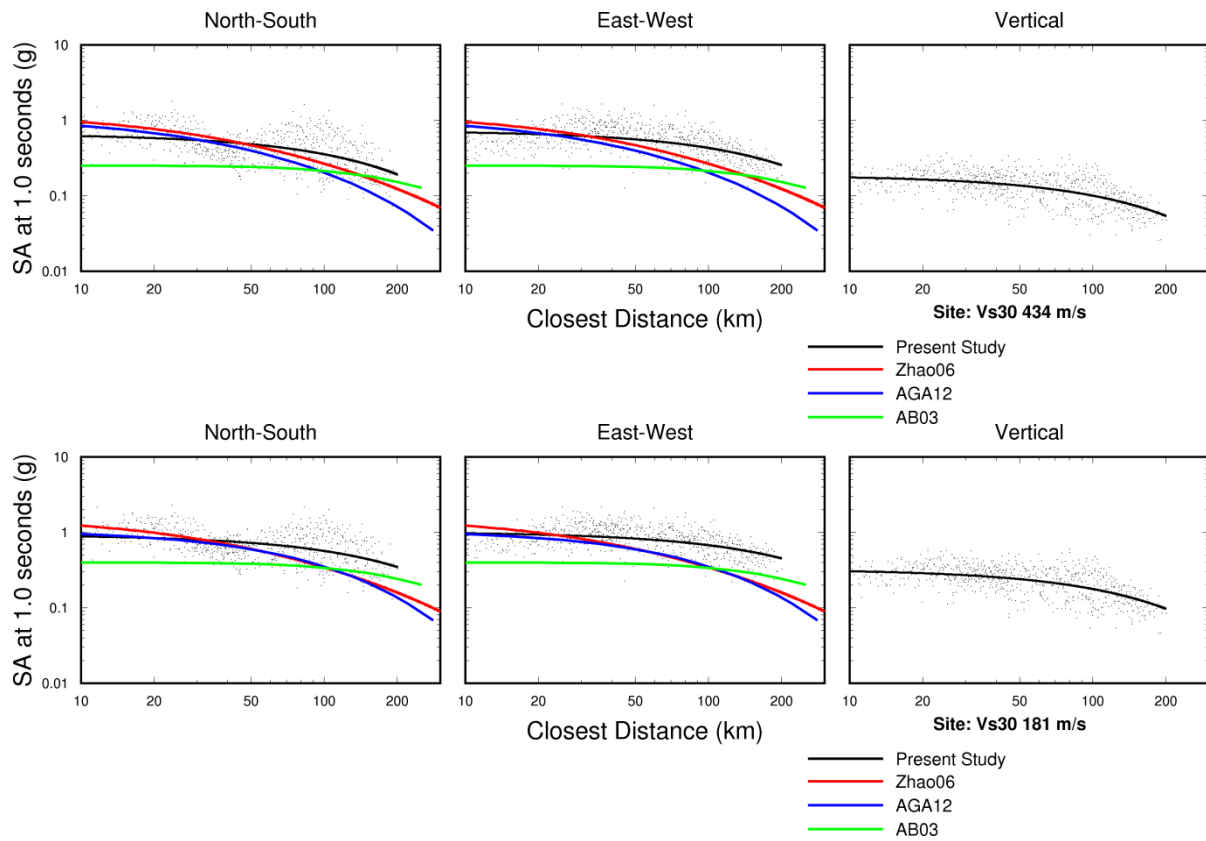

Figure 7. Comparison of simulated peak accelerations (small black dots and black line) for 2010 Maule earthquake with ground motion models.
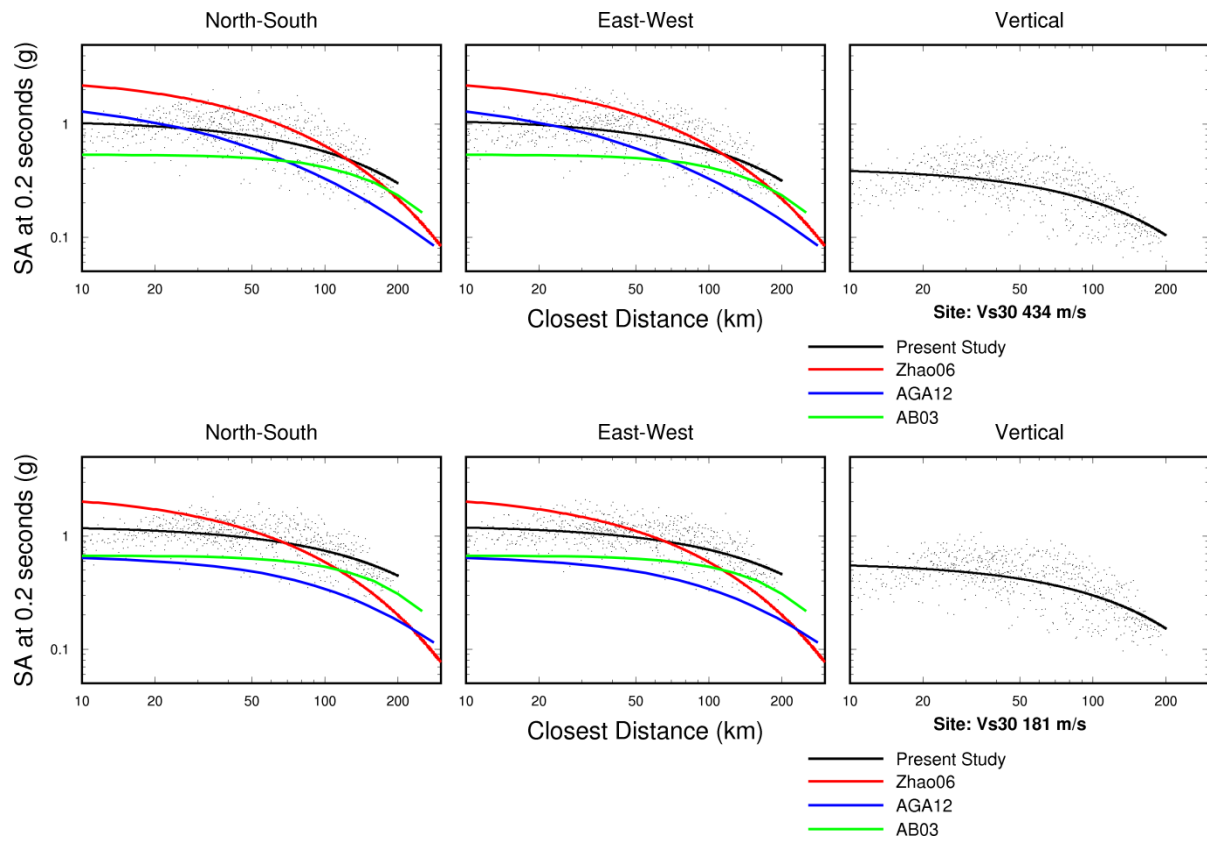
Figure 8. Comparison of simulated 0.2s spectral accelerations (small black dots and black line) for the 2010 Maule earthquake with ground motion models.
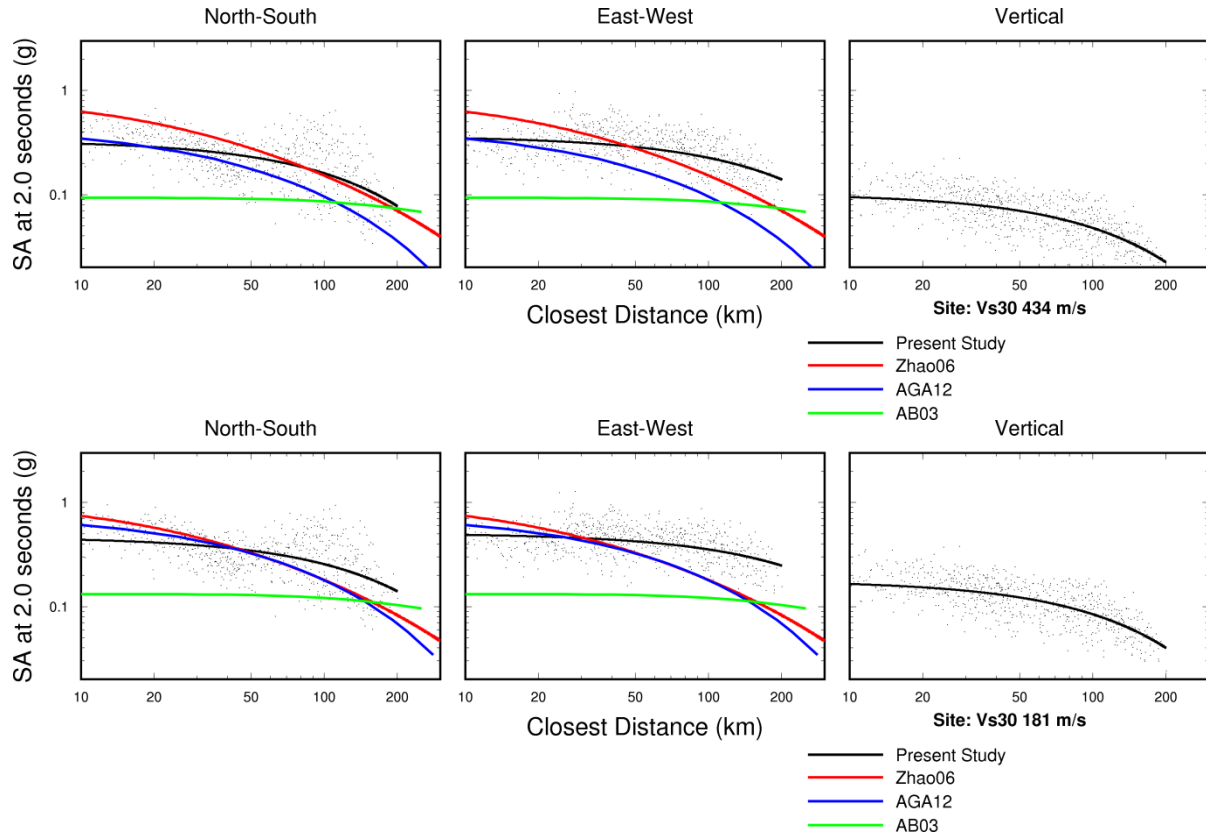
Figure 9. Comparison of simulated 0.5s spectral accelerations (small black dots and black line) for the 2010 Maule earthquake with ground motion models.
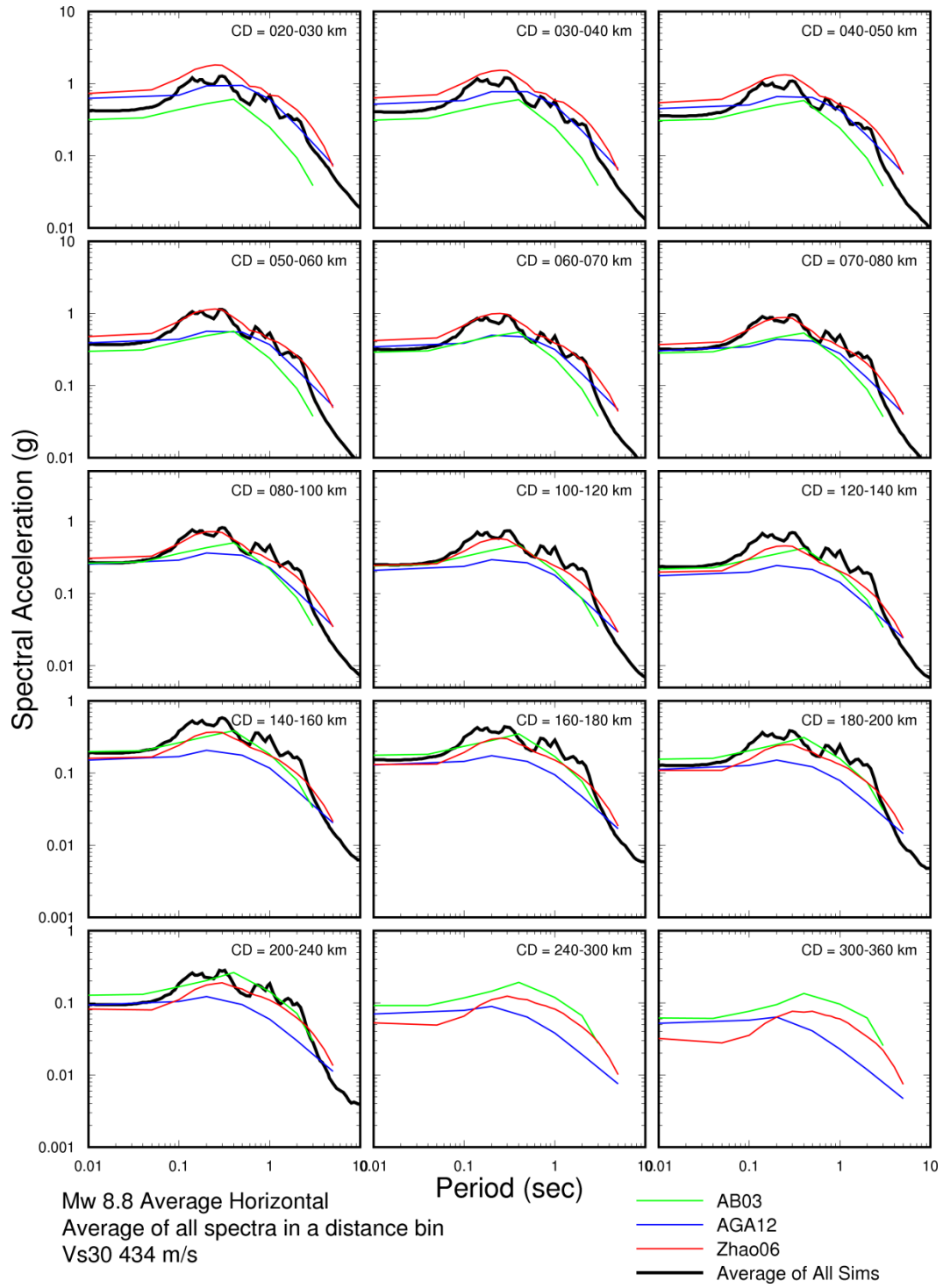
Figure 10. Comparison of simulated 1s spectral accelerations (small black dots and black line) for the 2010 Maule earthquake with ground motion models.
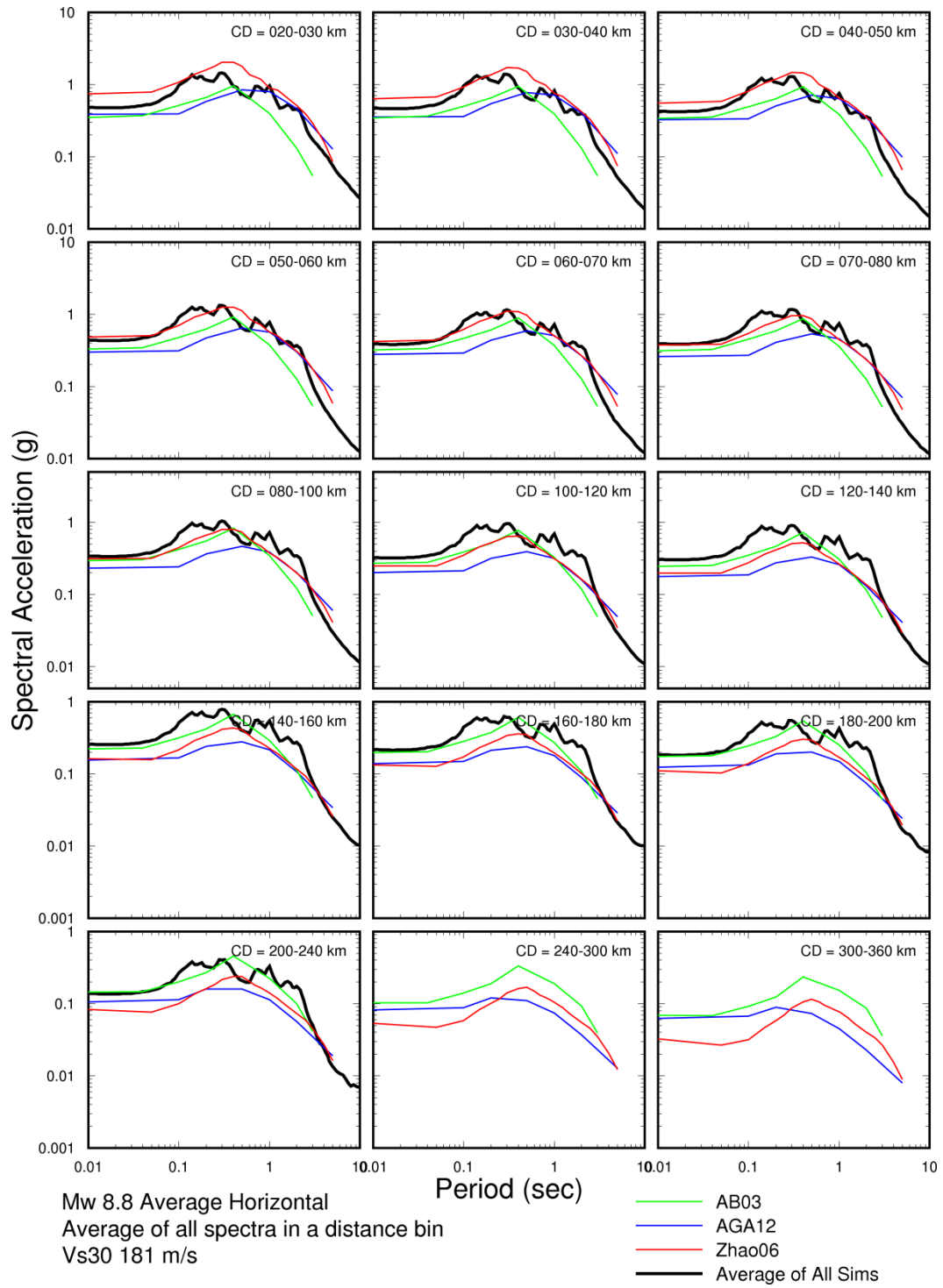
Figure 11. Comparison of simulated 2s spectral accelerations (small black dots and black line) for the 2010 Maule earthquake with ground motion models.

The average horizontal response spectra of the simulations of the 2010 Maule earthquake are compared with three ground motion models in a suite of distance ranges in Figures 12 and 13 for sites with Vs_{30} of 434 m/s and 181 m/s respectively. There is fairly good agreement in response spectral shape with all three models studied, depending on the distance and site conditions, with the Zhao et al. (2006) providing the best overall fit in response spectral shape.

Figure 12. Comparison of average horizontal simulated response spectra for a suite of distance ranges for the 2010 Maule earthquake for sites with Vs$_{30}$ of 434 m/s with three ground motion models.

Figure 13. Comparison of average horizontal simulated response spectra for a suite of distance ranges for the 2010 Maule earthquake for site with Vs$_{30}$ of 181 m/s with three ground motion models.

EARTHQUAKE SOURCE CHARACTERIZATION OF Mw 9 CASCADIA SUBDUCTION EARTHQUAKES

This section of the report describes the modeling of Mw 9.0 subduction earthquakes that rupture the entire Cascadia subduction zone. The geometry of the Cascadia earthquake source models used in this report was based on the source characterization of Petersen et al. (2008). In particular, we used their "base" model of the bottom of the seismogenic plate interface, shown in Figure 12, to which they gave a weight of 0.5. This model is based on the global observation that rupture usually extends down to depths of about 30 km. Petersen et al (2008) gave weights of 0.1, 0.2 and 0.2 to the alternative models "top," "middle," and "bottom" respectively, which are also shown in Figure 12. The sensitivity of the calculated seismic hazard to uncertainty in the model for the bottom of the seismogenic zone was analyzed by Petersen et al. (2002). This depth controls the eastern extent of the subduction source, and thus has a strong influence on ground motion levels in the urban regions of Washington and Oregon, which mainly lie to the east of the source.
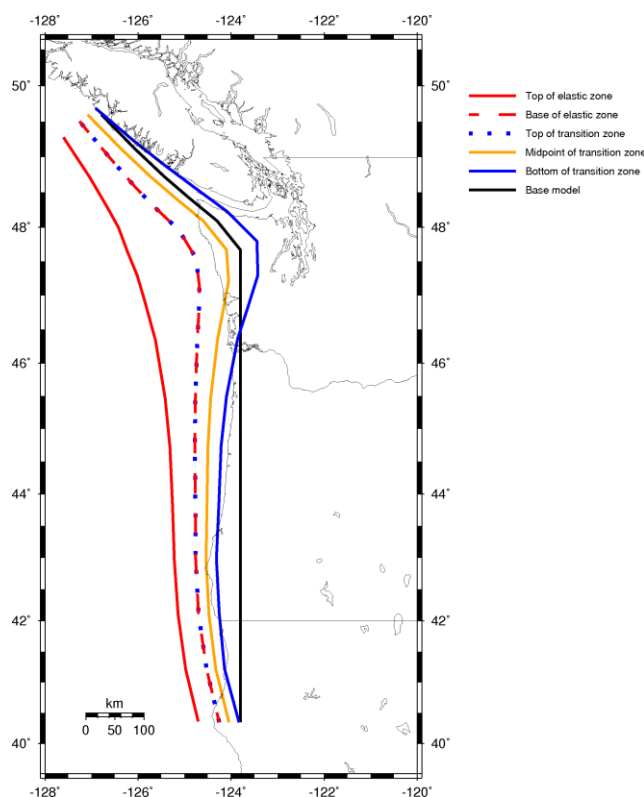

Figure 14. Alternative models of the downdip extent of the Cascadia subduction zone. Source: Petersen et al. (2008). This study used the base model based on global data, shown by the thick black line.

The fault geometry used to represent the base model is shown in Figure 13. The subduction interface was divided into three segments to accommodate the shallower dip at the bend in the subduction zone near the Olympic Peninsula. The shallower segment has a downdip width of 160 km

while the other segments have downdip widths of 120 km. The rupture area of the combined fault segments is 131,500 square km.

Petersen et al. (2008) assume that such earthquakes have magnitudes in the range of 8.8 to 9.2, with a weight of 0.6 given to magnitude 9.0, and weights of 0.2 given to magnitudes of 8.8 and 9.2. Based on the recent megathrust earthquakes that occurred worldwide, this assumption seems to be validated and accordingly, we perform simulations for an earthquake of magnitude **M** 9.0.
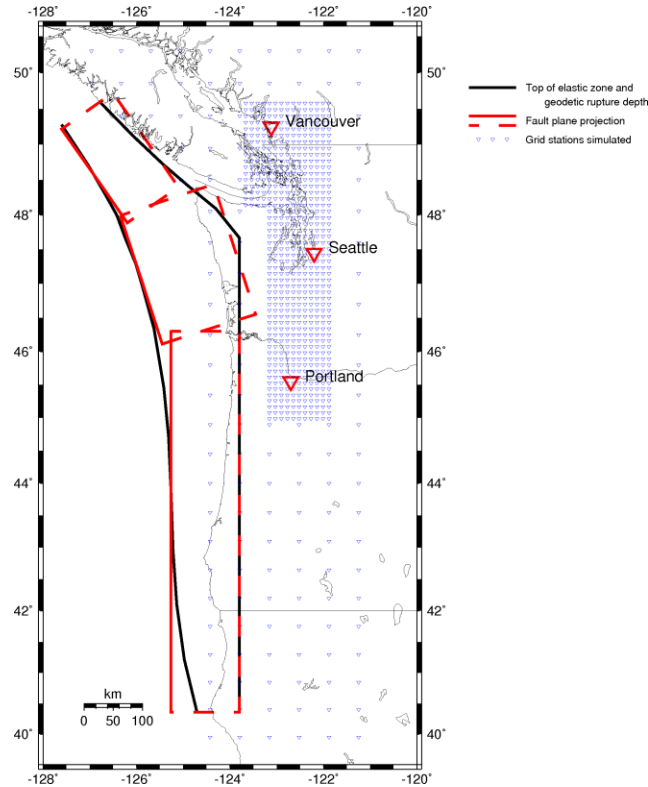
Figure 15. Modeled rupture geometry of the Cascadia subduction zone and the grid of stations used for strong motion simulation (blue triangles).

However, we note that the relations between seismic moment and rupture area of subduction earthquakes derived by Somerville et al. (2002) from the rupture models of past earthquakes predict that the magnitude corresponding to a rupture area of 131,500 square km is **M** 8.7. Consequently the source parameters of an earthquake with **M** 9.0, listed in Table 4, do not conform to the self-similar scaling relations of Somerville et al. (2002).

For the event listed in Table 4, we generated ten different earthquake rupture models, for three different hypocentral locations, i.e. south, central and north, in order to study the variability and the sensitivity of the derived ground motions and tsunami inundation to the individual characteristics of each slip model used.

Table 4. Source parameters of modeled M 9.0 earthquakes that rupture the whole Cascadia Subduction Zone.

M	Rupture Area (km^2)	Average Slip (cm)	Rise Time (s)	Slip Velocity (cm/s)
9.0	131,500	831	12.7	66.0

The rupture models of the **M** 9.0 event for the north hypocenter are shown in Figure 16.

Slip Models for M=9.0
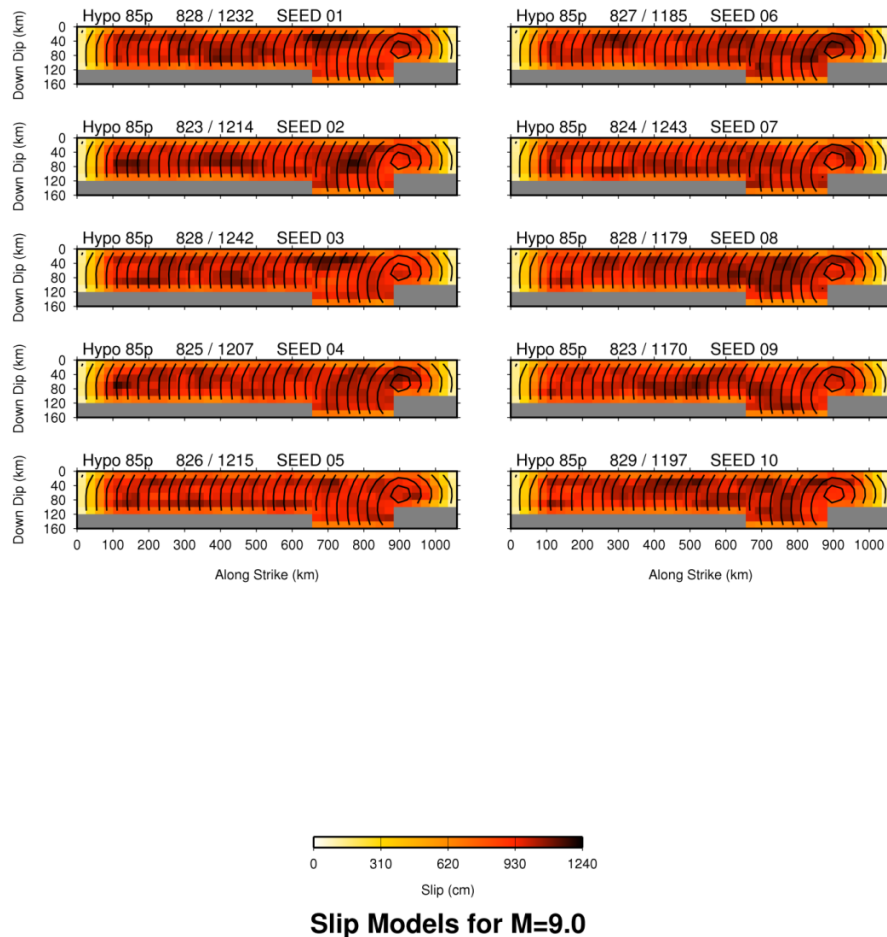
Figure 16. Rupture models of M 9.0 scenario earthquakes on the Cascadia subduction zone. The slip values of all models are the same for the different hypocenters (southern, central, and northern). The minimum slip of all models is 823 cm and the maximum slip is 1243 cm.

We selected slip models 01, 03, 05 and 09 for producing ground motion and tsunami simulations. Models 01 and 09 represent the two extremes in the estimated maximum slip (1232 cm and 1170cm, respectively) while models 05 and 09 were selected for studying the effects of the variability of slip distribution patterns on the simulated grounds motions. The high and low frequency components of the simulated ground motions were combined using matched filters with characteristic frequency of 1Hz.

CRUSTAL STRUCTURE

In a previous study in which we simulated the ground motions of Cascadia subduction earthquakes, we demonstrated the adequacy of Green's functions computed using a series of 1D approximations to a 2D seismic velocity model of the Cascadia subduction zone by comparing the 1D and 2D Green's functions (Cohee et al., 1991). The 2D model used a simple model of the subcrustal structure from the Lithoprobe transect (Clowes et al., 1987). Subsequent work by Brocher et al. (2003) and McNeill et al. (2004) indicates the presence of a serpentinized forearc upper mantle along the Cascadia margin. This forearc has significantly lower seismic velocities than those of Clowes et al. (1987) used in the ground motion study by Cohee et al. (1991).

McNeill et al. (2004) analyzed the effect of a serpentinized forearc upper mantle along the Cascadia margin on ground motions from megathrust earthquakes, and concluded that it has a relatively minor effect. It alters the distance range over which postcritically reflected S waves dominate by shifting the reflecting interface from the continental Moho to the oceanic Moho, but does not significantly affect the amplitudes. Accordingly, we conclude that it is not critical to use full 2D or 3D Green's functions in our simulations, and so we used Green's functions computed using a 1D approximation to the velocity model of the Cascadia subduction zone. We found that the velocity model we used for Peru is broadly compatible with the velocity model for Cascadia described McNeill et al. (2004). This velocity model, which has velocities that are considerably lower than those used by Cohee et al. (1991), is shown in Table 5. In Chile, we found that the amplitudes of the ground motions simulated using this velocity model are in agreement with the observed ground motion amplitudes at the recording stations of the Maule earthquake, which have an average Vs_{30} of 434 m/s. Accordingly, we expect that the ground motions simulated using this model represent sites with Vs_{30} of 434 m/s.

Table 5. Crustal structure model for Cascadia.

Vp (km/s)	Qp	Vs (km/s)	Qs	Density (Kgr/m^3)	Thickness (km)
2.600	2000	1.500	900.0	2.000	0.20
5.300	2000	3.030	900.0	2.100	6.70
6.000	2000	3.370	900.0	2.500	4.60
6.500	2000	3.650	900.0	2.780	18.10
7.300	2000	4.100	900.0	3.180	15.80
8.100	2000	4.500	900.0	3.400	16.00
8.101	2000	4.501	900.0	3.401	100.00

Another important influence on the amplitude and durations on strong ground motions is the effect of sedimentary basins, such as the Puget Trough and the Portland and Tualatin basins. We have addressed basin response in these locations in other studies (Ichinose, 2003b; Pitarka et al., 2002), and recognize that this is an important issue to be addressed in future studies, but it lies beyond the scope of this report.

GROUND MOTION ATTENUATION

The attenuation of ground motion with distance derived from the strong motion simulations is shown in Figures 17-36. In Figures 17-28, the simulated ground motion values and a simple model that is

fit to those values (shown by a solid black line) are compared with the three ground motion models for various spectral periods. The simulated response spectral values for the three different hypocentral locations are shown in different colors. From this comparison, it is clear that there are large differences between the three ground motion models, especially in the slopes of the attenuation curves. For close distances (R<50 km) there is fairly good agreement between the GMPEs and the simple model derived from our simulations. This agreement improves with increasing ground motion period. For larger distances, the GMPE's underpredict the simulated ground motions, exhibiting stronger distance decay than in the present study model. In general, this behavior is consistent for all three empirical GMPE models and in agreement with the findings of Boroschek et al. (2012) that ground motions from the Maule earthquake are underpredicted by the Atkinson and Boore (2003) GMPE, as well as by the Zhao et al. (2006) GMPE at larger distances.

The second set of Figures (29-36) compares the response spectra of the simulations of the **M** 9.0 Cascadia earthquakes with the three ground motion models in a suite of distance ranges for two sites conditions (Vs$_{30}$ 434 m/s and Vs$_{30}$ 181 m/s), respectively. In most of the cases the Atkinson and Boore (2003) model underpredicts the simulated response spectra, especially in closer distances. This is again in agreement with the comparisons presented in the previous figures. The Zhao et al. (2006) and Abrahamson et al. (2012) models are in closer agreement with the simulations, particularly for distances < 200km. The scaled simulated response spectra to lower Vs30 values (181 m/s) capture the general characteristics of the empirical models.

From both sets of figures it can be seen that the differences among the various slip models used are very small, exhibiting practically identical ground motions for the whole period and distance ranges studied.
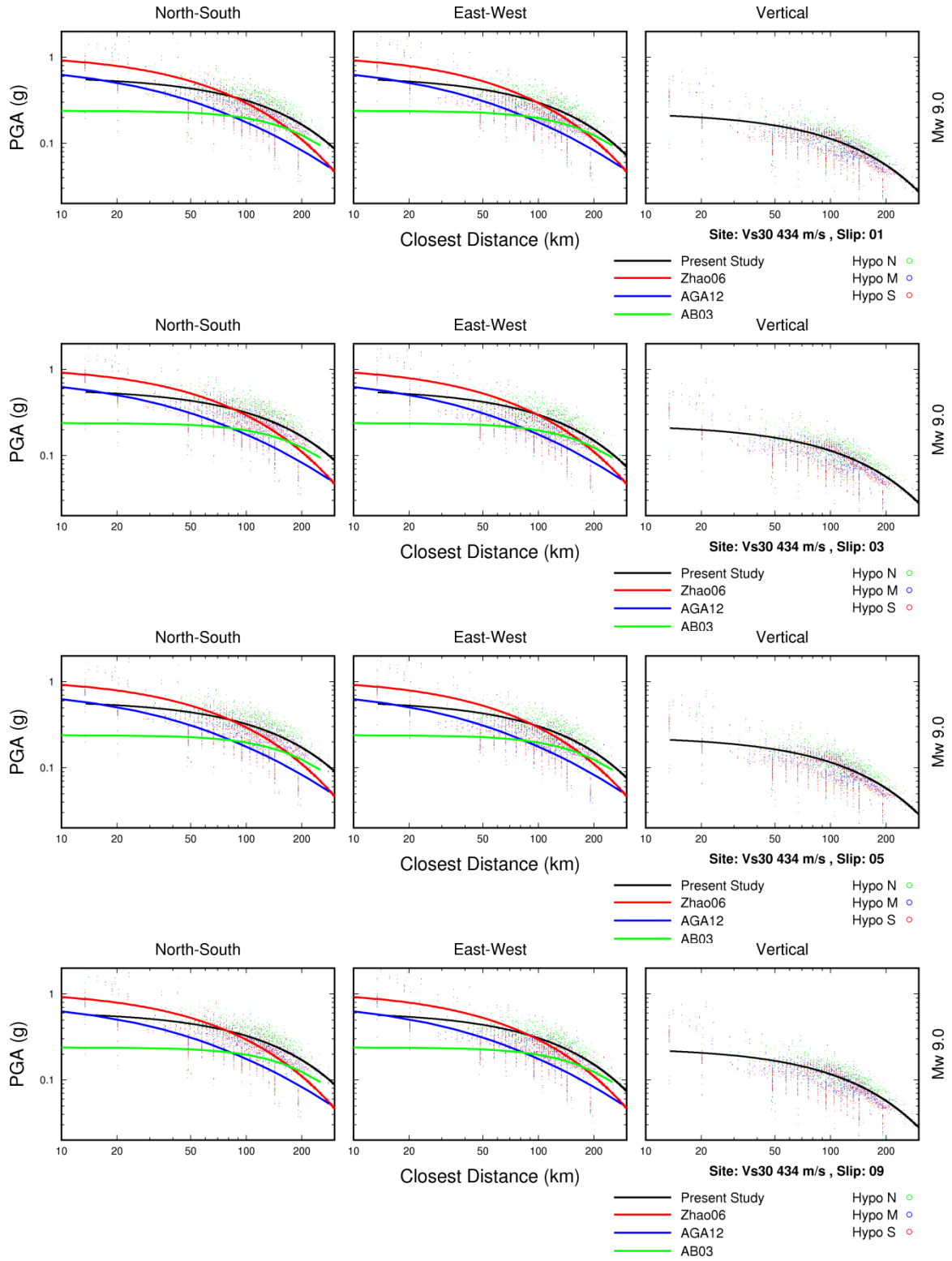
Figure 17. Comparison of simulated peak accelerations (points and black line), for various slip models for M 9.0 Cascadia earthquake with ground motion models for Vs_{30} 434 m/s.
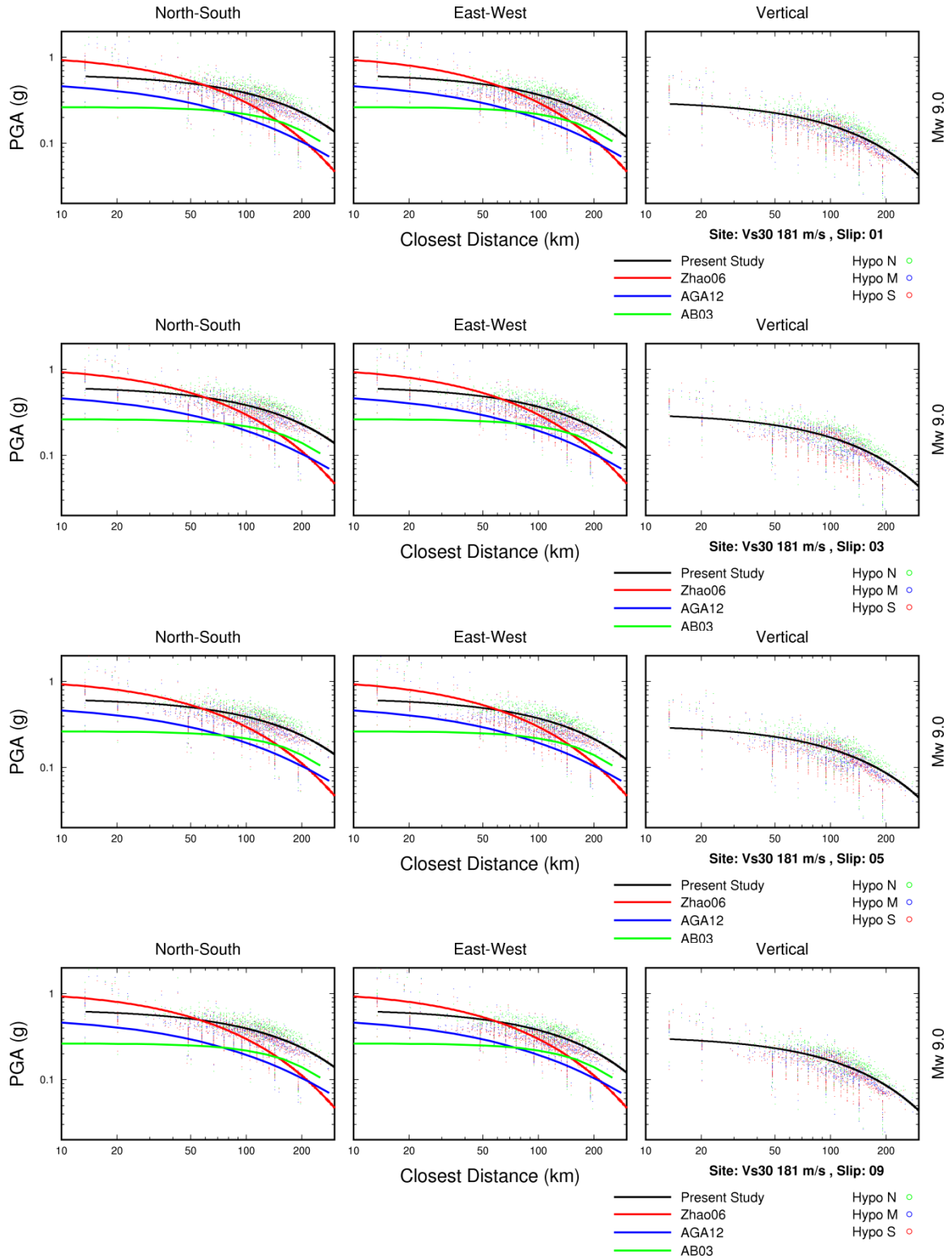
Figure 18. Comparison of simulated peak accelerations (points and black line), for various slip models for M 9.0 Cascadia earthquake with ground motion models for Vs$_{30}$ 181 m/s.
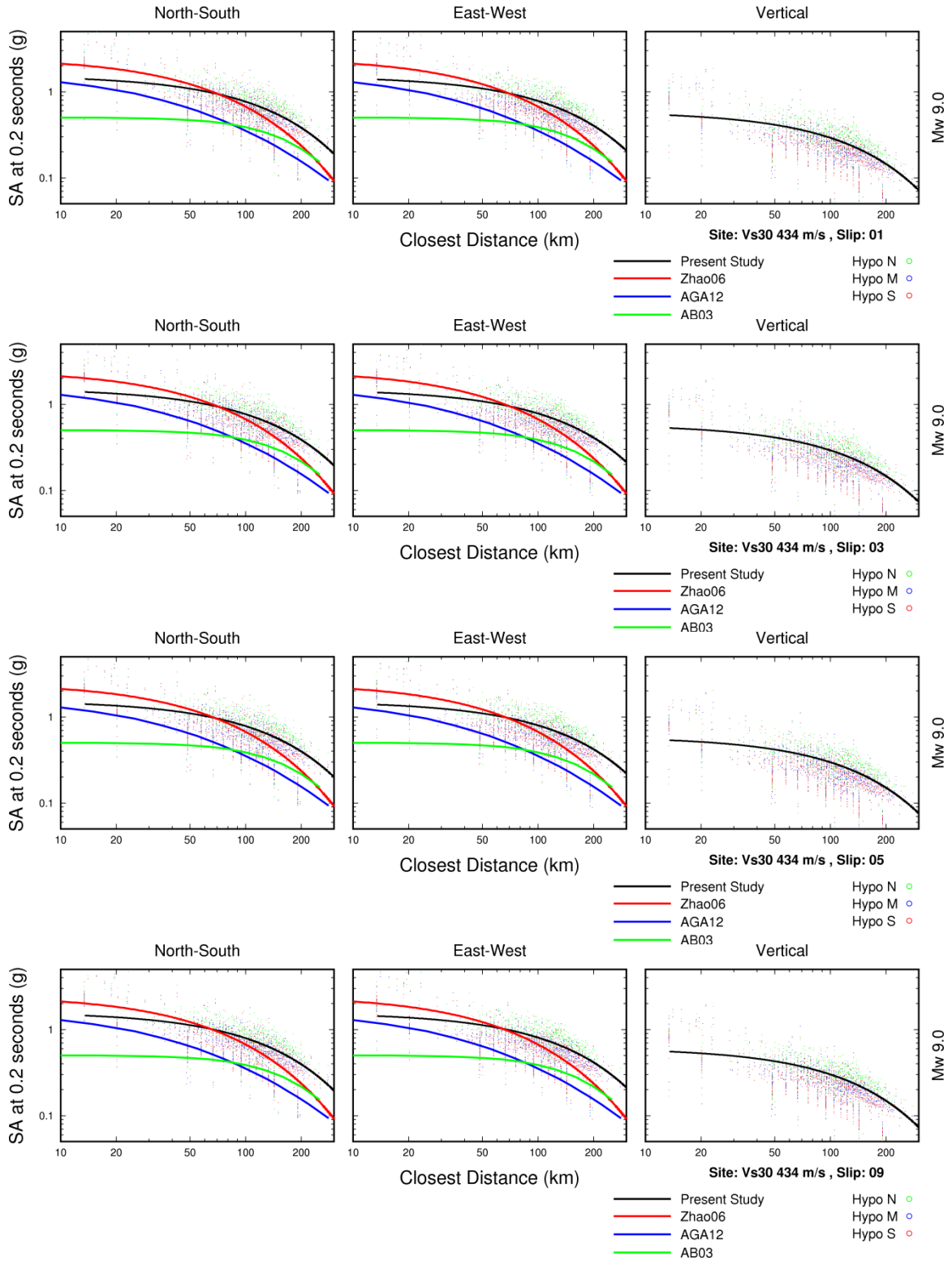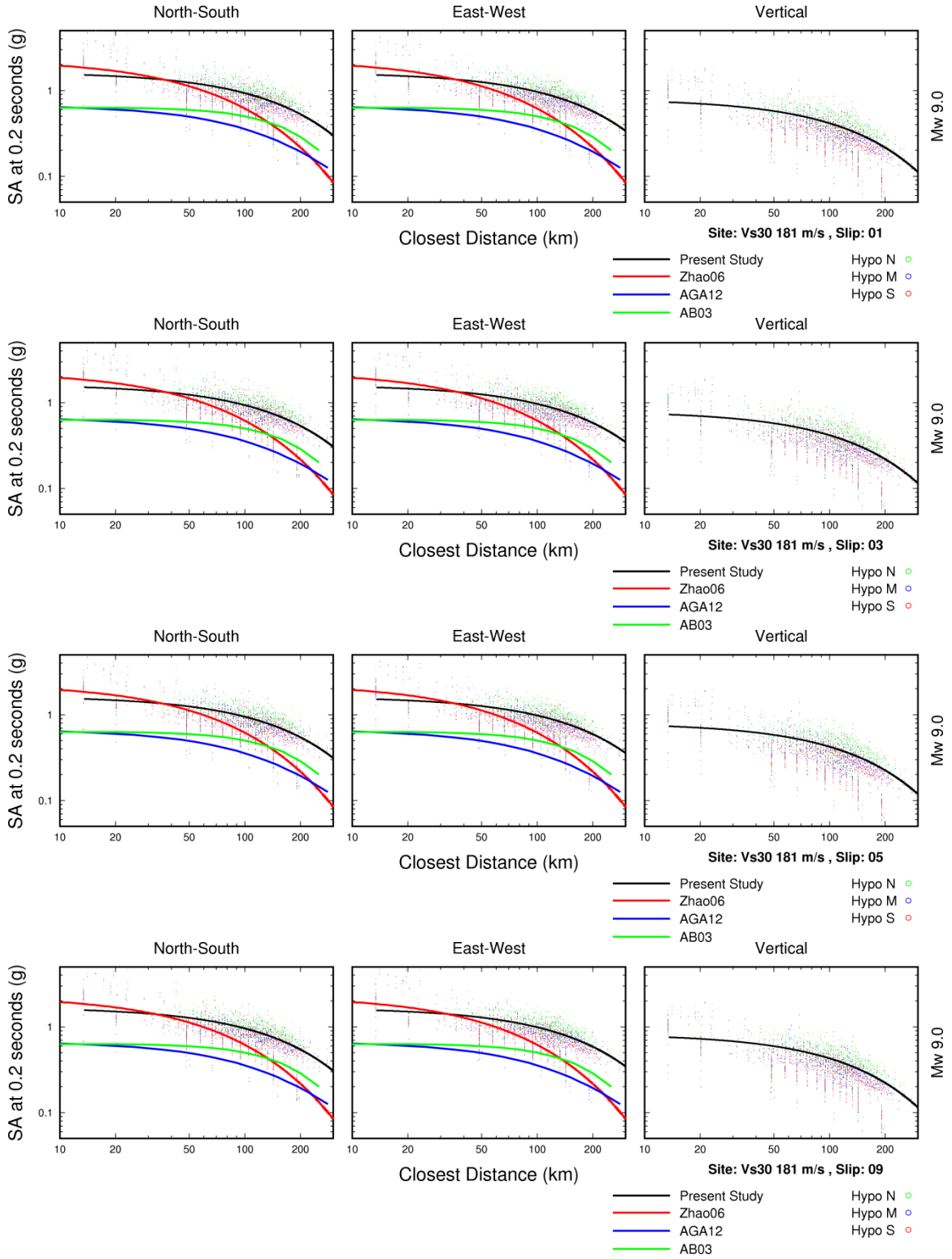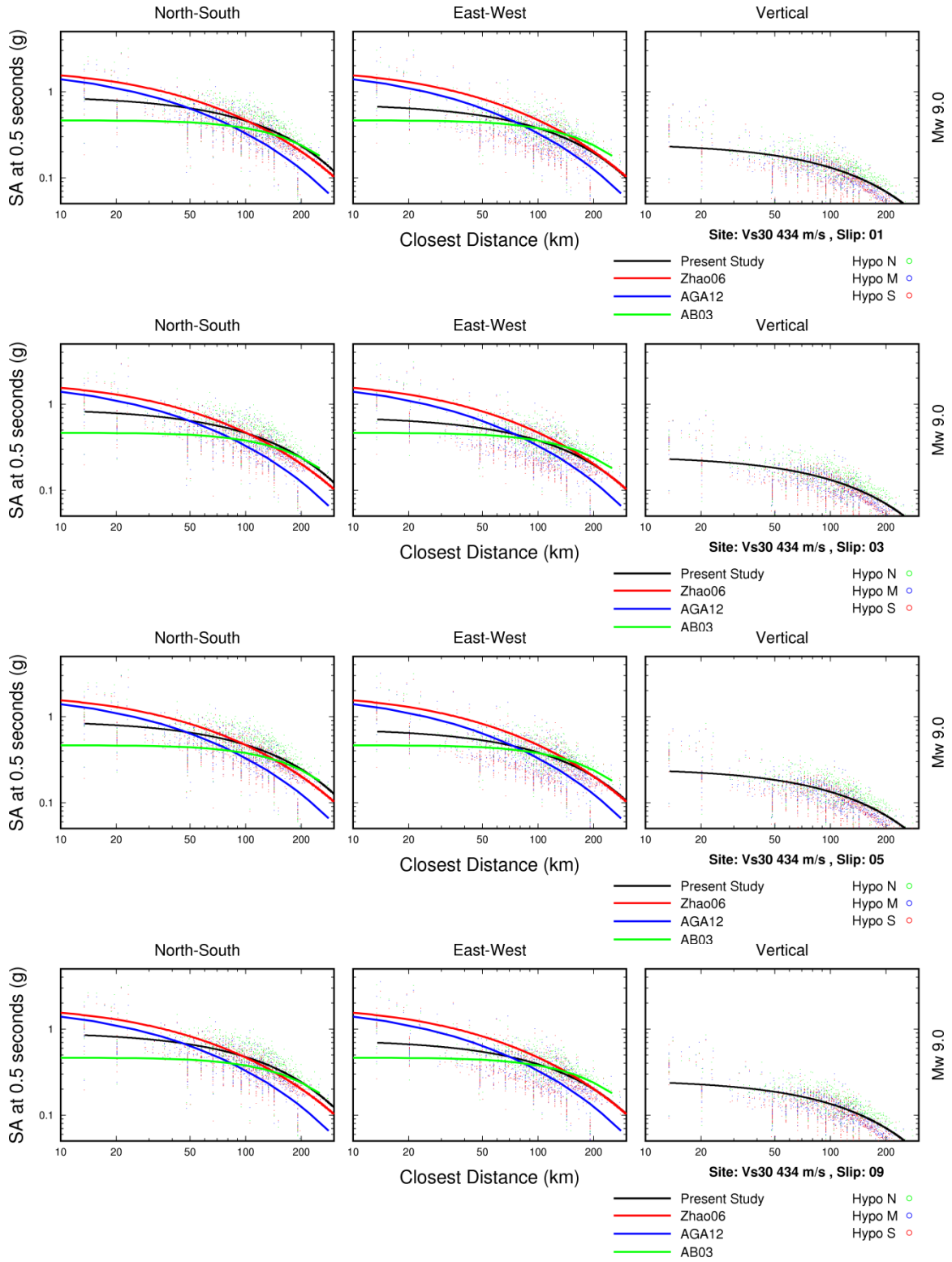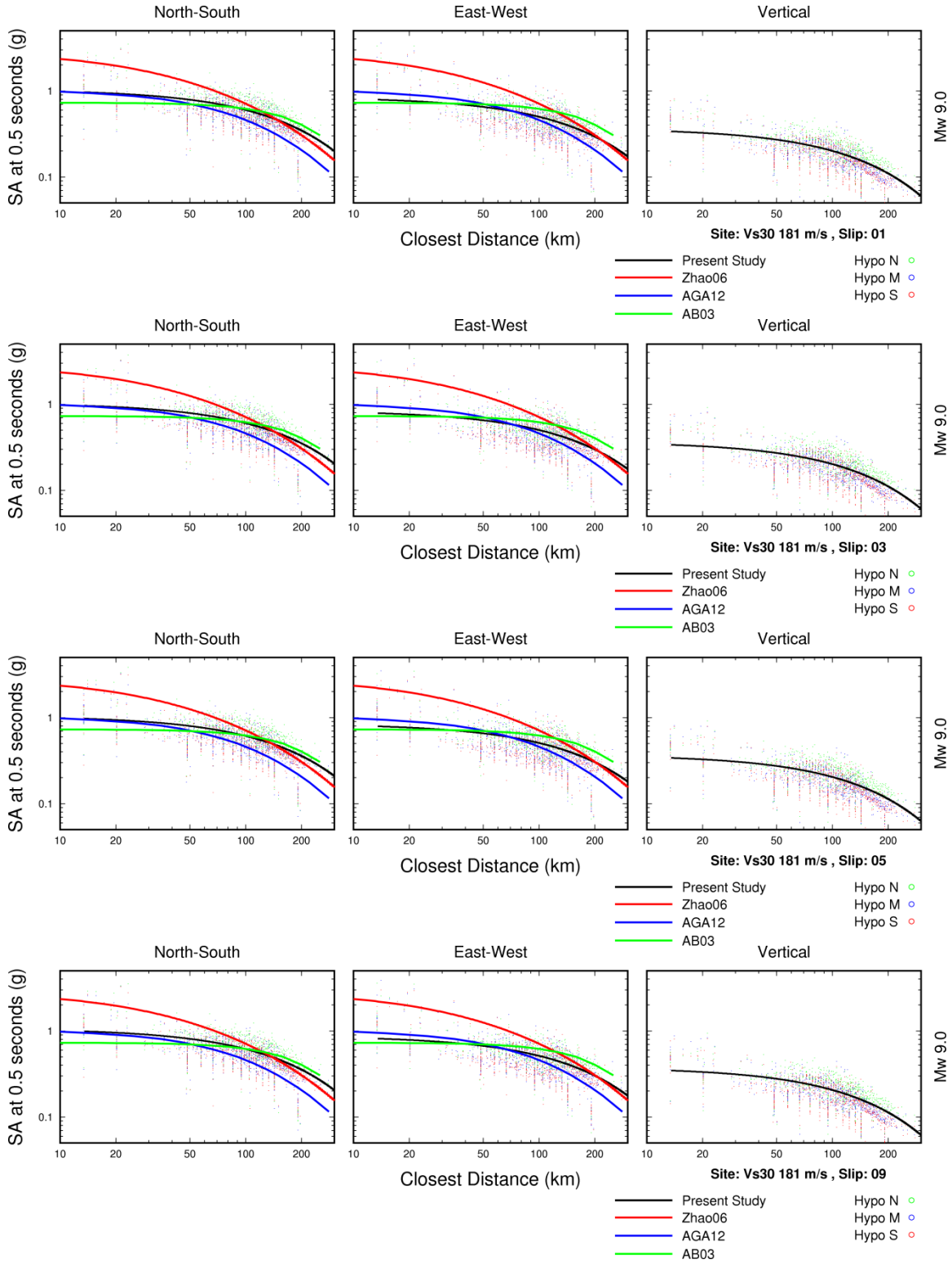
Figure 19. Comparison of simulated 0.2 sec spectral accelerations (points and black line), for various slip models for M 9.0 Cascadia earthquake with ground motion models for Vs$_{30}$ 434 m/s.

Figure 20. Comparison of simulated 0.2 sec spectral accelerations (points and black line), for various slip models for M 9.0 Cascadia earthquake with ground motion models for Vs$_{30}$ 181 m/s.

Figure 21. Comparison of simulated 0.5 sec spectral accelerations (points and black line), for various slip models for M 9.0 Cascadia earthquake with ground motion models for Vs$_{30}$ 434 m/s.

Figure 22. Comparison of simulated 0.5 sec spectral accelerations (points and black line), for various slip models for M 9.0 Cascadia earthquake with ground motion models for Vs$_{30}$ 181 m/s.
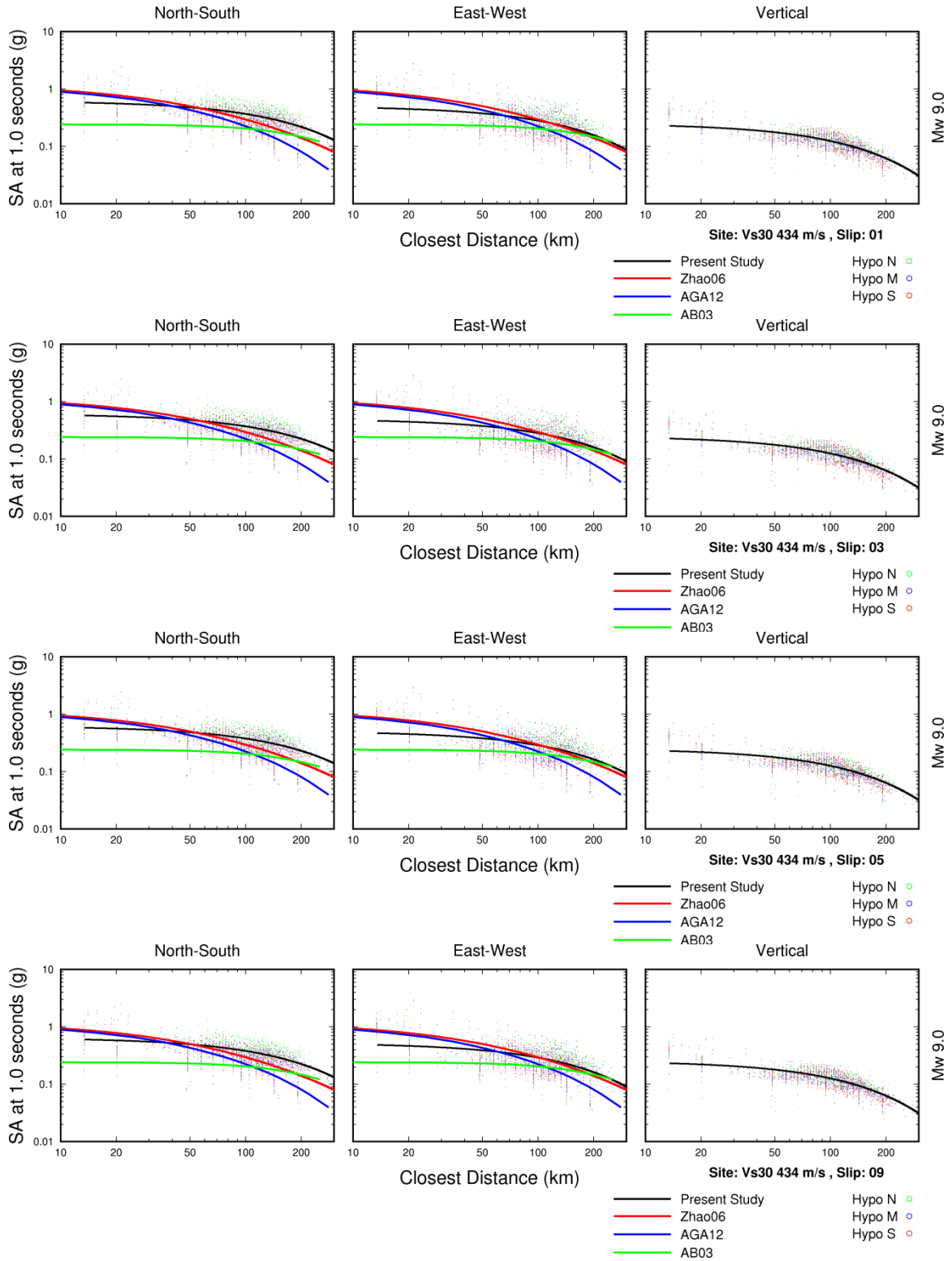
Figure 23. Comparison of simulated 1 sec spectral accelerations (points and black line), for various slip models for M 9.0 Cascadia earthquake with ground motion models for Vs$_{30}$ 434 m/s.
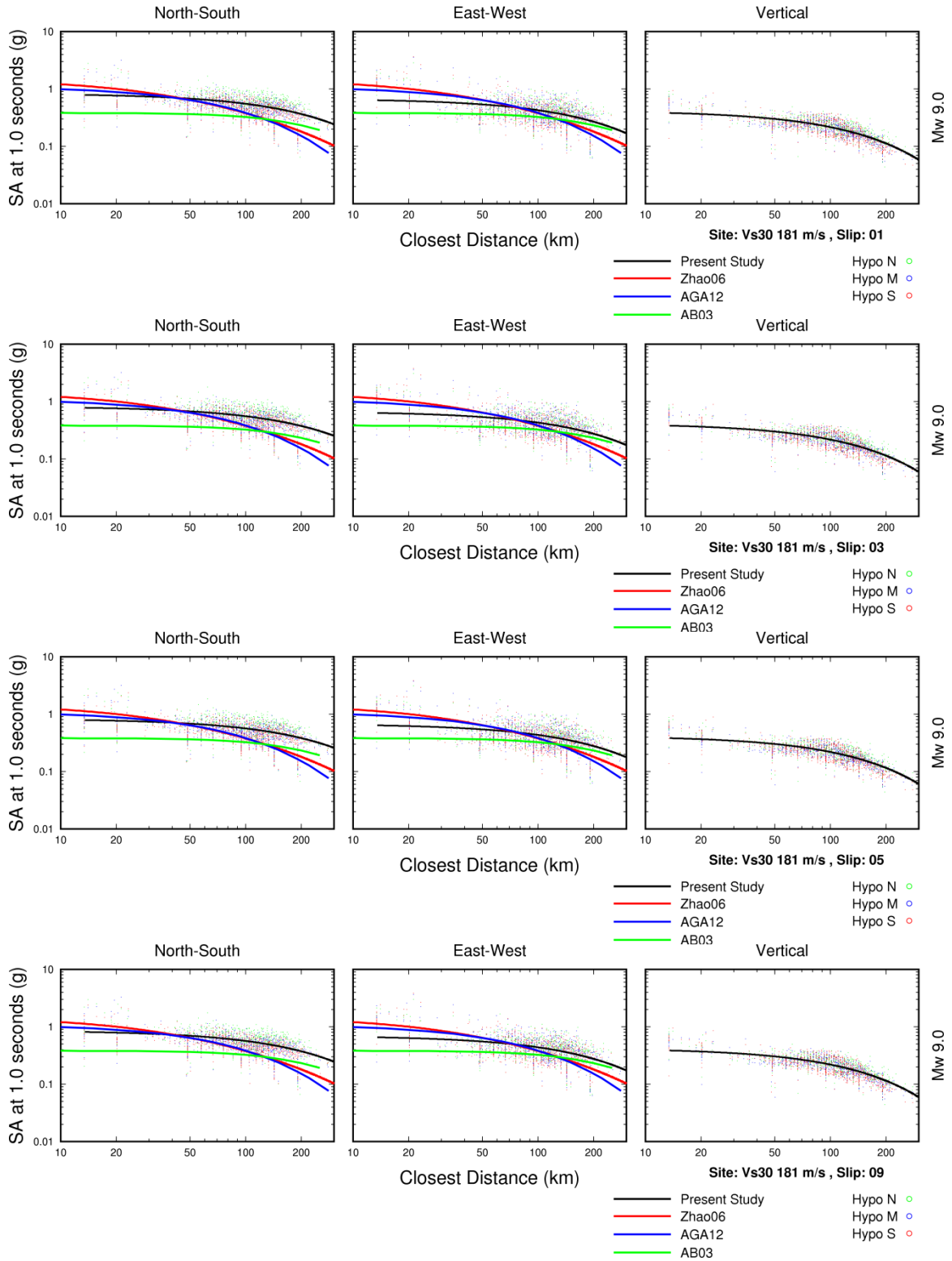
Figure 24. Comparison of simulated 1 sec spectral accelerations (points and black line), for various slip models for M 9.0 Cascadia earthquake with ground motion models for Vs$_{30}$ 181 m/s.
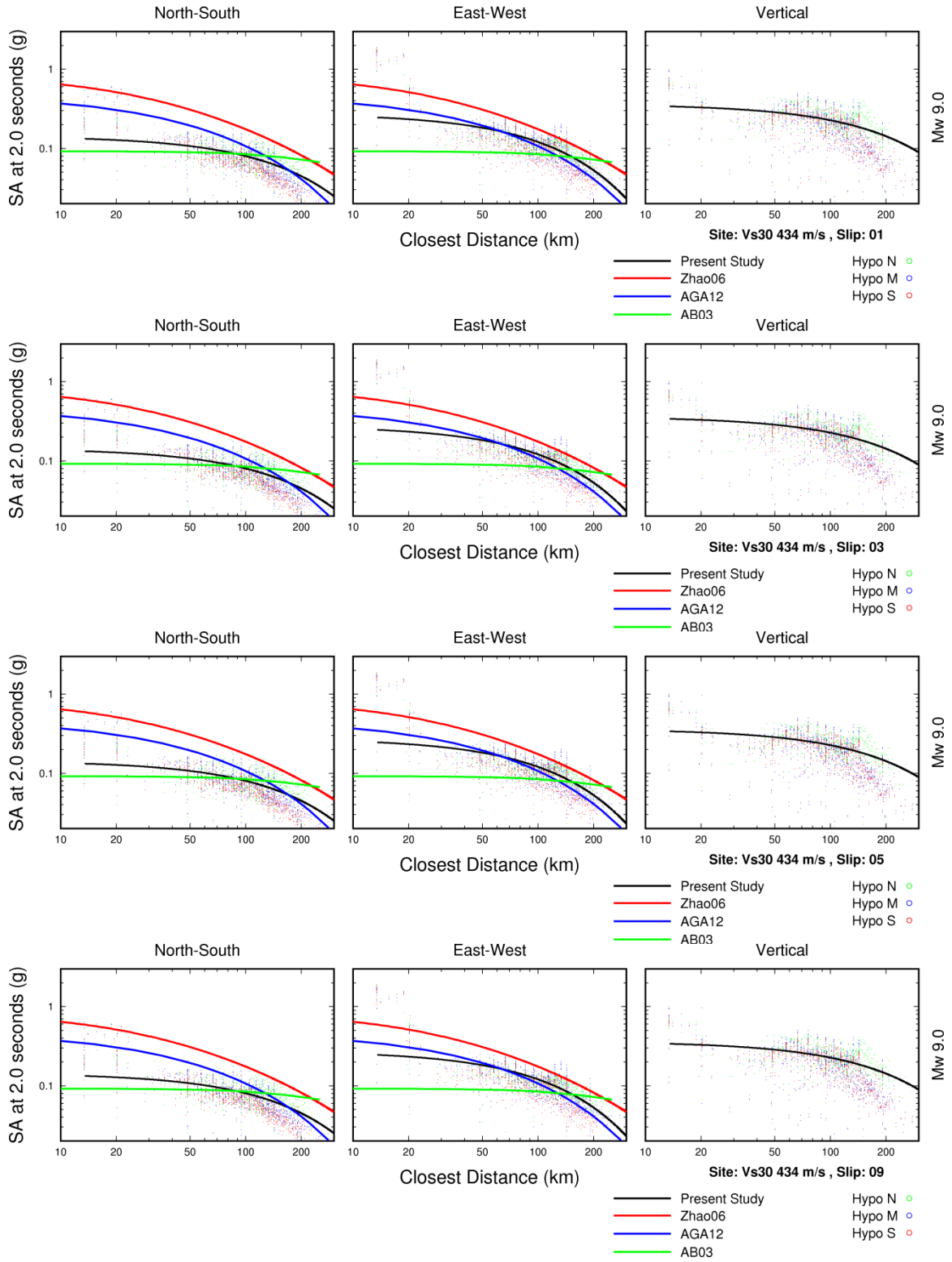
Figure 25. Comparison of simulated 2 sec spectral accelerations (points and black line), for various slip models for M 9.0 Cascadia earthquake with ground motion models for Vs$_{30}$ 434 m/s.
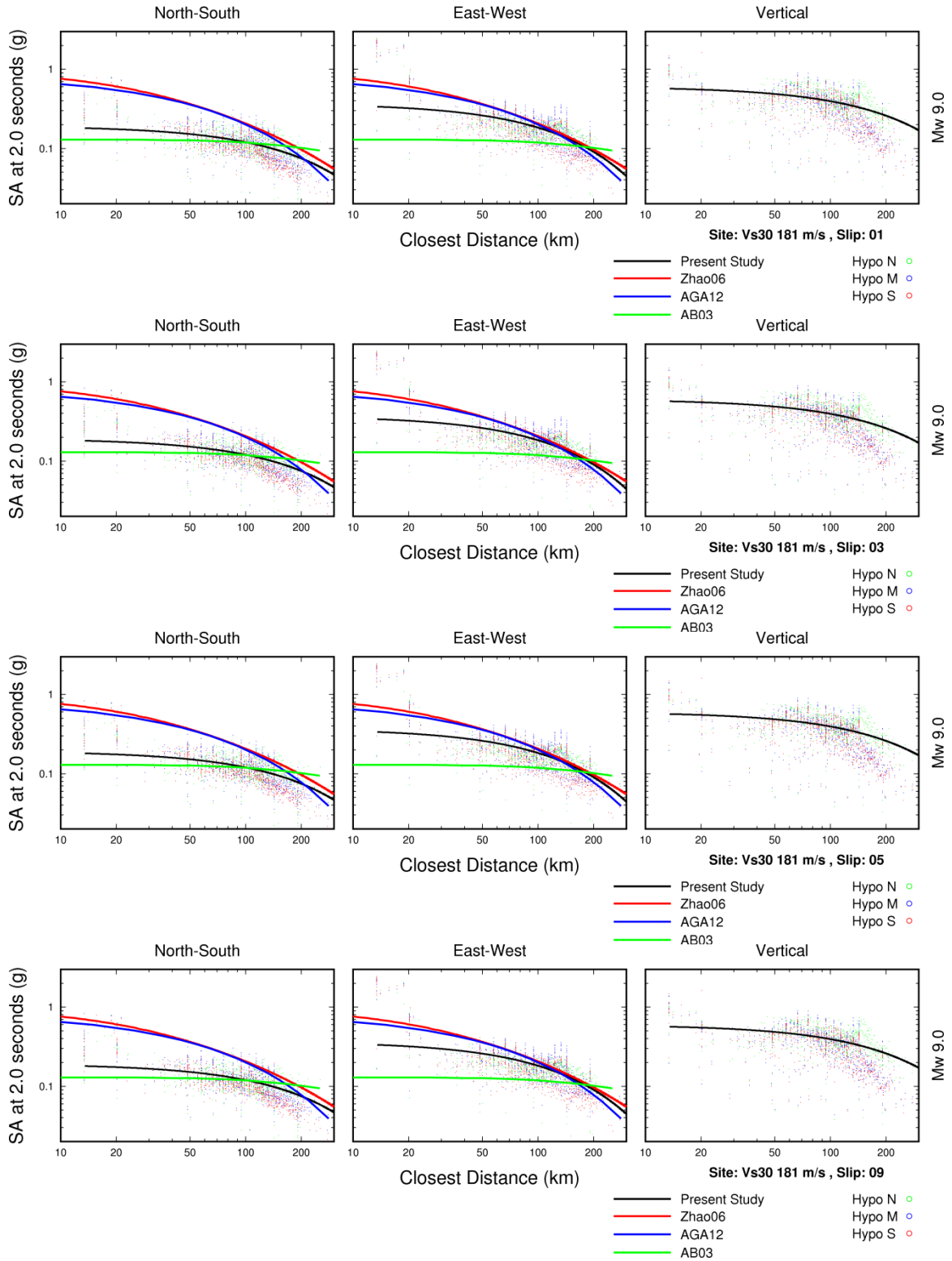
Figure 26. Comparison of simulated 2 sec spectral accelerations (points and black line), for various slip models for M 9.0 Cascadia earthquake with ground motion models for Vs$_{30}$ 181 m/s.

Figure 27. Comparison of simulated 5 sec spectral accelerations (points and black line), for various slip models for M 9.0 Cascadia earthquake with ground motion models for Vs$_{30}$ 434 m/s.
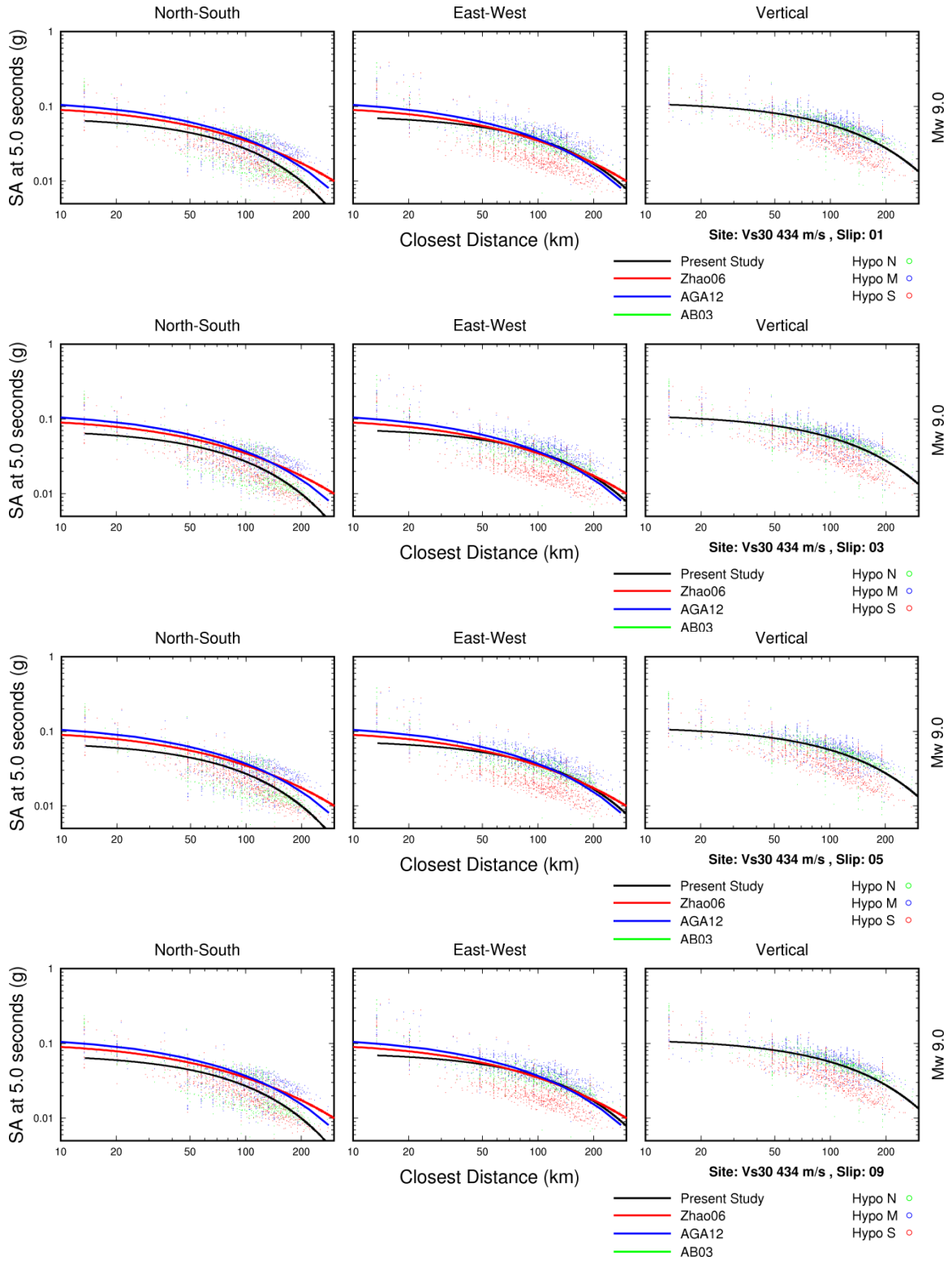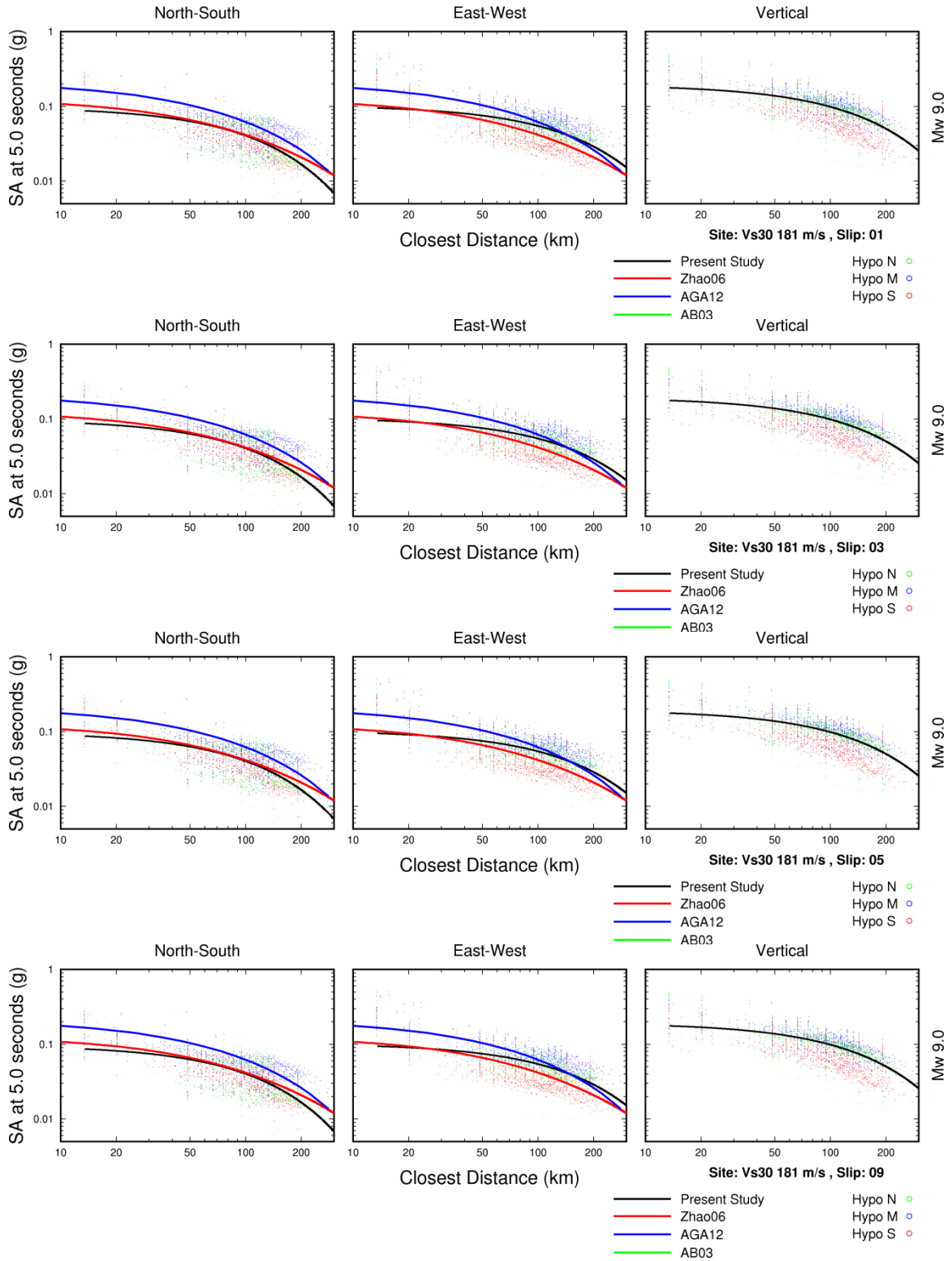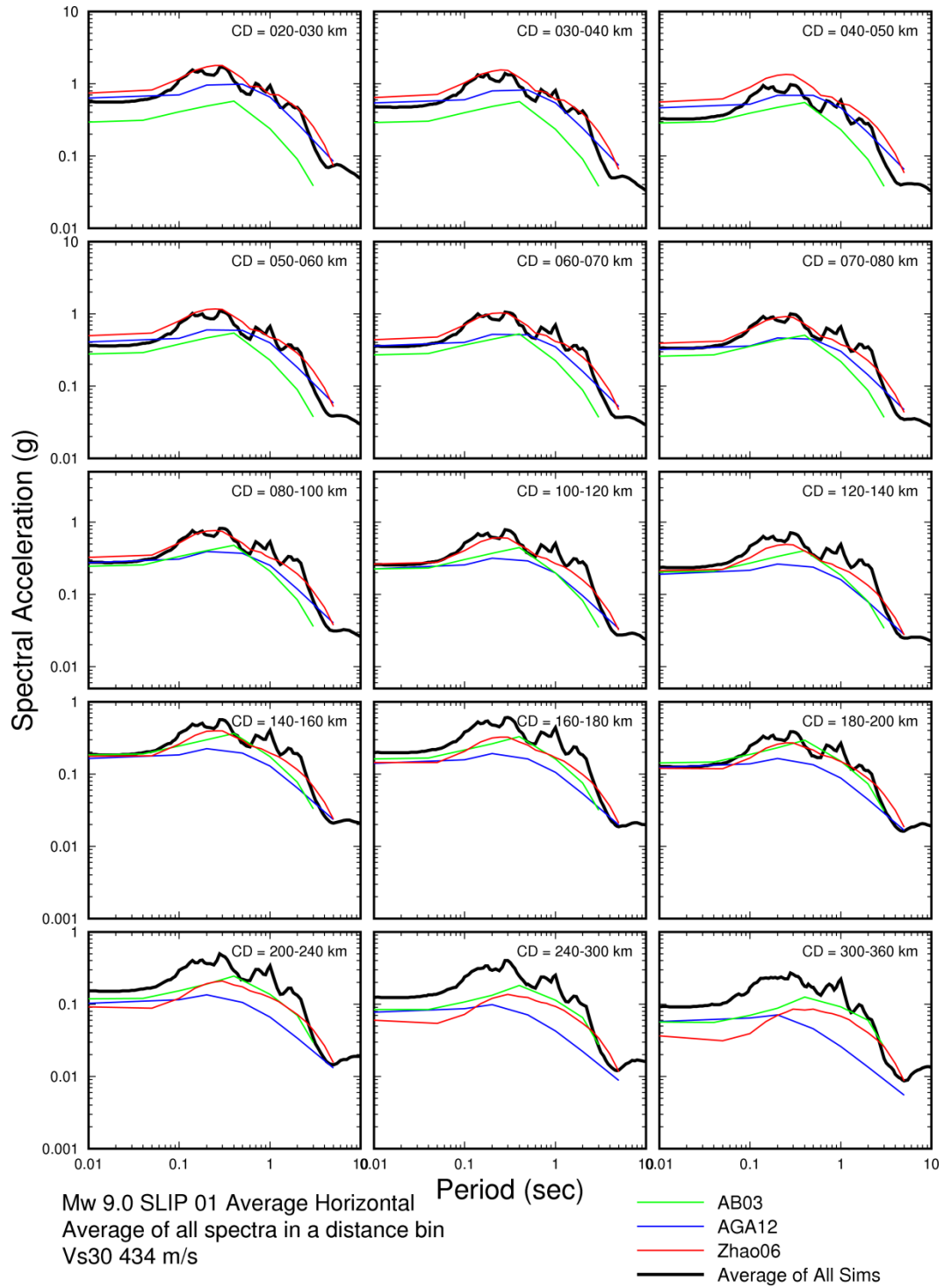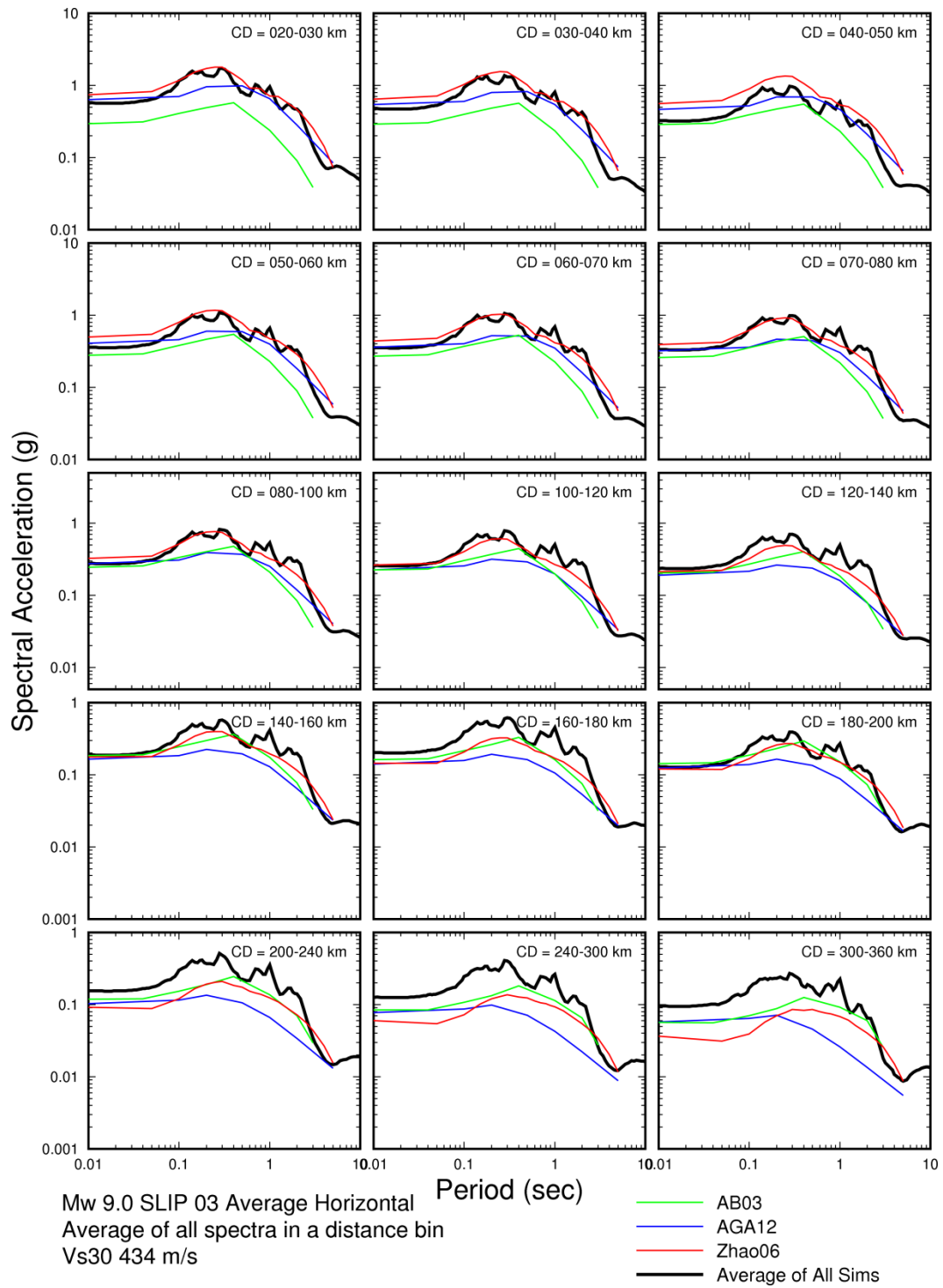
Figure 28. Comparison of simulated 5 sec spectral accelerations (points and black line), for various slip models for M 9.0 Cascadia earthquake with ground motion models for Vs$_{30}$ 181 m/s.
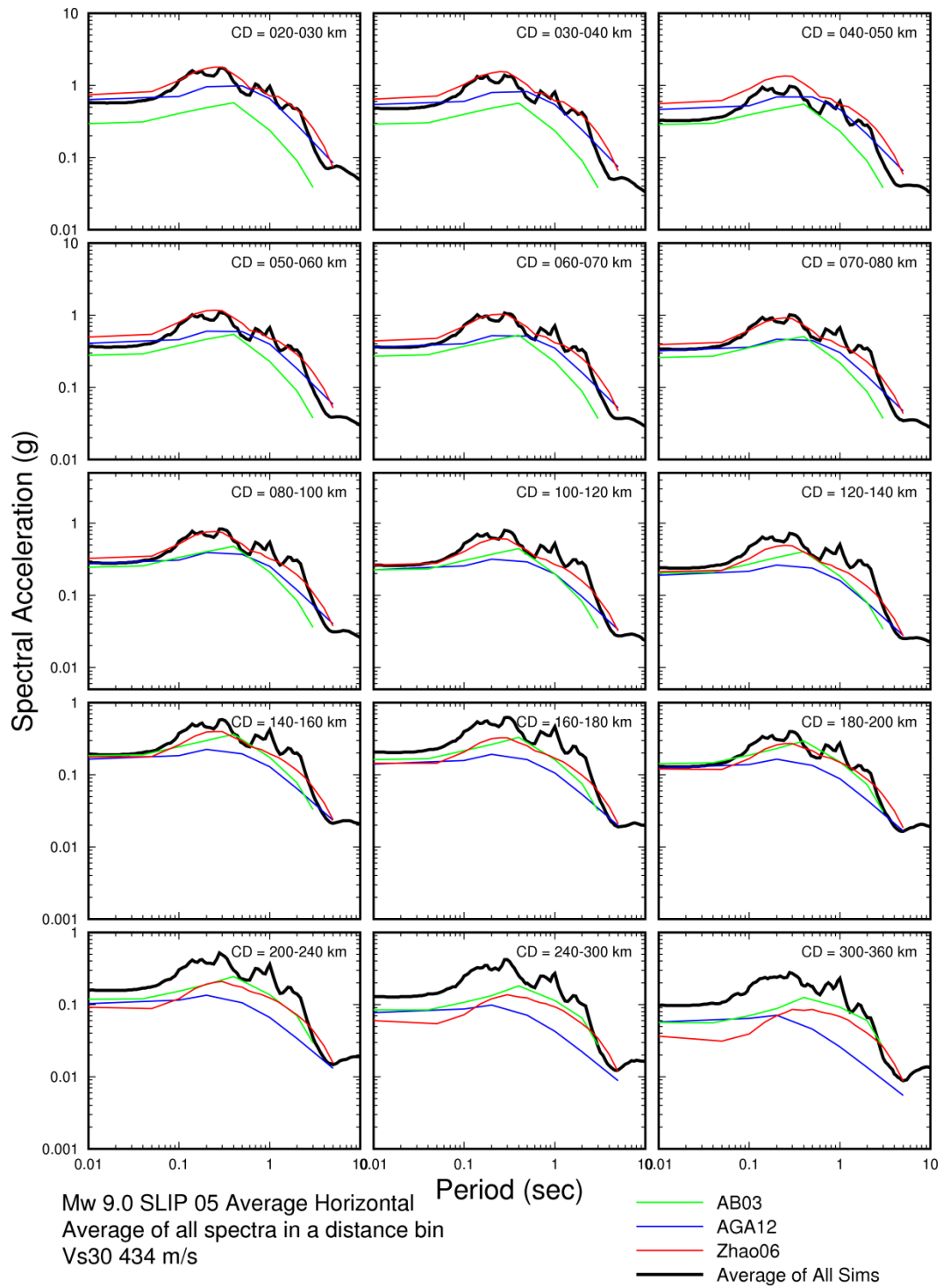
Figure 29. Comparison of simulated response spectra for a suite of distance ranges for M 9.0 Cascadia earthquake for Vs$_{30}$ 434 m/s with three ground motion models, and a ground motion model representing the simulations, for slip model 1.

Figure 30. Comparison of simulated response spectra for a suite of distance ranges for M 9.0 Cascadia earthquake for Vs$_{30}$ 434 m/s with three ground motion models, and a ground motion model representing the simulations, for slip model 3.

Figure 31. Comparison of simulated response spectra for a suite of distance ranges for M 9.0 Cascadia earthquake for Vs$_{30}$ 434 m/s with three ground motion models, and a ground motion model representing the simulations, for slip model 5.

Figure 32. Comparison of simulated response spectra for a suite of distance ranges for M 9.0 Cascadia earthquake for Vs$_{30}$ 434 m/s with three ground motion models, and a ground motion model representing the simulations, for slip model 9.

Figure 33. Comparison of simulated response spectra for a suite of distance ranges for M 9.0 Cascadia earthquake for Vs$_{30}$ 181 m/s with three ground motion models, and a ground motion model representing the simulations, for slip model 1.
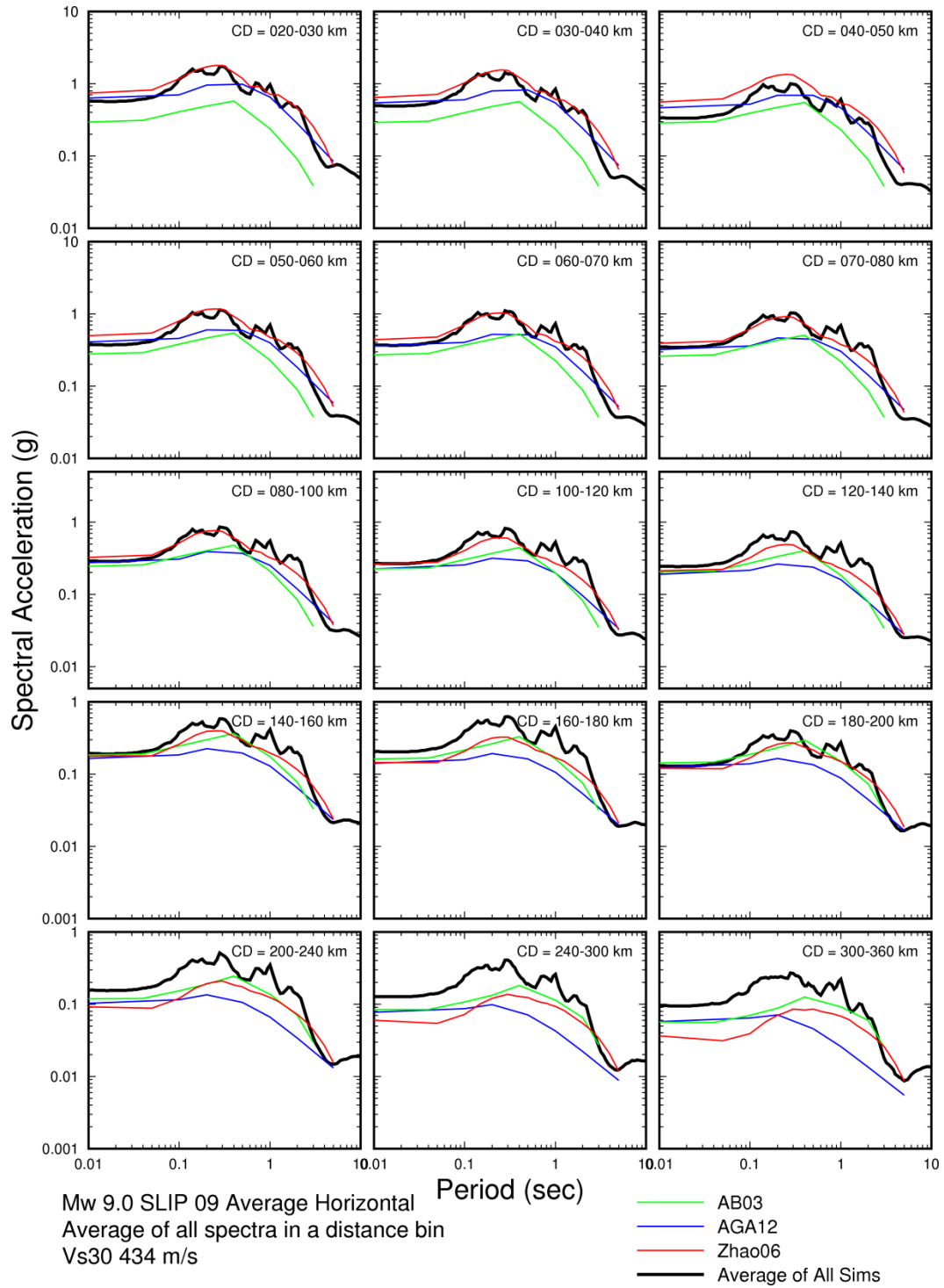
Figure 34. Comparison of simulated response spectra for a suite of distance ranges for M 9.0 Cascadia earthquake for Vs$_{30}$ 181 m/s with three ground motion models, and a ground motion model representing the simulations, for slip model 3.
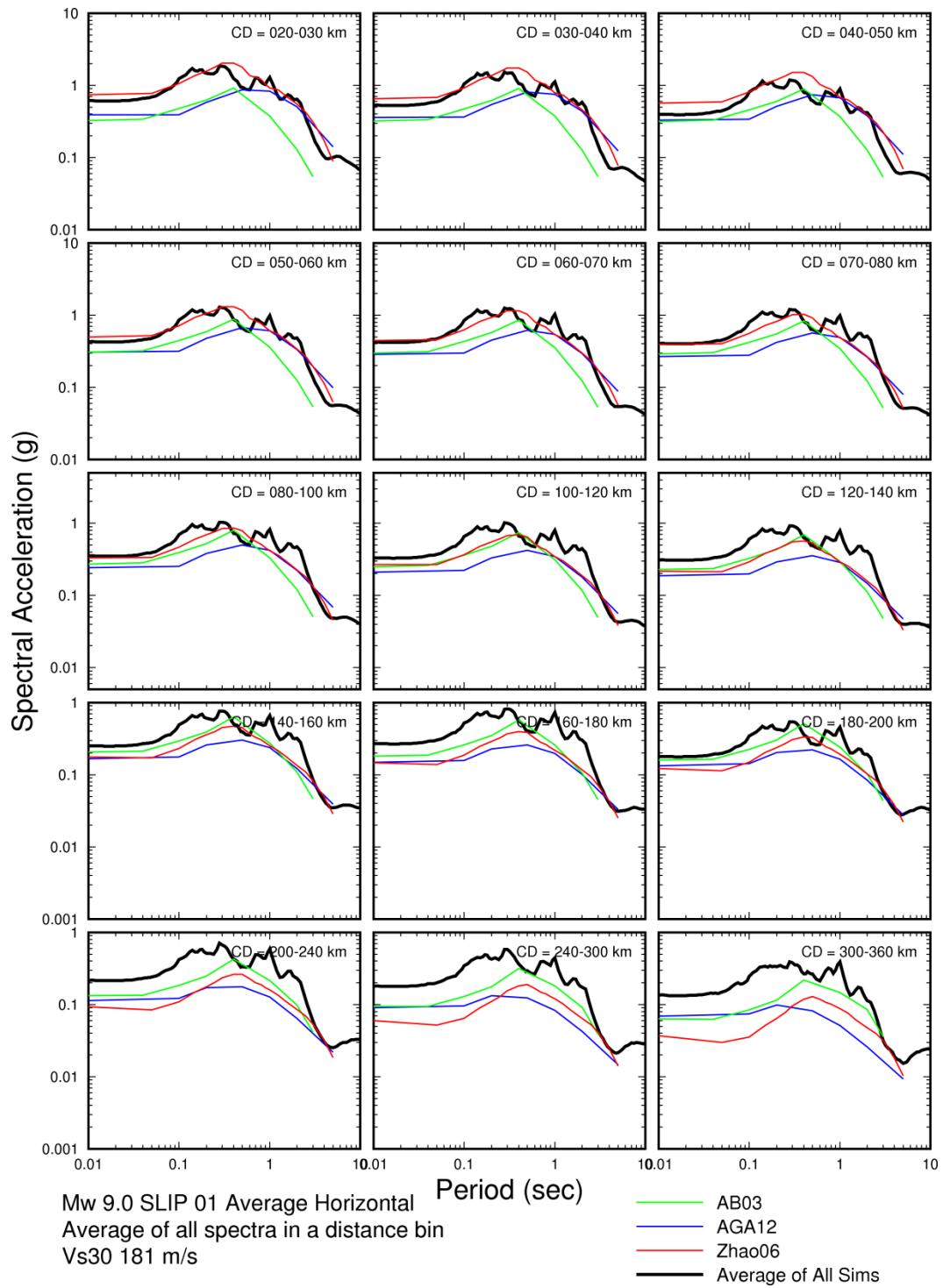
Figure 35. Comparison of simulated response spectra for a suite of distance ranges for M 9.0 Cascadia earthquake for Vs$_{30}$ 181 m/s with three ground motion models, and a ground motion model representing the simulations, for slip model 5.
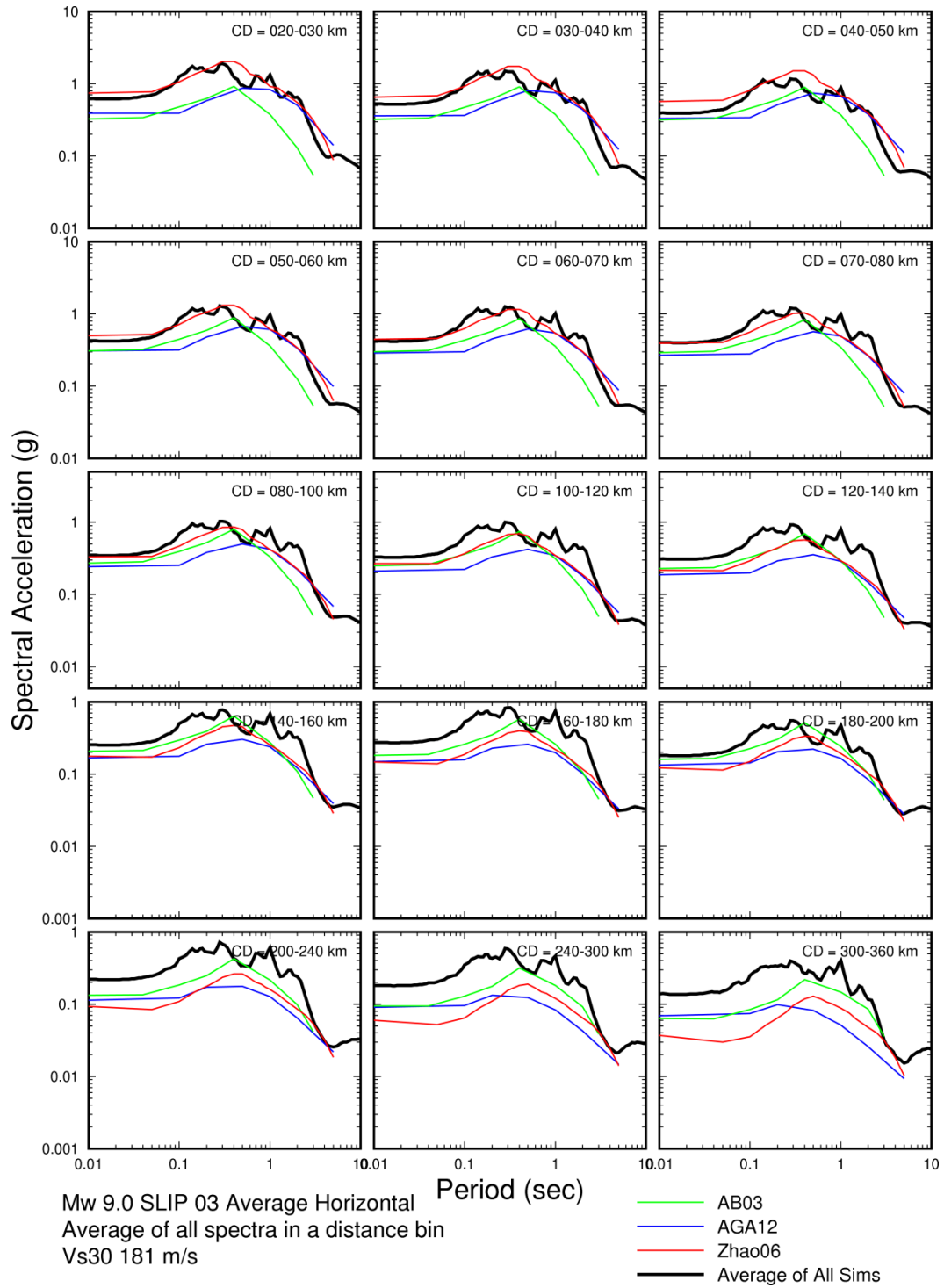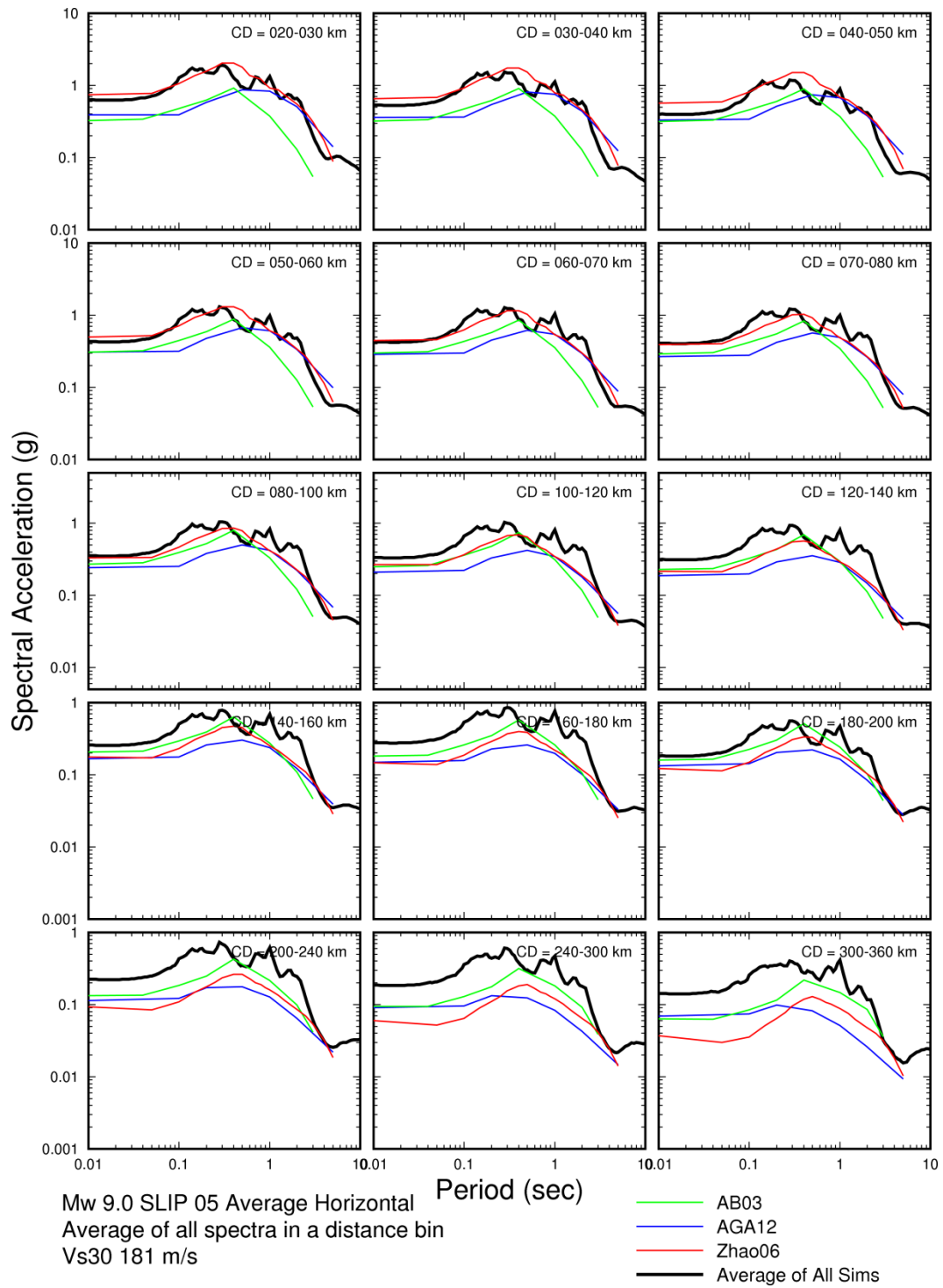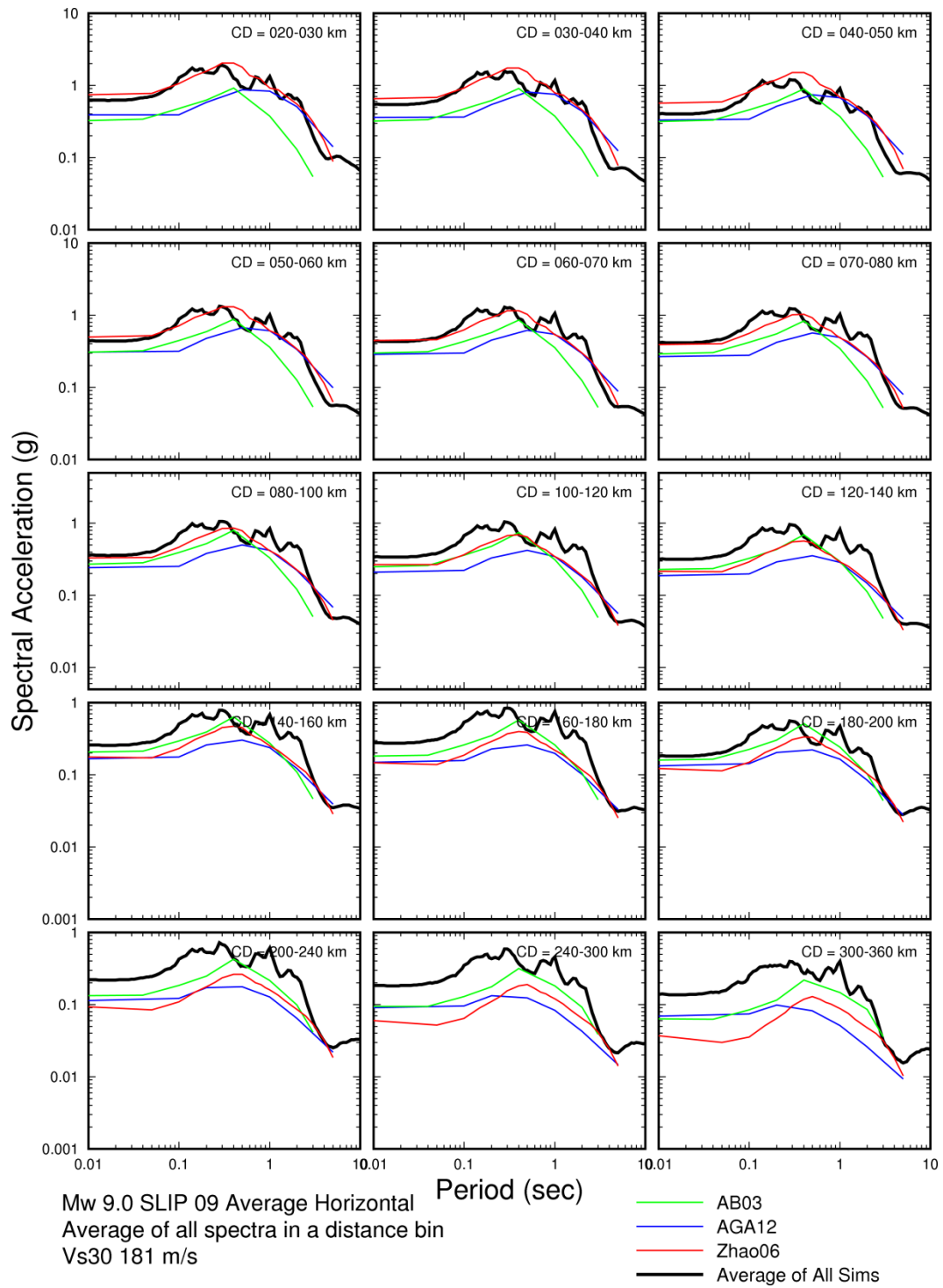
Figure 36. Comparison of simulated response spectra for a suite of distance ranges for M 9.0 Cascadia earthquake for Vs$_{30}$ 181 m/s with three ground motion models, and a ground motion model representing the simulations, for slip model 9.

We averaged the simulations over the three hypocenter locations and the two horizontal components for the different slip models, to obtain simple ground motion models for **M** 9.0 earthquakes. Since the differences among the results from different slip models are negligible we will use the ground motion model derived from slip model 03. The ground motion models coefficients are given in Tables 6 and 7. We consider that these ground motion models are appropriate for estimating the response spectra of ground motions of earthquakes that rupture the entire Cascadia Plate Interface.

Table 6. Ground motion model for M 9.0 earthquakes rupturing the entire Cascadia Plate Interface, Vs30 434 m/s.

Period (s)	C_1	C_2
0.01	-0.6357	-0.00724
0.10	0.1223	-0.00740
0.20	0.2851	-0.00714
0.50	-0.3148	-0.00710
1.00	-0.6713	-0.00581
2.00	-1.4977	-0.00891
5.00	-2.6710	-0.00828
10.00	-3.1831	-0.00460
20.00	-4.2606	-0.00389

The simulations are fit to the simple ground motion model: $Ln(Sa) = C_1 + C_2 * R_{cld}$

Table 7. Ground motion model for Mw 9.0 earthquakes rupturing the entire Cascadia Plate Interface, Vs30 181 m/s.

Period	C1	C2
0.01	-0.5251	-0.0059
0.10	0.2329	-0.0061
0.20	0.3957	-0.0058
0.50	-0.1282	-0.0058
1.00	-0.3402	-0.0046
2.00	-1.1665	-0.0077
5.00	-2.3399	-0.0071
10.00	-2.8519	-0.0034
20.00	-3.9294	-0.0027

The simulations are fit to the simple ground motion model: $Ln(Sa) = C_1 + C_2 * R_{cld}$
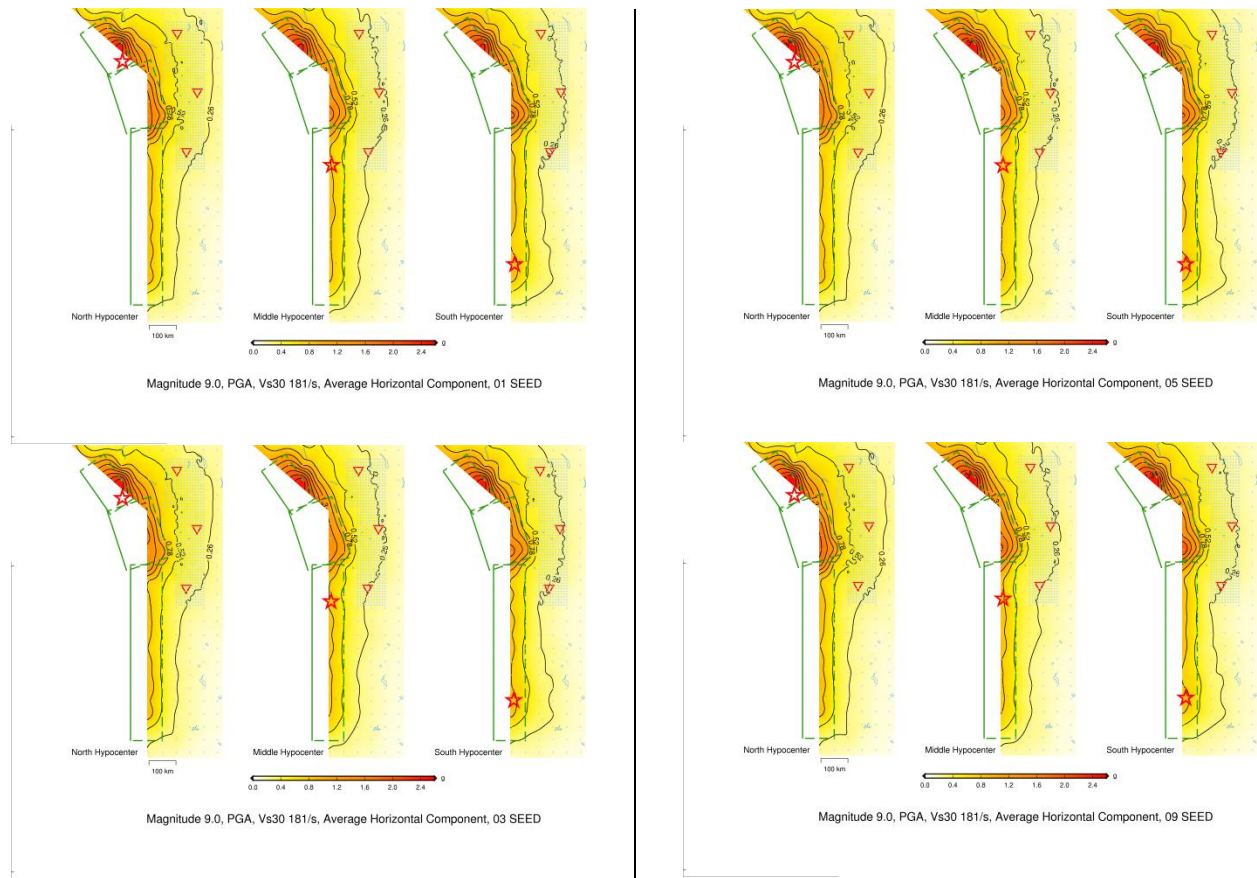
GROUND MOTION MAPS

We performed ground motion simulations at the stations shown by the grid in Figure 13. We then generated ground motion maps for each of the three rupture scenarios. The maps, shown in Figures 35 through 44, are for peak acceleration and response spectral acceleration at 0.2, 0.5, 1.0, 2.0, and 5.0 seconds for four different slip models and for two site conditions; Vs30 of 434 m/s and of 181 m/s, respectively.

High values for the periods of 0.2s and 0.5s are exhibited in throughout the Olympic Peninsula, independent of the hypocentral location of the scenario earthquake. However, for the longer periods of ground motion (T>1s) the maximum values of ground motion occur in a well defined coastal zone which extends from Washington to the northern parts of California.
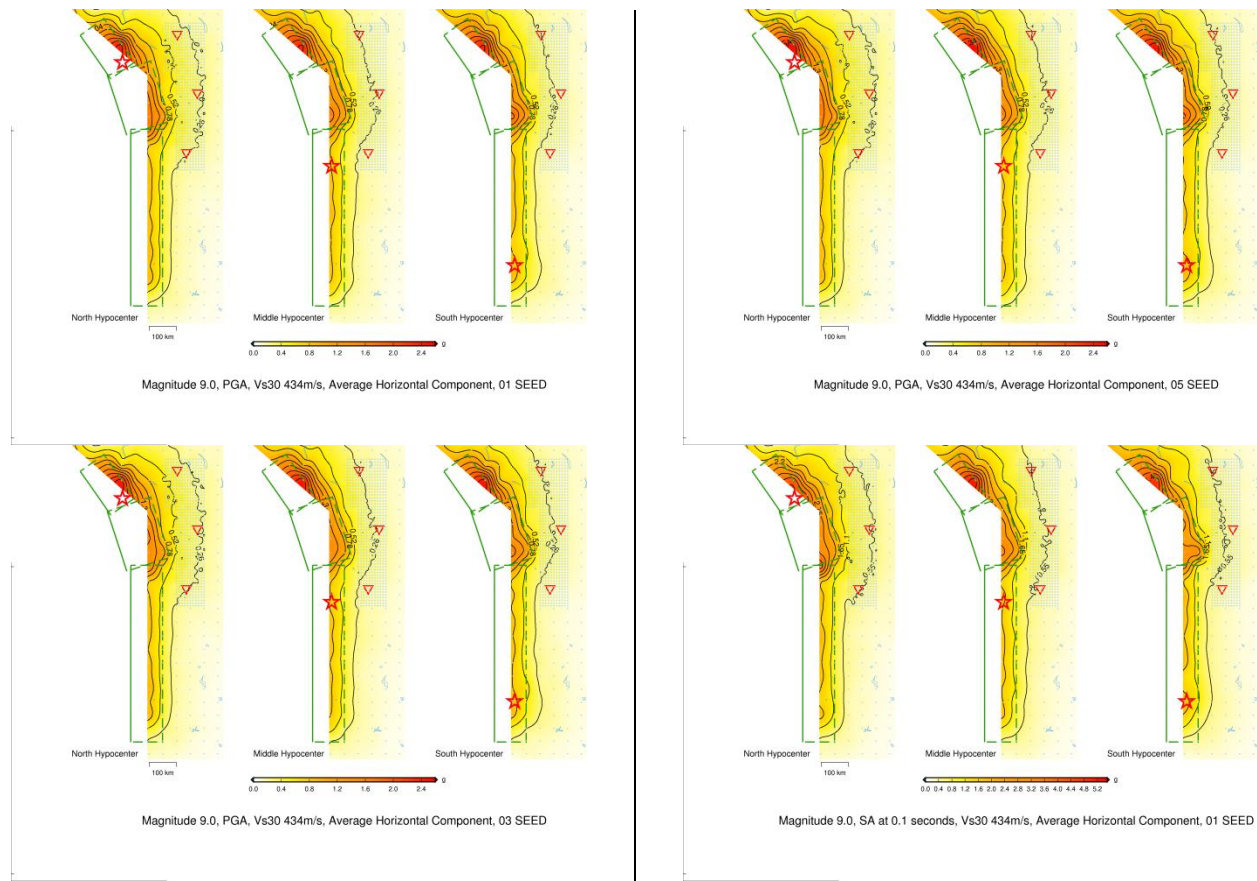
Figure 37. Ground motion maps for peak acceleration for an M 9.0 Cascadia earthquake for three hypocenter locations and various slip models, for Vs$_{30}$ 434 m/s.

Figure 38. Ground motion maps for peak acceleration for an M 9.0 Cascadia earthquake for three hypocenter locations and various slip models, for Vs$_{30}$ 181 m/s.

Figure 39. Ground motion maps for 0.2 s spectral acceleration for an M 9.0 Cascadia earthquake for three hypocenter locations and various slip models, for Vs$_{30}$ 434 m/s.

Figure 40. Ground motion maps for 0.2s spectral acceleration for an M 9.0 Cascadia earthquake for three hypocenter locations and various slip models, for Vs$_{30}$ 181 m/s.

Figure 41. Ground motion maps for 0.5s spectral acceleration for an M 9.0 Cascadia earthquake for three hypocenter locations and various slip models, for Vs$_{30}$ 434 m/s.
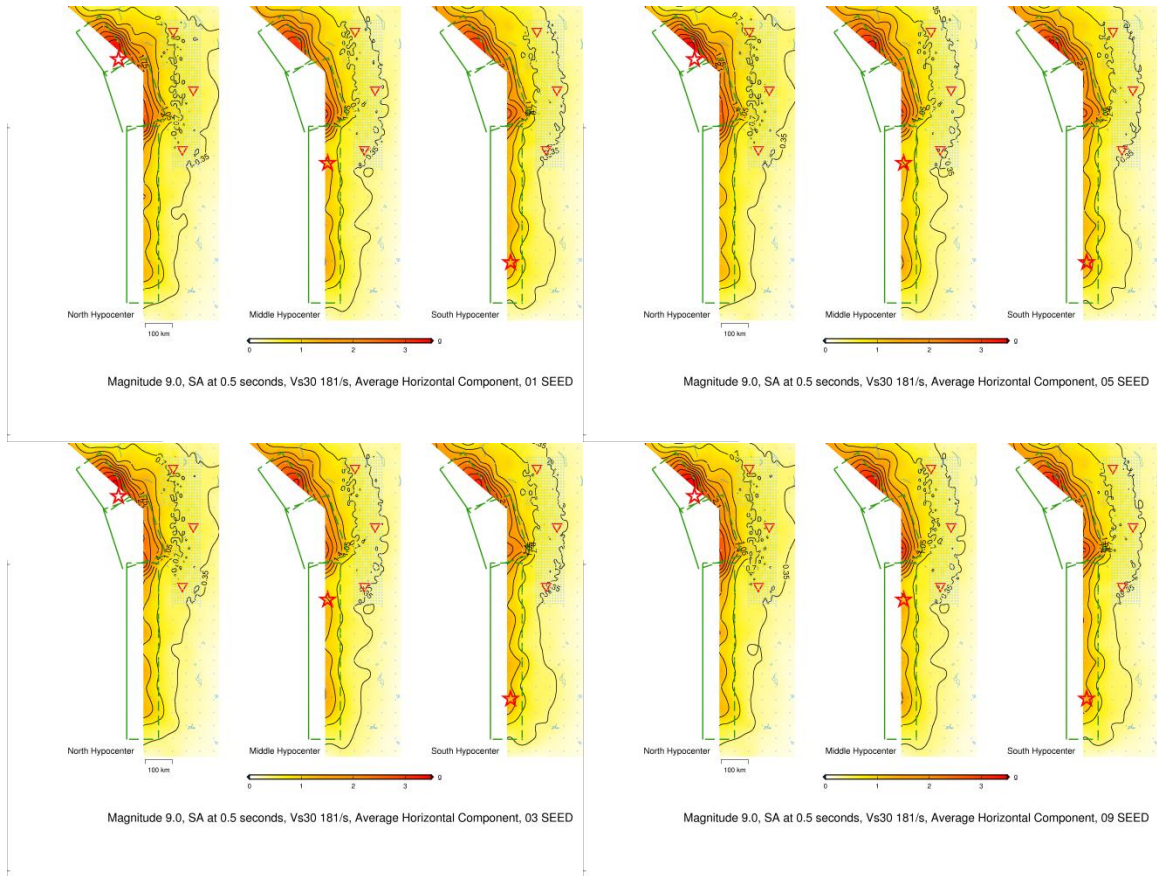
Figure 42. Ground motion maps for 0.5s spectral acceleration for an M 9.0 Cascadia earthquake for three hypocenter locations and various slip models, for Vs$_{30}$ 181 m/s.
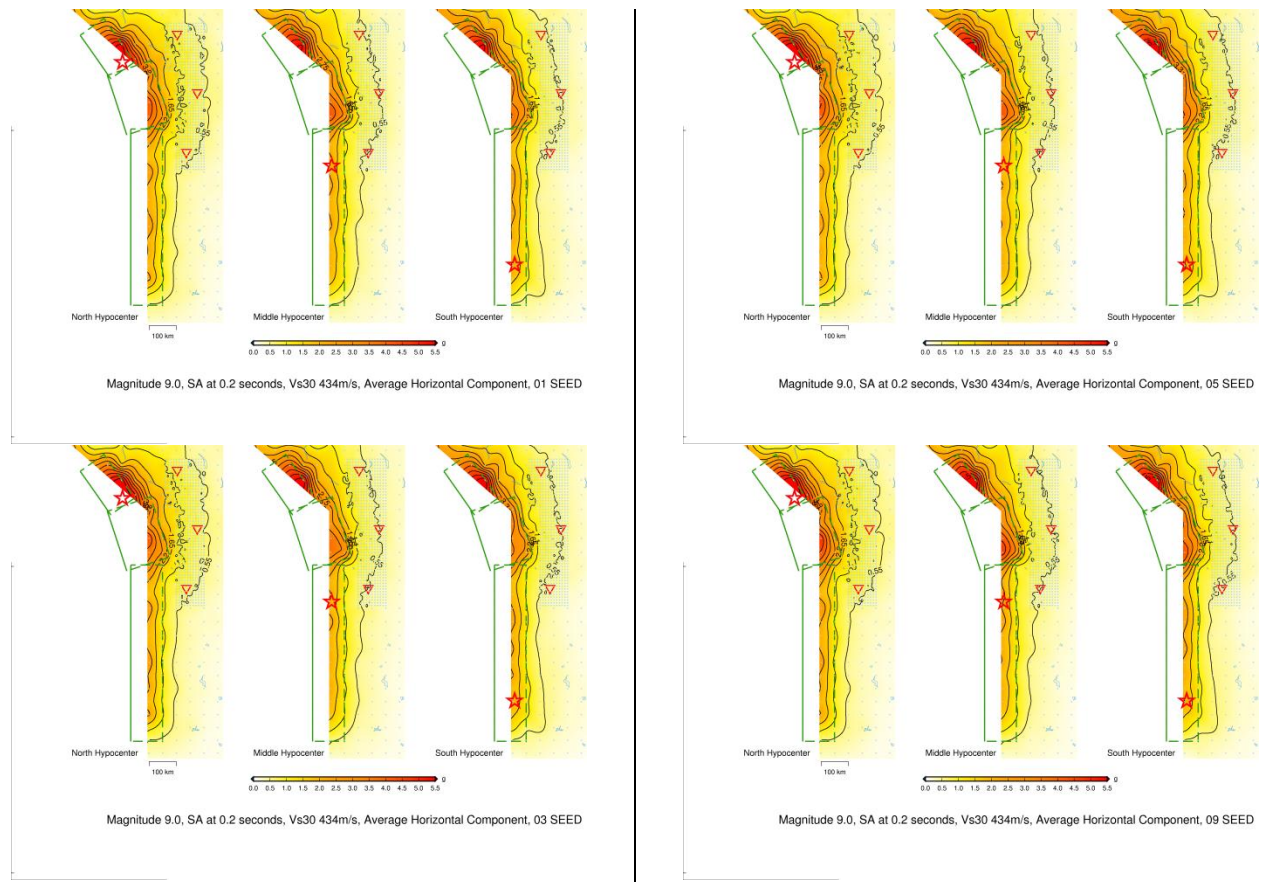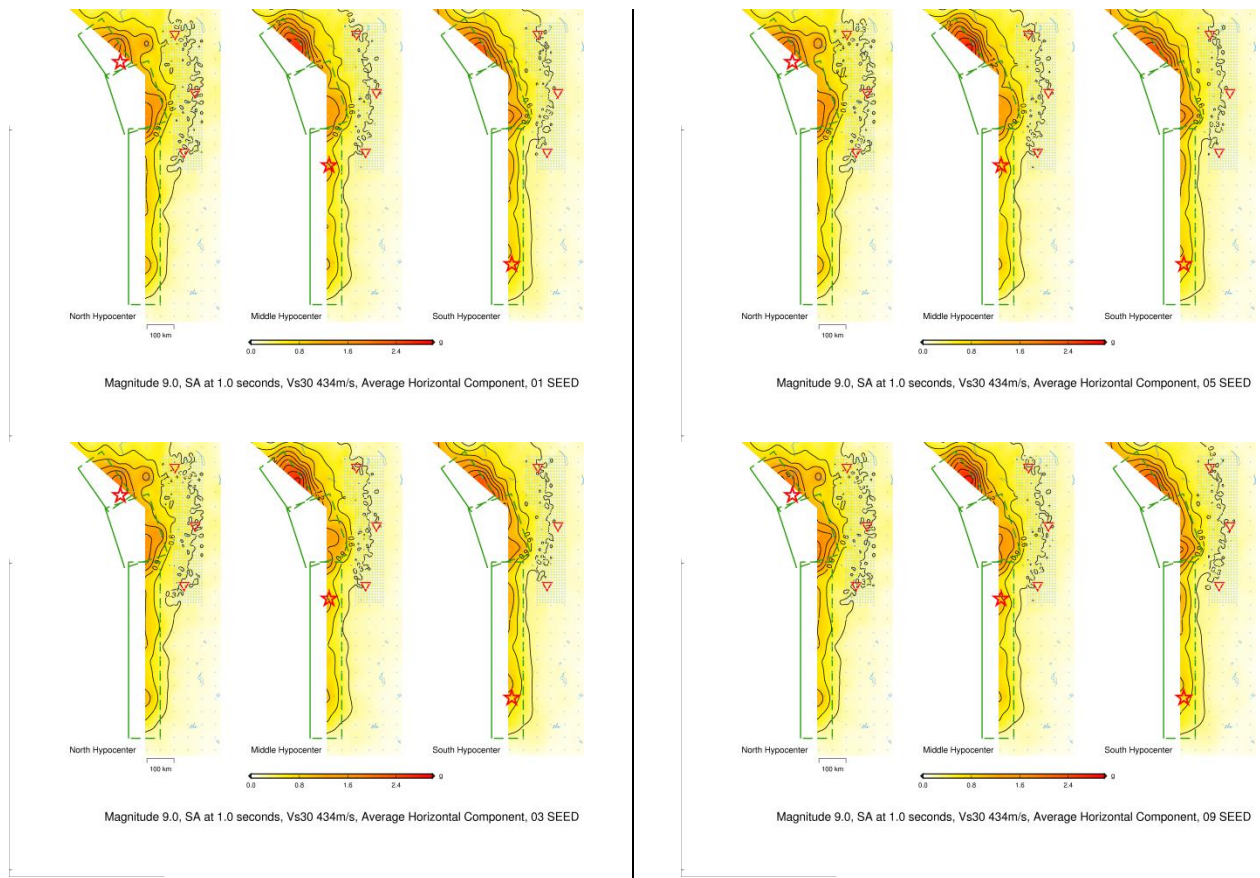
Figure 43. Ground motion maps for 1s spectral acceleration for an M 9.0 Cascadia earthquake for three hypocenter locations and various slip models, for Vs$_{30}$ 434 m/s.
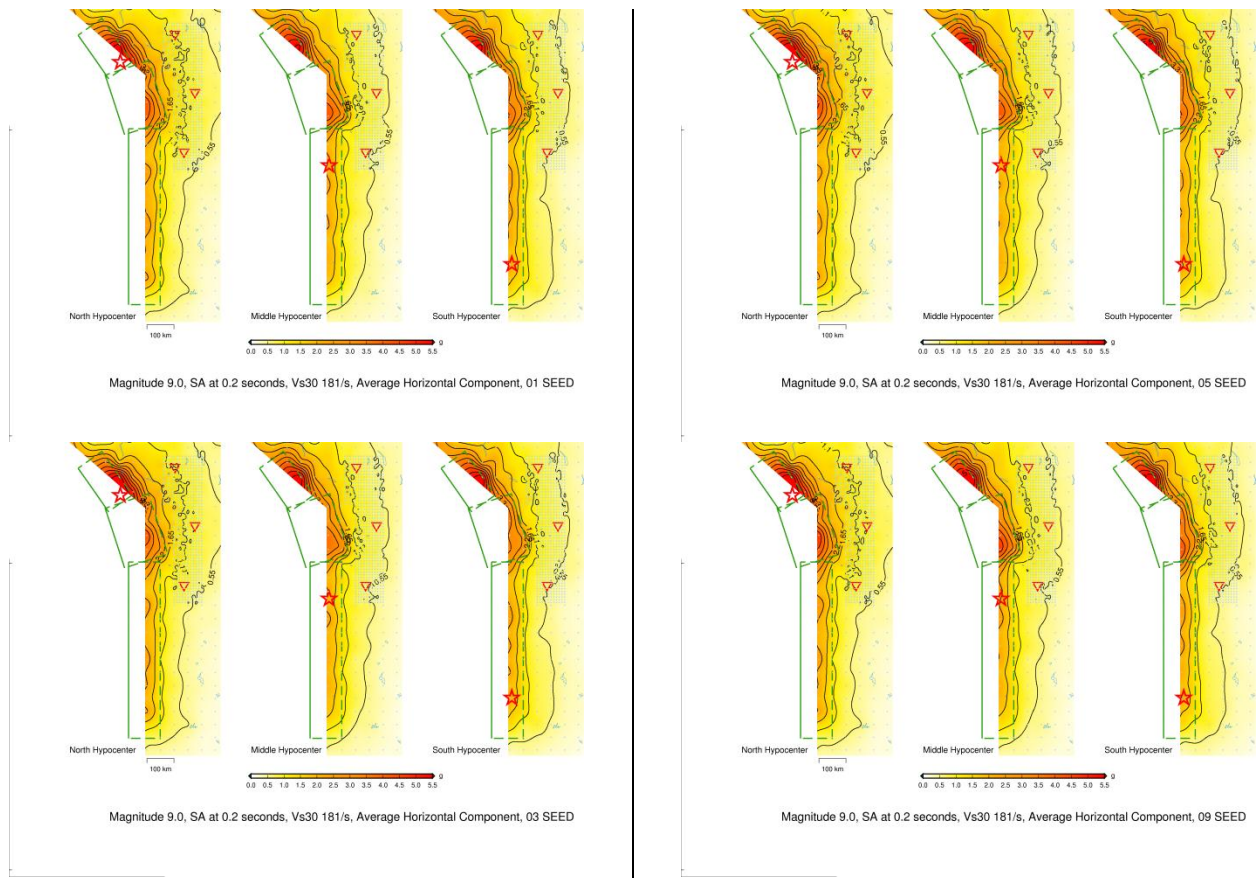
Figure 44. Ground motion maps for 1s spectral acceleration for an M 9.0 Cascadia earthquake for three hypocenter locations and various slip models, for Vs$_{30}$ 181 m/s.

Figure 45. Ground motion maps for 2s spectral acceleration for an M 9.0 Cascadia earthquake for three hypocenter locations and various slip models, for Vs$_{30}$ 434 m/s.
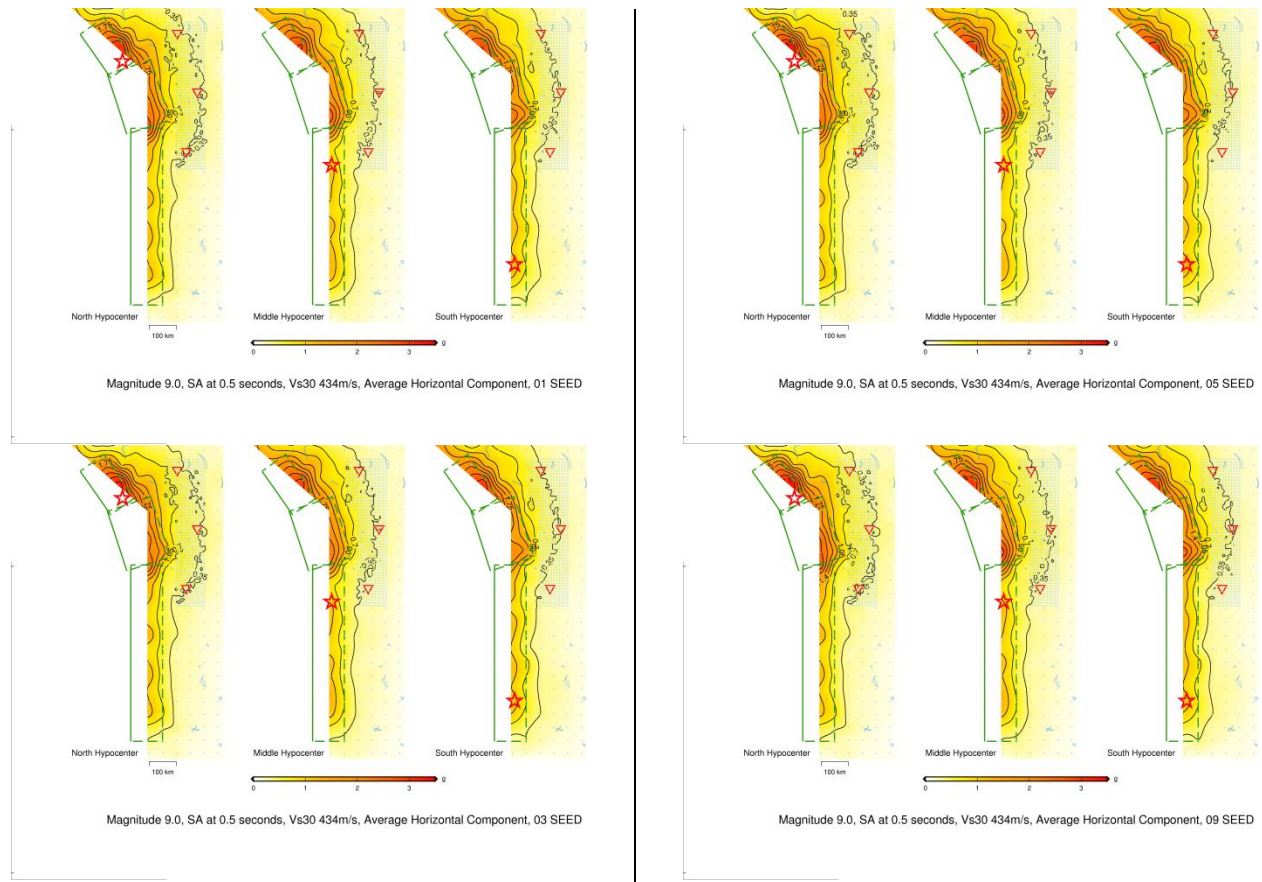
Figure 46. Ground motion maps for 2s spectral acceleration for an M 9.0 Cascadia earthquake for three hypocenter locations and various slip models, for Vs$_{30}$ 181 m/s.

Magnitude 9.0, SA at 5.0 seconds, Vs30 434m/s, Average Horizontal Component, 01 SEED

Magnitude 9.0, SA at 5.0 seconds, Vs30 434m/s, Average Horizontal Component, 05 SEED

Magnitude 9.0, SA at 5.0 seconds, Vs30 434m/s, Average Horizontal Component, 03 SEED

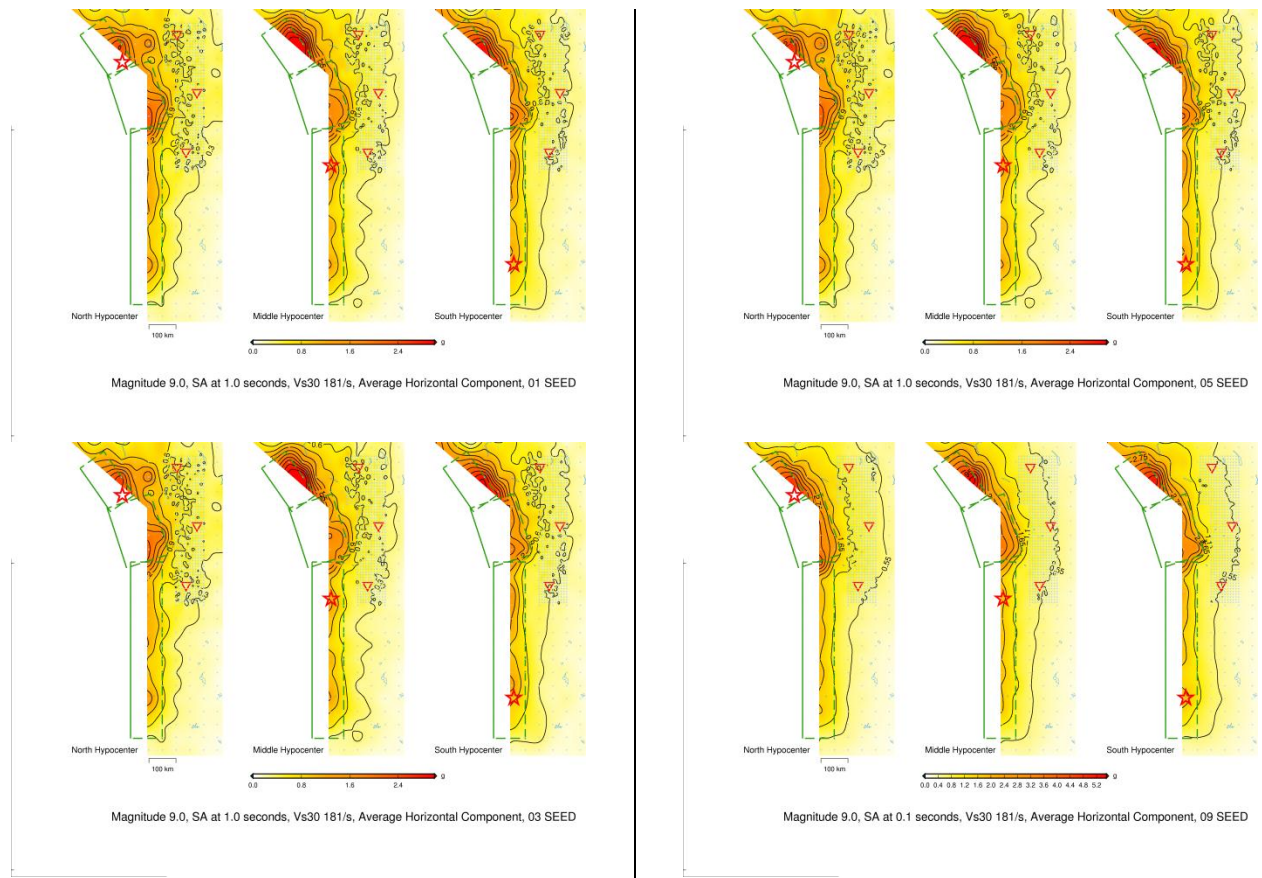Magnitude 9.0, SA at 5.0 seconds, Vs30 434m/s, Average Horizontal Component, 09 SEED

Figure 47. Ground motion maps for 5s spectral acceleration for an M 9.0 Cascadia earthquake for three hypocenter locations and various slip models, for Vs$_{30}$ 434 m/s.

Magnitude 9.0, SA at 5.0 seconds, Vs30 181/s, Average Horizontal Component, 01 SEED

Magnitude 9.0, SA at 5.0 seconds, Vs30 181/s, Average Horizontal Component, 05 SEED

Magnitude 9.0, SA at 5.0 seconds, Vs30 181/s, Average Horizontal Component, 03 SEED

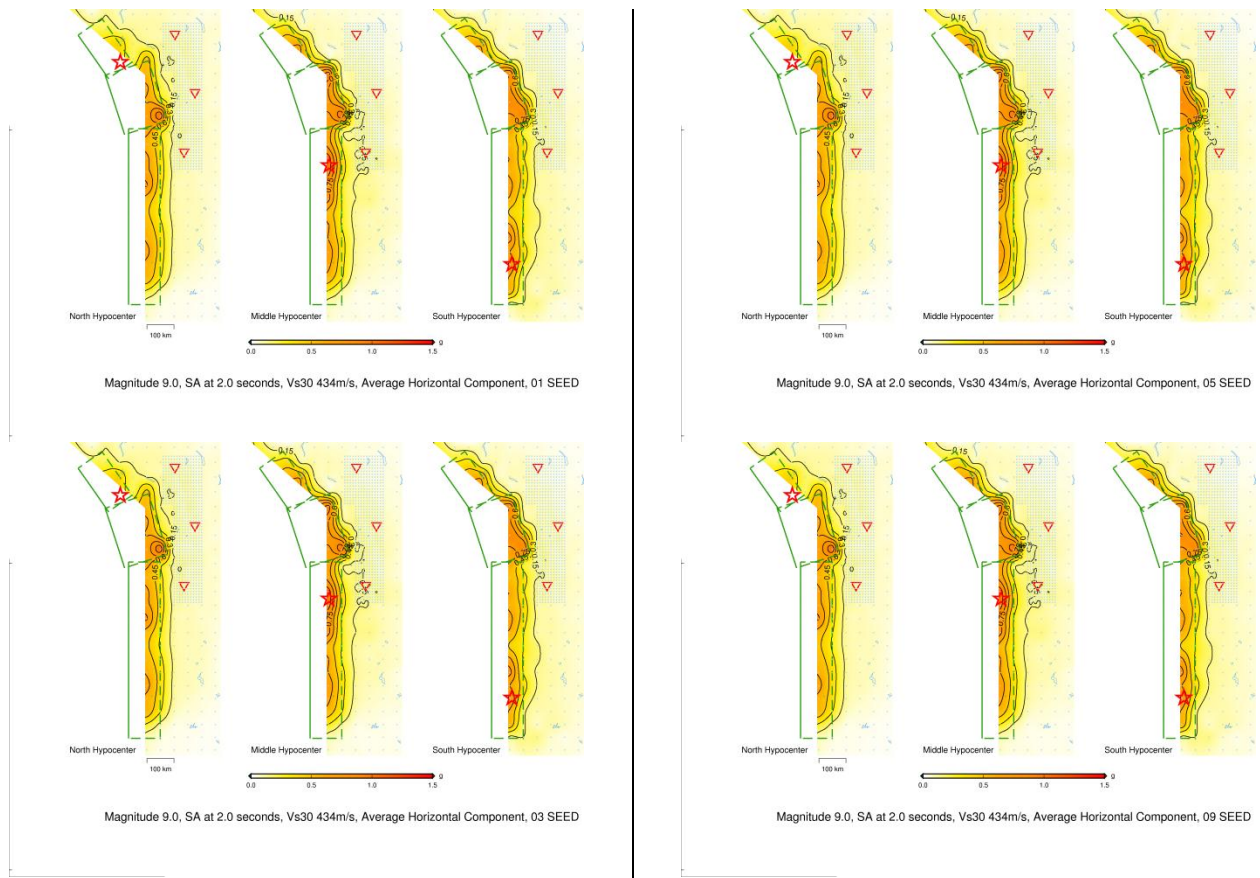Magnitude 9.0, SA at 5.0 seconds, Vs30 181/s, Average Horizontal Component, 09 SEED
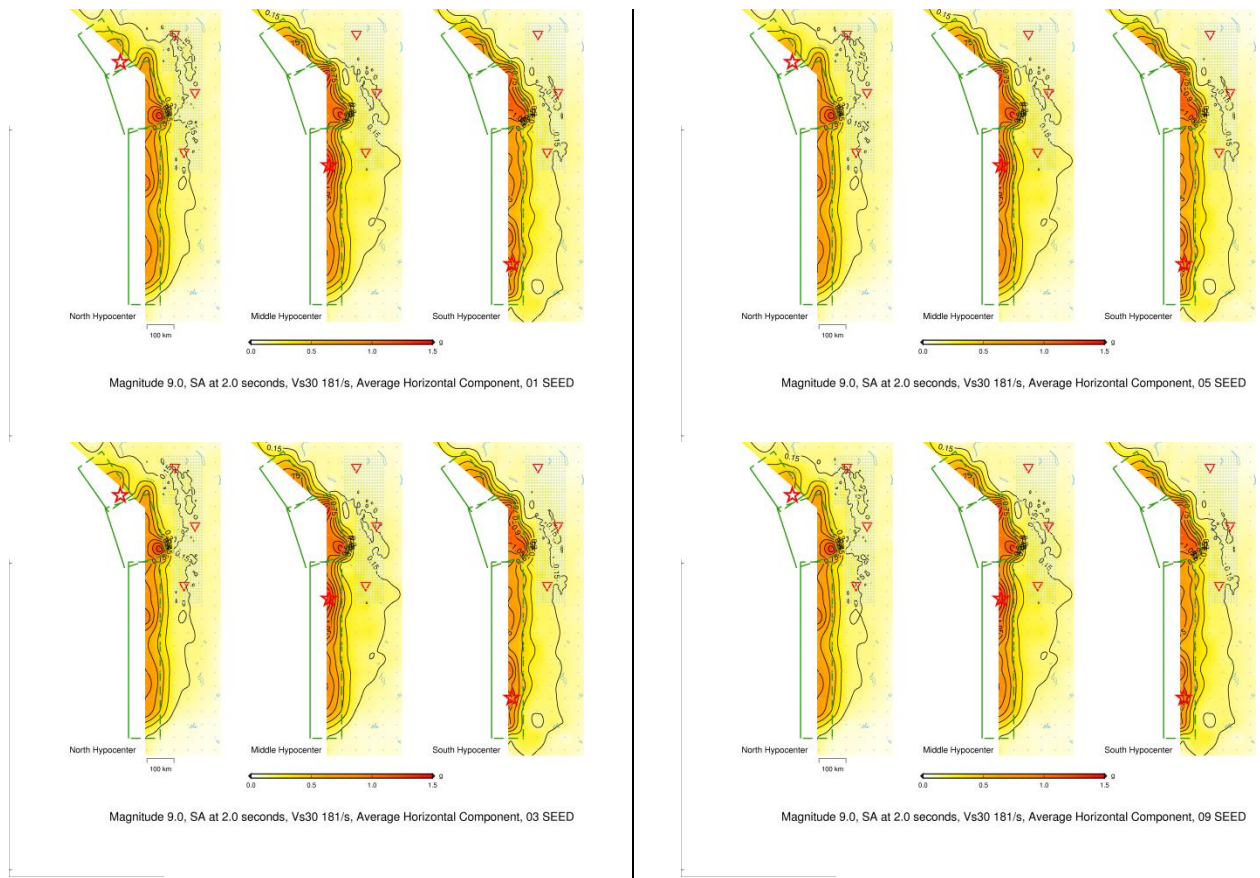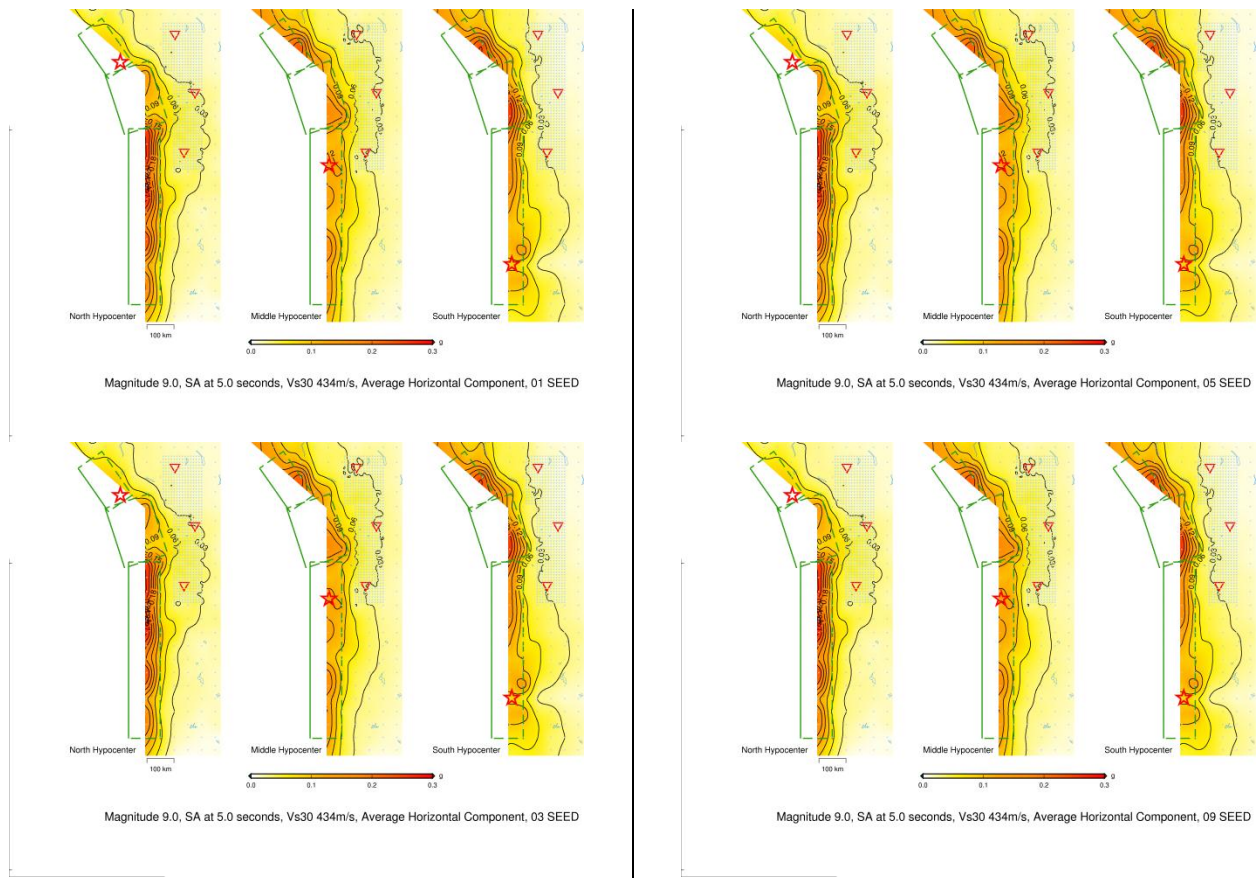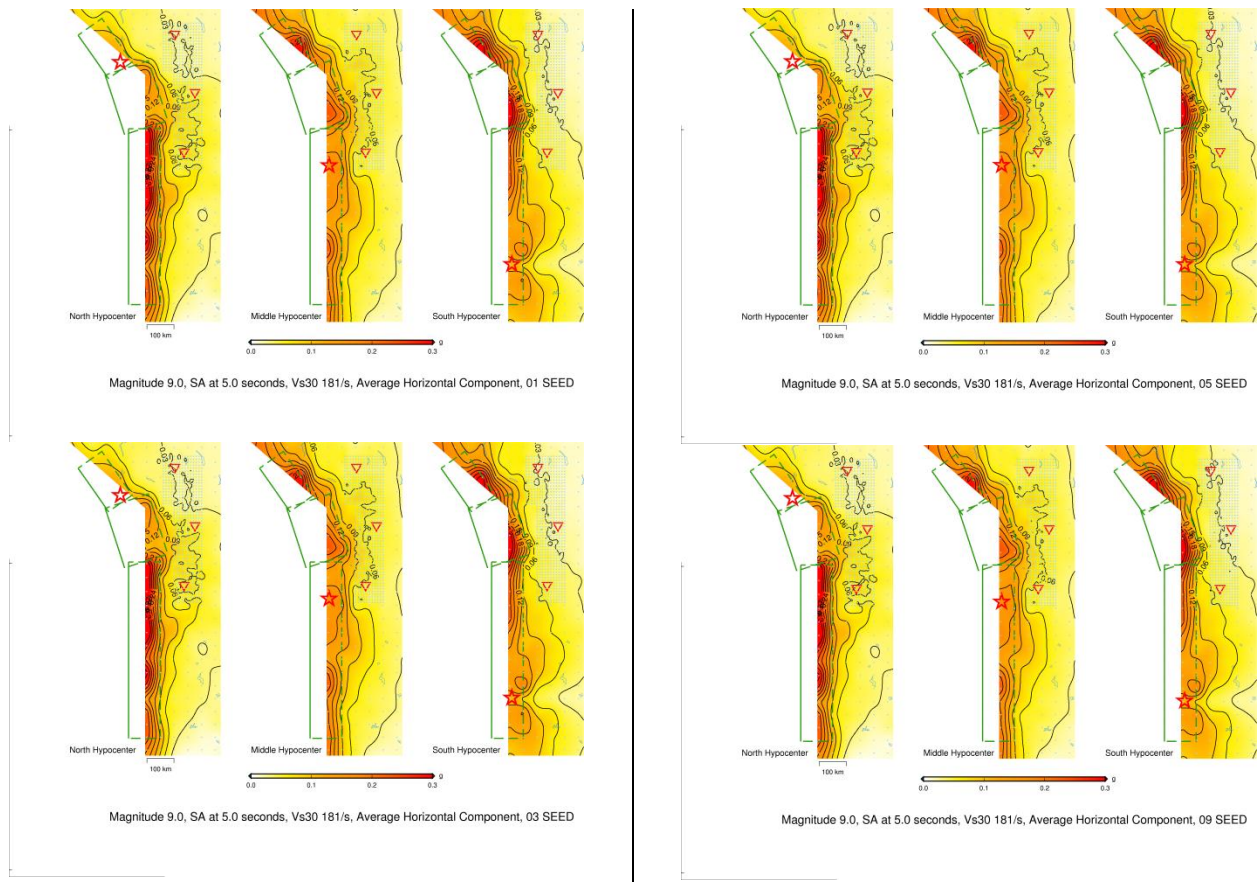
Figure 48. Ground motion maps for 5s spectral acceleration for an M 9.0 Cascadia earthquake for three hypocenter locations and various slip models, for Vs$_{30}$ 181 m/s.

TSUNAMI MODELING OF THE MAULE EARTHQUAKE AND CASCADIA SCENARIOS

INTRODUCTION

In this Section, we report analyses for tsunami that are analogous to those described above for strong ground motions. We first describe the tsunami modeling method that we use. Next we test the method by showing that it reliably matches the recorded tsunami amplitudes of the Mw 8.8 Maule, Chile earthquake. We then apply the tsunami simulation method to model tsunami runup throughout the Cascadia region from scenario Mw 9.0 subduction earthquakes, and provide detailed tsunami runup maps for four specific coastal locations: Seaside, OR and Crescent City, Klamath River and Redwood Creek, CA.

METHOD

We simulate tsunami propagation and inundation using the GeoClaw tsunami model. GeoClaw is a branch of the open source software package, CLAWPACK (Conservation LAWs PACKage) which was first released by LeVeque in 1994 (http://www.clawpack.org). GeoClaw was originally named TsunamiClaw; the code has been further developed and improved for tsunami modeling over the years. GeoClaw was approved in 2012 by the US National Tsunami Hazard Mitigation Program (NHTMP) for use in modeling work.

The GeoClaw model solves the two-dimensional depth-averaged nonlinear shallow water equations using high-resolution finite volume methods:

$$h_t + (hu)_x + (hv)_y = 0$$
$$(hu)_t + \left(hu^2 + \frac{1}{2}gh^2\right)_x + (huv)_y = -ghB_x - Du$$
$$(hv)_t + (huv)_x + \left(hv^2 + \frac{1}{2}gh^2\right)_y = -ghB_y - Dv$$

(4)

where h is the water depth, u and v are the depth-averaged velocities in the horizontal directions, B is the bathymetry or topography, and D (h, u, v) is the drag coefficient. Values of h, hu and hv in each grid cell represent cell averages of the depth and momentum components. The methods are exactly conservative for both mass and momentum with flat bathymetry; and conserve mass for arbitrary bathymetry when used on a fixed grid. This system of equations is widely used in modeling of tsunami propagation and inundation.

The high-resolution Godunov-type methods implemented in GeoClaw solve Riemann problems at each grid interface. Block structured adaptive mesh refinement (AMR) is used to employ much finer grid resolution in regions of particular interest.

The empirical Manning formulation is used to model bottom friction; generally for generic tsunami modeling, the constant value of the Manning coefficient n = 0.025 is used. GeoClaw can also account for Coriolis.

TSUNAMI OF THE Mw 8.8 2010 MAULE, CHILE EARTHQUAKE

The Mw 8.8 mega-thrust earthquake and tsunami occurred on 27 February 2010 offshore the Maule region, Chile. The time series of surface elevation at 16 stations shown in Figure 49 and listed in Table 7 are predicted by GeoClaw using an instantaneous tsunami source.

Table 7. Tide gauges and DART sensors that recorded the sea surface elevation.

Station Name	Latitude (°)	Longitude (°)
Ancud	286.158334	-41.858333
Antofagasta	289.583333	-23.650000
Arica	289.658334	-18.466667
Caldera	289.166667	-27.041667
Callao	282.833333	-12.058333
Coquimbo	288.675000	-29.950000
Corral	286.583333	-39.858333
Iquique	289.850000	-20.191667
San Felix	279.883333	-26.283333
Talcahuano	286.916667	-36.691667
Valparaiso	288.383333	-33.025000
Easter Is.	250.550000	-27.150000
Rikitea	225.050000	-23.133333
Owenga	183.633333	-44.008333
Waitangi	183.450000	-43.941667
DART 32412	273.608000	-17.975000
DART 51406	234.994440	-8.488861
DART 51426	191.901944	-22.993333
DART 54401	187.015000	33.005278

The seafloor displacement is calculated using the Okada method based on the slip distribution provided by Lorito et al. (2011). The Okada model is often used to translate slip along one small fault plane into the seafloor motion; the final displacement is achieved by combing the seafloor motions caused by the 200 small sub-faults.
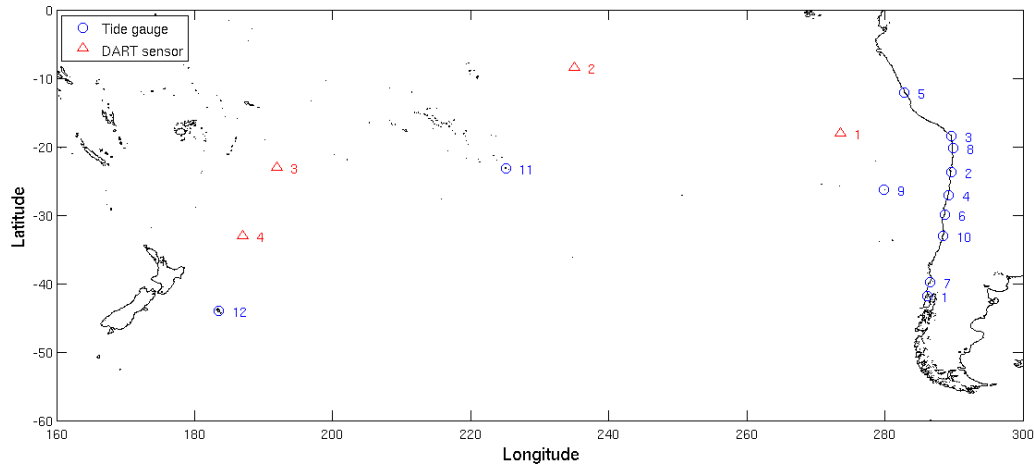
Figure 49. The locations of 12 tide gauges (blue circle) and 4 DART sensors (red triangle) used in the tsunami simulation of the 2010 Chile earthquake. The list of the coordinates of the 15 tide-gauges and 4 DART sensors is presented in Lorito (2011). The observed tide-gauge data at Stations Talcahuano, Easter Is. and Owenga obtained from the website are either not available or of poor quality and were not used in this analysis.

In this GeoClaw tsunami model, the computational domain used is (160º, 300º) in longitude and (-60º, 20º) in latitude. We use 6 levels of refinement going from a coarse grid with 2º resolution on Level 1, to the finest grid with resolution of 4" on Level 6 (2º, 30', 6', 2', 24", and 4"). The global bathymetric/topographic Digital Elevation Models (DEMs) used over the ocean are ETOPO1 with a resolution of 1' (approximately 2 km). Its horizontal datum is WGS84 and vertical datum is sea level. The dataset is available online at the NOAA/NGDC website. For the area around the 12 tide gauges, local bathymetries with a resolution of 4", obtained from Global Multi-Resolution Topography (the horizontal datum is WGS84 and the vertical datum is MHW) are used. Onshore topography is bare earth without structures.

The Manning coefficient n = 0.025 is used in this model, and the Coriolis terms are considered as well. The zero-order extrapolation from grid cells along the boundaries to ghost cells in every time step is used to implement non-reflecting boundary conditions at 4 edges of the computational domain. The total computational time is 20 hours.

The time series of sea surface elevation at the 16 stations (12 tide gauges and 4 DART sensors) are calculated with GeoClaw, and compared with the observed data (tidal effects are subtracted). Tide-gauge data are obtained from http://www.ioc-sealevelmonitoring.org; DART sensor data are from http://www.ndbc.noaa.gov/. The comparisons at 16 stations are shown on Figure 50. We can see that the numerical predictions (red) are in good agreement with the observations (blue) in both wave amplitude and phase, especially for the first few cycles after tsunami's arrival.
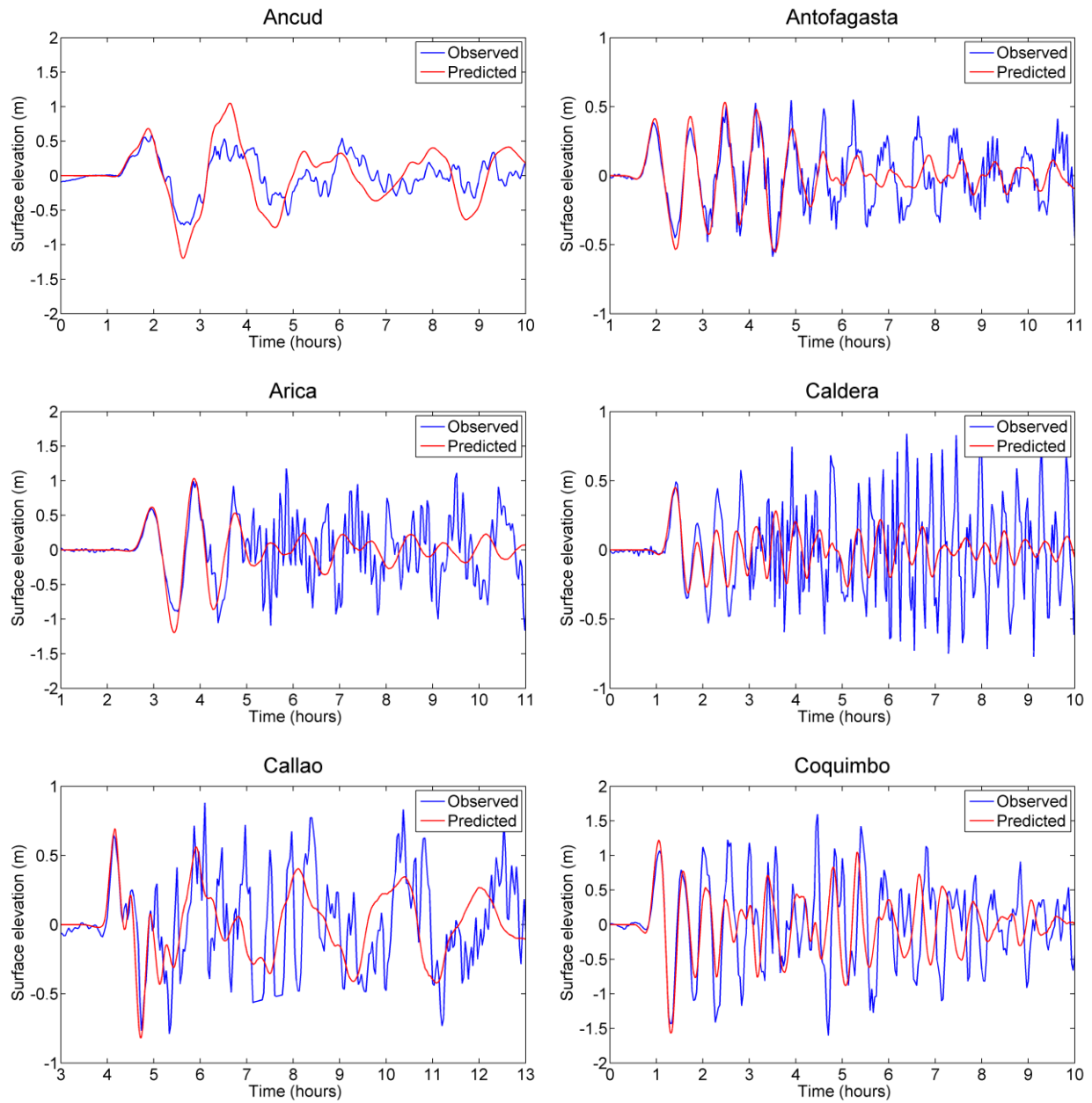
Figure 50. The time histories of water surface elevation predicted by GeoClaw (red) and the observed data (blue) at 12 tide-gauge stations and 4 DART-sensor stations.
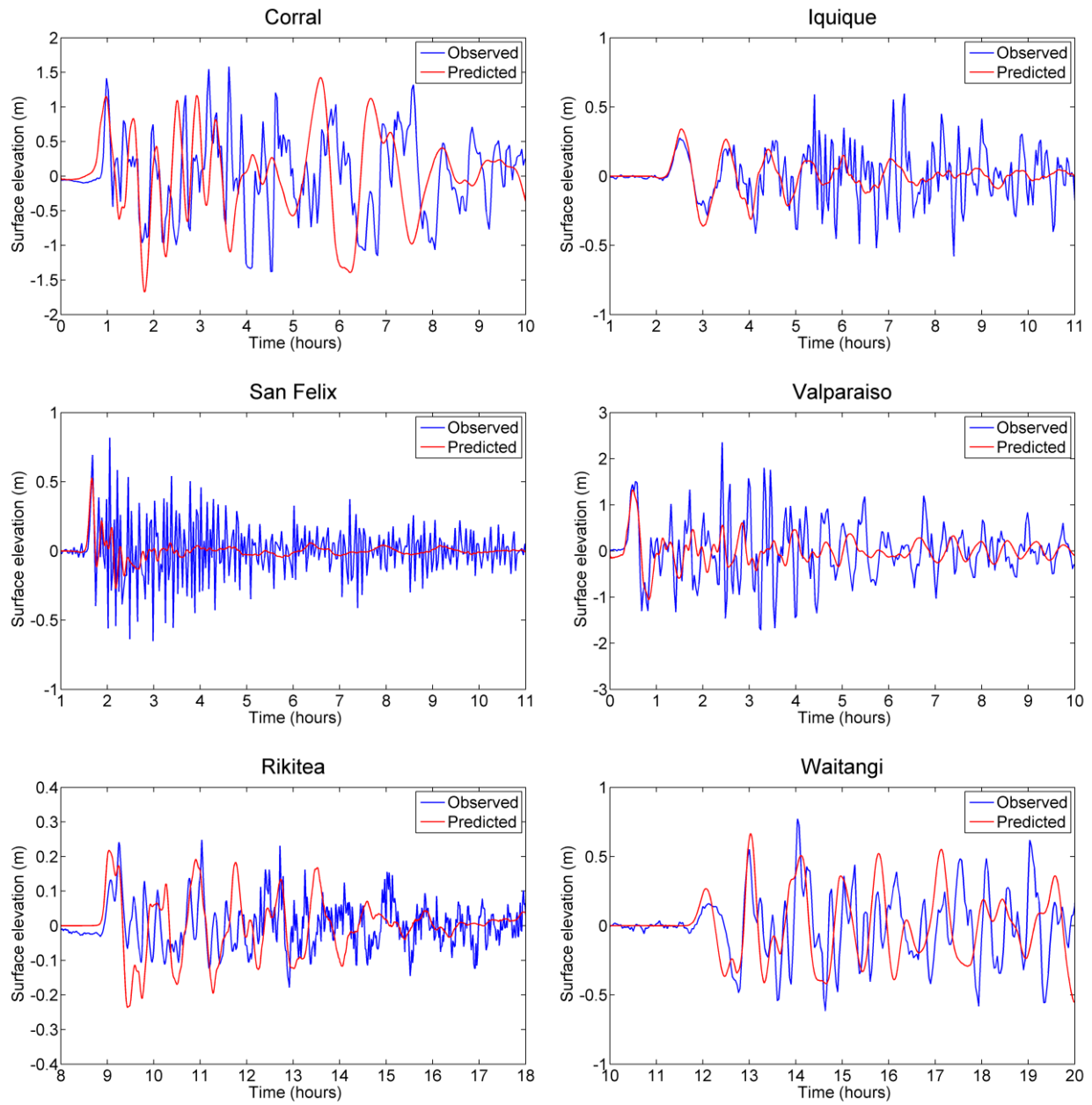
Figure 50. Cont.
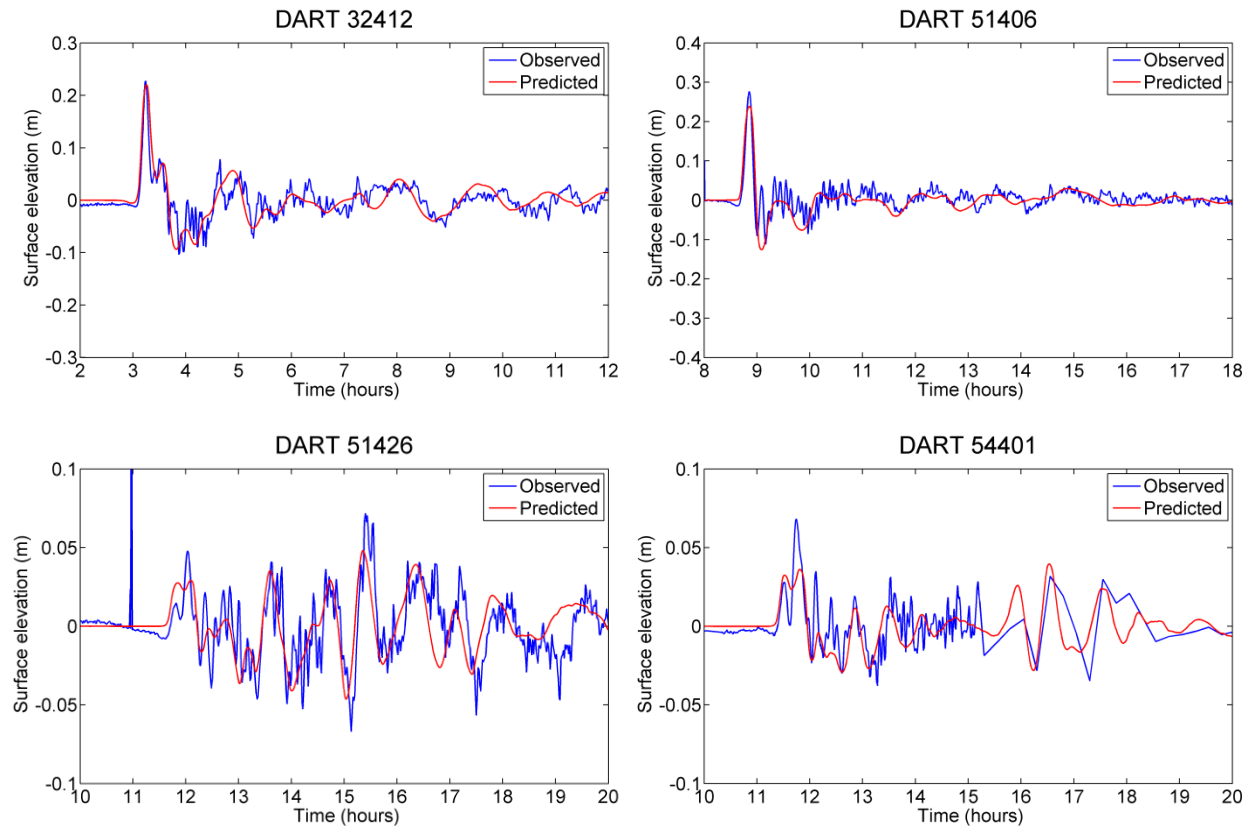
Figure 50. Cont.

TSUNAMIS OF MW 9.0 CASCADIA SUBDUCTION EARTHQUAKE SCENARIOS

The slip models used here are the slip models used in the simulation of ground motion described above: slip01, slip03, slip05 and slip09. The seafloor displacement is calculated using the Okada model. Since instantaneous tsunami sources are used, only the final seafloor displacement matters. Thus, different earthquake hypocentral locations with the same slip model have no effect on the tsunami simulations.

The computational domain used in this model is (-150º, -115º) in longitude and (30º, 55º) in latitude, and non-reflecting boundary conditions are applied at the four edges of the computational domain. The total computational time is 4 hours. The Manning coefficient n = 0.025 is used and the Coriolis terms are turned on in this model. There are four target areas that we are interested in: Crescent City, CA; Klamath River, CA; Redwood Creek, CA; Seaside, OR. The bathymetric or topographic data used are ETOPO1 global grids and local 1/3" DEMs from NOAA/NGDC website (horizontal datum WGS84 and vertical datum MHW). The grid refinement has 5 levels from coarse to fine grids (20', 4', 1', 10", and 1"). Around the target areas, the grid resolution is set between levels 4 and 5 (10" to 1") and is automatically refined by GeoClaw. The tsunami inundation maps around the four target areas using Mw 9.0 Cascadia slip models of slip_01, slip_03, slip_05 and slip_09 are shown in Figures 3-6. The grey lines in each chart denote the topographic contours every 100 m. Here the tsunami inundation map presents the maximum value ζ over the full time period of a tsunami of either the flow depth at points on land or the sea surface elevation relative to MHW for points offshore. The tidal level is set to be MHW.

The results presented in Figures 3-6 demonstrate that the tsunami inundation maps around the four target areas predicted by GeoClaw from the four slip models have similar characteristics. The maximum values of tsunami inundation (ζ_{max}) around each target area from each slip model are marked in each plot. Generally, the area around Seaside, OR has relatively larger inundation since it is closer to the center of the Cascadia tsunami source; and the area around Redwood Creek, CA has relatively lower wave height offshore or flow depth onshore because it is near the southern end of the tsunami source.
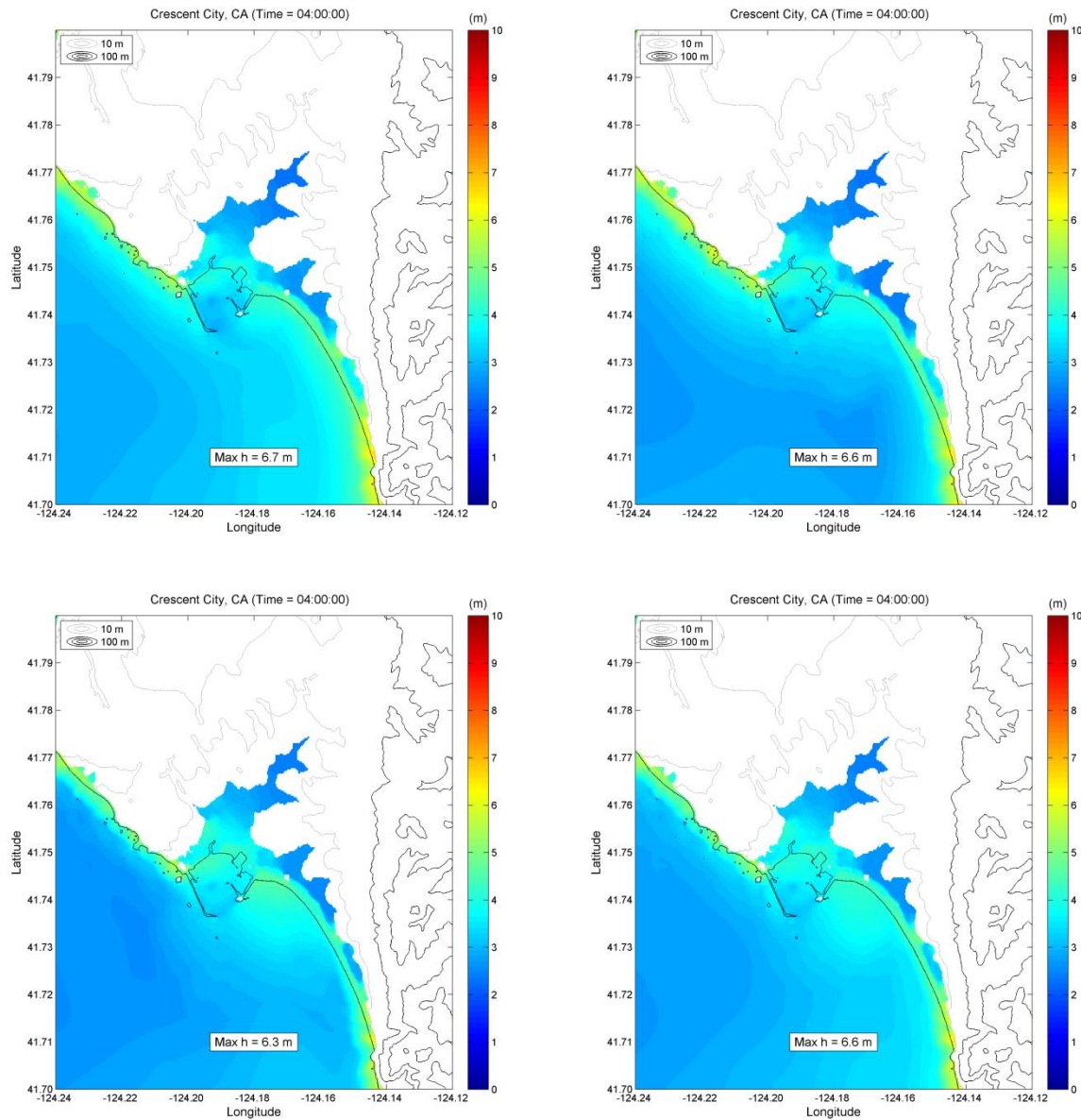
Figure 51. Tsunami inundation maps around Crescent City, CA predicted by GeoClaw from M 9.0 Cascadia slip models slip01 (upper left), slip03 (upper right), slip05 (lower left) and slip09 (lower right). The maximum inundation is recorded on a 1" grid.
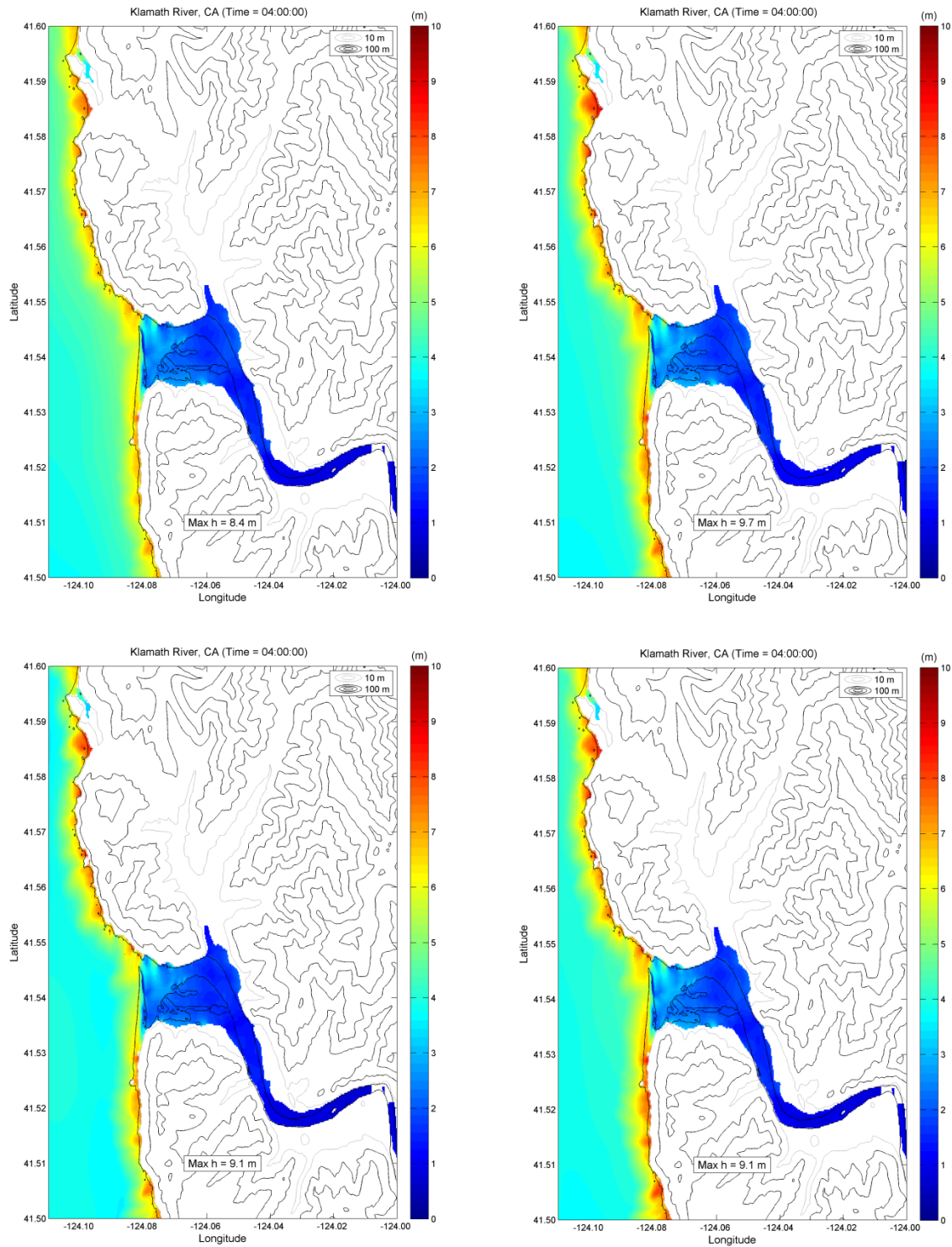
Figure 52. Tsunami inundation maps around Klamath River, CA predicted by GeoClaw from M 9.0 Cascadia slip models slip01 (upper left), slip_03 (upper right), slip05 (lower left) and slip09 (lower right).

Figure 53. Tsunami inundation maps around Redwood Creek, CA predicted by GeoClaw from M 9.0 Cascadia slip models slip01 (upper left), slip03 (upper right), slip05 (lower left) and slip09 (lower right).
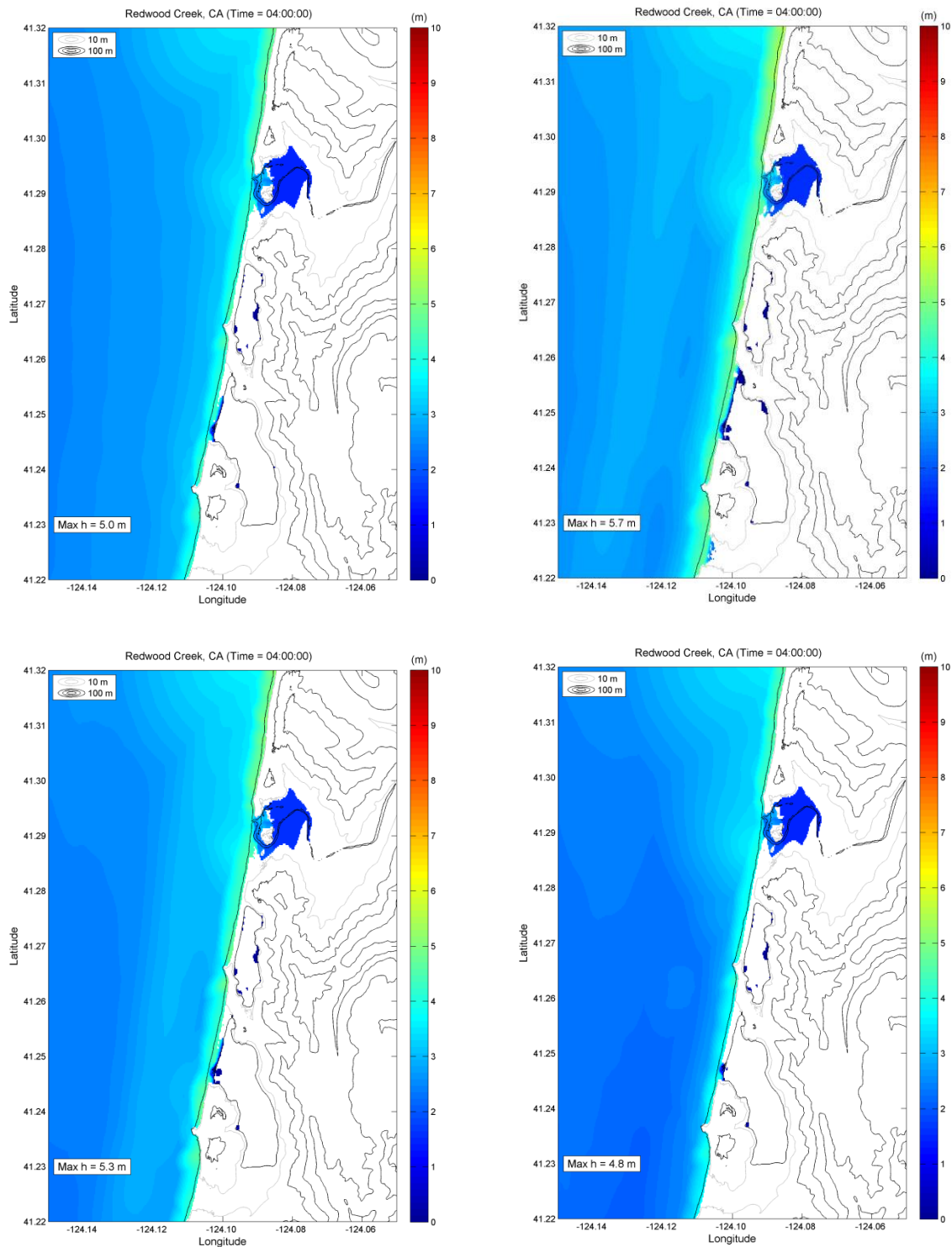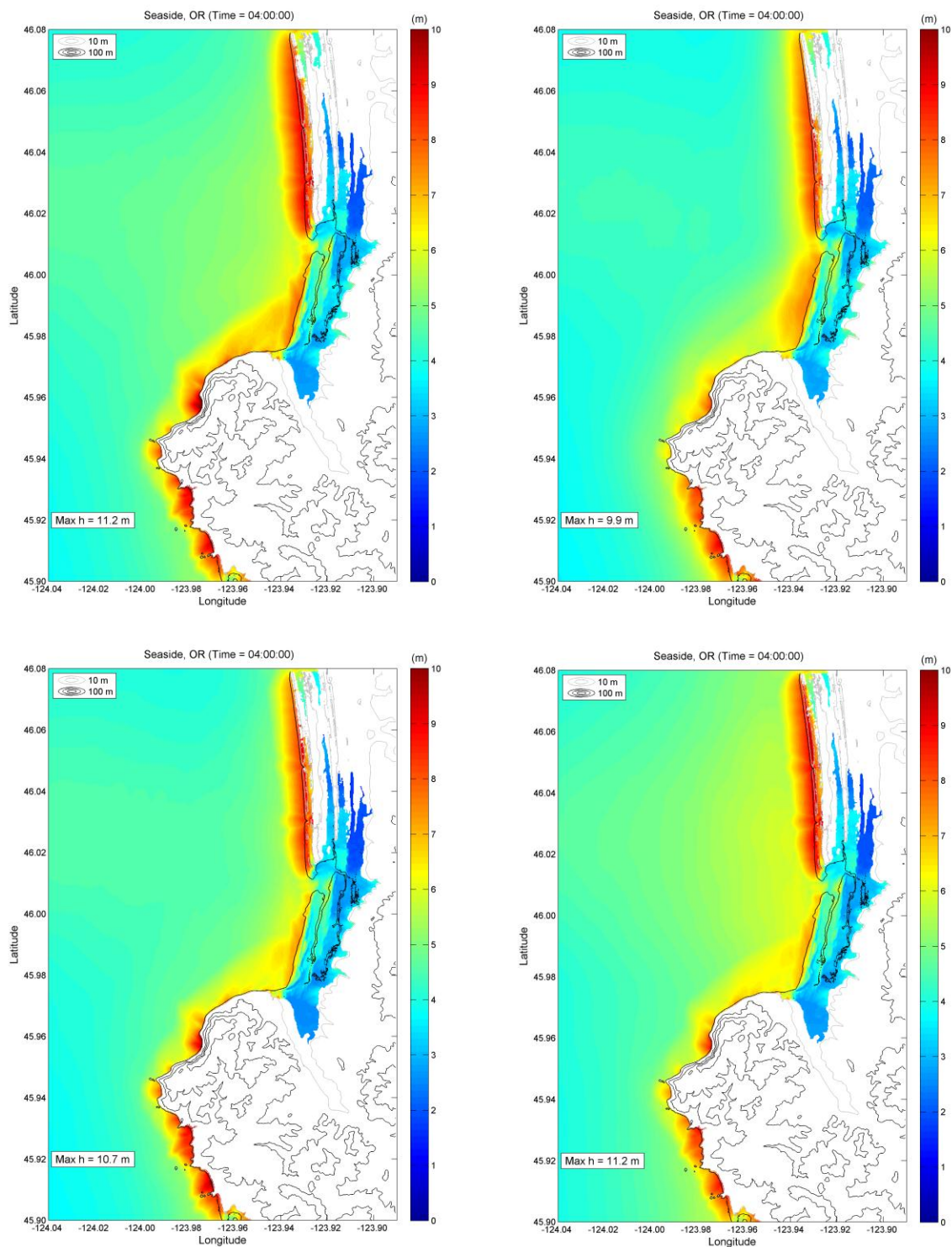
Figure 54. Tsunami inundation maps around Seaside, OR predicted by GeoClaw from M 9.0 Cascadia slip models slip01 (upper left), slip03 (upper right), slip05 (lower left) and slip09 (lower right).

REFERENCES

Abrahamson, N.A., P.G. Somerville, and C. Allin Cornell (1990). Uncertainty in numerical strong motion predictions, *Proc. 4th U.S. National Conference on Earthquake Engineering,* **1**, 407- 416.

Abrahamson, N., N. Gregor and K. Addo (2012). BC Hydro Ground Motion Prediction Equations for Subduction Earthquakes. *Earthquake Spectra, submitted*.

Atkinson, G.M. and D.M. Boore (2003). Empirical ground motion relations for subduction zone earthquakes and their application to Cascadia and other regions, *Bull. Seism. Soc. Am*., in press.

Boroscheck, R., and D. Comte (2004). Time – frequency characteristics of the 2001 Southern Peru, Mw 8.4 earthquake. 13th World Conference on Earthquake Engineering, Vancouver, B.C., Canada, August 1 – 6, Paper No. 287.

Boroscheck, R., V. Contreras, D.Y. Kwak and J.P. Stewart (2012). Strong Ground Motion Attributes of the 2010 Mw 8.8 Maule, Chile, Earthquake. Earthquake Spectra, 28, 19-38.

Boroscheck, R., and V. Contreras (2012). Strong ground motion from the 2010 Mw8.8 Maule Chile earthquake and attenuation relations for Chilean subduction zone interface earthquakes. International Symposium on Engineering Lessons Learned from the 2011 Great East Japan Earthquake, Tokyo, Japan, March 1-4.

Brocher, T.M., T. Parsons, A. Trehu, C.M. Snelson, and M.A. Fisher (2003). Seismic evidence for widespread serpentinized forearc upper mantle along the Cascadia margin. Geology 31, 267-270.

Clowes, R.M., M.T. Brandon, A.G. Green, C.J. Yorath, A.S. Brown, E.R. Kanasewich, and C. Spencer (1987). LITHOPROBE – southern Vancouver Island: Cenozoic subduction complex imaged by deep seismic reflections. Can. J. Earth Sci., 24, 31-51.

Cohee, B.P., P.G. Somerville and N.A. Abrahamson (1991). Ground motions from hypothesized Mw = 8 subduction earthquakes in the Pacific Northwest, *Bull. Seism. Soc. Am.,* **81**, 28-56.

González F. I., R. J. LeVeque, P. Chamberlain, B. Hirai, J. Varkovitzky and D. L. George (2011). Validation of the GeoClaw model, *NTHMP MMS Tsunami Inundation Model Validation Workshop*.

Graves, R.W. and A. Pitarka (2004). Broadband time history simulation using a hybrid approach. Proceedings of the 13th World Conference on Earthquake Engineering, Vancouver, Canada, August 1-6, 2004, Paper No. 1098.

Graves, R.W. (2005). Broadband simulation for a Mw 6.7 earthquake on the Puente Hills Fault. *SRL* 76, p. 242.

Guatteri, M., Mai, P.M., Beroza, G., and Boatwright, J. (2003). Strong ground motion prediction from stochastic-dynamic source models." Bull. Seism. Soc. Am. 93: 301-313.

Hartzell S. (1978). Earthquake aftershocks as Green's functions. Geophys. Res. Lett. 5: 1-4.

Hartzell S., and T. Heaton (1983). Inversion of strong ground motion and teleseismic waveform data for the fault rupture history of the 1979 Imperial Valley, California earthquake. Bull. Seism. Soc. Am. 1983; 1553-1583.

Hisada, Y. (2001). A theoretical omega-squared model considering spatial variation in slip and rupture velocity. Part 2. Case for a two-dimensional source model. Bull. Seism. Soc. Am. 91, 651-666.

Irikura K. (1978). Semi-empirical estimation of strong ground motions during large earthquakes. Bull. Disast. Prev. Res. Inst., Kyoto Univ. 33: 63-104.

Ichinose, G. A., H. K. Thio, P. G. Somerville, T. Sato, and T. Ishii (2003). Rupture model for the 1944 Tonankai earthquake from the inversion of teleseismic and regional seismograms, J. Geophys. Res. 108, 10, 2497.

Ichinose, G., H.K. Thio and P. Somerville (2003b). Source characteristics of modern and historical in-slab Cascadia earthquakes applicable to strong motion prediction. USGS Final Report, Award 02HQGR0018.

Ishii, T. T. Sato and P.G. Somerville (2000). Identification of main rupture areas of heterogeneous fault models for strong motion estimates. J. Struct. Constr. Eng. AIJ, 527, 61-70.

Kagawa, T., K. Irikura and P.G. Somerville (2004). Differences in ground motion and fault rupture process between the surface and buried rupture earthquakes. *Earth Planets Space*, 56, 3-14.

Lorito S., F. Romano, S. Atzori, X. Tong, A. Avallone, J. McCloskey, M. Cocco, E. Boschi and A. Piatanesi (2011). Limited overlap between the seismic gap and coseismic slip of the great 2010 Chile earthquake. Nature Geoscience, 4, 173 – 177.

Mai, M.P. and G. Beroza. (2002). A spatial random field model to characterize complexity in earthquake slip. J. Geophys. Res. 107(B11): doi:10.1029/2001JB000588.

McNeill, A.F., M.G. Bostock, G.C. Rogers, and J.C Shragge (2004). The effect of forearc mantle serpentinization on ground motions from megathrust and intraslab events in the Cascadia subduction zone. BSSA. 94, 147-154.

Ocola, L.C., J. Luetgert, L.T. Aldrich, R.P. Meyer, and C.E. Helsey (1995). Velocity structure of the coastal region of southern Peru from seismic refraction / wide-angle reflection data. J. Geodynamics 20, 1-30.

Ohtsuka, H., P.G. Somerville, and T. Sato (1998). Estimation of broadband strong ground motions considering uncertainty of fault parameters, J. Struct. Mech. Earthq. Eng., JSCE, No.584/I-42, 185-200.

Petersen, M., A. Frankel, A., S. Harmsen, C. Mueller, K. Haller, R. Wheeler, R. Wesson, Y. Zeng, O. Boyd, D. Perkins, N. Luco, E. Field, C. Wills, and K. Rukstales (2008). Documentation for the 2008 updated of the United States National Seismic Hazard Maps. *U.S. Geological Survey Open File Report* 2008-1128.

Petersen, M.D., C.H. Cramer, and A.D. Frankel (2002). Simulations of seismic hazard for the Pacific Northwest of the United States from earthquakes associated with the Cascadia subduction zone. Pure Appl. Geophys. 159, 2147-2168.

Pitarka, A., R. Graves, P.G. Somerville (2002). Investigation of effects of the Seattle Fault Zone structural complexities on ground motions in the Seattle Basin, EOS 83.

Somerville, P.G., H.K. Thio, G, Ichinose, N. Collins, A. Pitarka, and R. Graves (2003). Earthquake source and ground motion characteristics of the June 23, 2001 Mw 8.4 Arequipa, Peru, earthquake. *SRL* 74, 223.

Somerville, P.G., T. Sato, T. Ishii, N.F. Collins, K. Dan and H. Fujiwara (2002). Characterizing heterogeneous slip models for large subduction earthquakes for strong ground motion prediction. Proceedings of the Architectural Institute of Japan.

Somerville, P.G., K. Irikura, R. Graves, S. Sawada, D. Wald, N. Abrahamson, Y. Iwasaki, T. Kagawa, N. Smith and A. Kowada (1999). Characterizing earthquake slip models for the prediction of strong ground motion. Seismological Research Letters 70, 59-80.

Somerville, P.G., M.K. Sen and B.P. Cohee (1991). Simulation of strong ground motions recorded during the 1985 Michoacan, Mexico and Valparaiso, Chile earthquakes, BSSA., 81, 1-27. Somerville P., R. Graves and N. Collins (2008). Ground motions from large Cascadia subduction earthquakes. Report, U.S. Geological Survey, Award Number: 06HQGR0160.

Wald, D.J. and P.G. Somerville (1995). Variable slip rupture model of the great 1923 Kanto, Japan earthquake: geodetic and body-waveform analysis. Bull. Seism. Soc. Am., 85, 159-177.

Zhao, J.X., J. Zhang, A. Asano, Y. Ohno, T. Oouchi, T. Takahashi, H. Ogawa, K. Irikura, H.K. Thio, P. Somerville, Y. Fukushima, and Y. Fukushima (2006). Attenuation Relations of Strong Motion in Japan using Site Classification based on Predominant Period. Bull. Seism. Soc. Am. 96, 898-913.